

# Design of CVD Coatings for Cutting Tools



Dipl.-Ing. Christoph Czettl

being a thesis in partial fulfilment of the requirements for the degree of a

**Doctor of Montanistic Sciences (Dr. mont.)**

at the Montanuniversität Leoben

Leoben, November 2013

Financial support by the Austrian Federal Government (in particular from the Bundesministerium für Verkehr, Innovation und Technologie and the Bundesministerium für Wirtschaft, Familie und Jugend) and the Styrian Provincial Government, represented by Österreichische Forschungsförderungsgesellschaft mbH and by Steirische Wirtschaftsförderungsgesellschaft mbH, within the research activities of the K2 Competence Centre on “Integrated Research in Materials, Processing and Product Engineering”, operated by the Materials Center Leoben Forschung GmbH in the framework of the Austrian COMET Competence Centre Programme, is gratefully acknowledged.

## **Affidavit**

I declare in lieu of oath, that I wrote this thesis and performed the associated research myself, using only literature cited in this volume.

Reutte, 28<sup>th</sup> November 2013

## **Acknowledgement**

My sincerest gratitude is due to Prof. Dr. Christian Mitterer for the possibility to compose this thesis at the Chair for Functional Materials and Material Systems. For the countless discussions which extended my view during the last years, as well as the perfect example how teamwork should be. Christian, I am impressed in which way you brought me and my thesis forward – thank you very much!

I am grateful to ao. Prof. Dr. Reinhold Ebner and to Dr. Richard Schanner, managing directors of the Materials Center Leoben (MCL), for giving me the opportunity to carry out my thesis within an MCL project. I am also thankful to the MCL staff and the co-workers for their support.

Many thanks to DI Dr. Martin Kathrein for the perfect design of this project and for guiding through the basics of coated carbide tools and chemical vapor deposition.

I want to express my gratitude to MSc Marianne Penoy and DI Claude Michotte from CERATIZIT Luxembourg. For the countless measurements performed within this thesis and beside. Thanks for the valuable discussions and support.

Special thanks to the people who decided to support me and the whole project. Your help was essential to perform this thesis. In particular I'd like to thank my Diploma Student DI Elisabeth Brettner, my student co-workers DI Tamara Tepperneegg, Cornelia Hoffmann and Mario Mangelberger, as well as the whole Thin Film Group for all the discussions and support. It was a great time!

I want also thank the whole R&D Group of Ceratizit Reutte for their help, discussions and the support without doubt of all ideas I had. I'm proud to be a part of this Team. Special thanks to Christian Dürhammer and Peter Lechleitner for their assistance during the installation of the CVD Device, which was essential for this thesis.

For the insights in the History of CVD and the numerous discussions, I want like to thank Werner Bürgin and Helga Holzschuh from SuCoTec AG.

Last but not least I want to thank my Family, who made all this possible and supported me in every situation.

If everything seems under control, you're not going fast enough

(Mario Andretti)

# Content

1	Introduction .....	1
2	Chemical vapour deposition .....	2
3	Coating systems for cutting inserts.....	6
3.1	Historic development of TiN/TiCN/Al <sub>2</sub> O <sub>3</sub> coating systems.....	6
3.2	κ- to α-Al <sub>2</sub> O <sub>3</sub> phase transformation .....	7
3.3	Improved α-Al <sub>2</sub> O <sub>3</sub> coatings and interlayers.....	9
3.4	The evolution of base layer systems .....	11
3.5	Crystal orientation of α-Al <sub>2</sub> O <sub>3</sub> .....	14
3.6	Post treatment of coatings and residual stresses .....	15
3.7	Future developments - TiAlN coatings via CVD.....	20
4	Conclusions and outlook .....	22
5	Literature.....	24
6	Publications.....	29
6.1	List of included Publications .....	29
6.2	Publications related to this work .....	30
6.3	My contribution to the included Publications.....	32
	Publication I.....	34
	Publication II.....	45
	Publication III.....	60
	Publication IV .....	75

# 1 Introduction

The trend of higher productivity and cost efficiency in the metal cutting industry lead to increased demands of tools, regarding higher feed rates and cutting velocity in combination with higher reliability. Therefore, the wear resistance, thermal stability as well as toughness of the tools have to be improved [1]. For machining of low carbon steels, stainless steels and cast irons, coated cemented carbide indexable inserts are frequently used beside cermets and ceramic materials [2, 3]. For those applications, where high thermal resistivity and wear resistance have to be covered with coatings up to 30  $\mu\text{m}$  total thickness, chemical vapour deposition (CVD) is still state of the art [4-6]. The single layer TiC, TiN and TiCN coatings developed in the last century have been extended to multilayer coatings, where the different benefits of the materials like hot hardness and oxidation resistance are combined [7]. During the last two decades, the main efforts were to control and optimize the structure of the components, especially the  $\text{Al}_2\text{O}_3$  phase and orientation [8-14]. The adjustment of material properties, starting with the outermost zone of the substrate material [15], the applied coating layers and their interfaces [10, 16-21] in combination with the deposition parameters are necessary to obtain an optimized tool. This has also to be adjusted to the associated post treatment process, where the final properties of the coated indexable insert are achieved [22-25]. The aims of recent investigations are to improve the understanding of the tribological system, in particular the generation of heat due to friction and plastic deformation of the chip in combination with the tool. In this complex system, the macroscopic scale of coating system, i.e. layer thickness and layer architecture, have to be combined with the adjusted structures and material properties. Finally, the design of interfaces has to be conducted on an atomistic level, to achieve the desired adherence of the individual layers within the coating architecture and to the substrate. The residual stresses caused by the thermal mismatch of layer and substrate materials have to be taken into account in combination with the modification of stress level due to the post treatment [22, 23, 26]. For a coating architecture with optimized performance, all of the above mentioned considerations have to be considered.

## 2 Chemical vapour deposition

Chemical vapour deposition is a thermally activated process using volatile precursors, which react to solid products. Various types of CVD processes have been developed, to fulfil the criteria of a wide range of application from semiconductors, optical coatings, thermal barriers to wear resistant coatings. The deposition process can be assisted for example by plasma, laser or microwaves to lower the deposition temperatures close to room temperature. Numerous precursor materials from halide materials, carbonyls and metal organic compounds are used [27-29]. The solid products can form a surface covering layer due to heterogeneous reaction on the substrate or powder by a homogenous gas phase reaction. The second one is used to synthesize high purity fine grained powders, but is undesired for a coating process [27]. For the deposition of hard coatings for cutting applications, mainly the thermal process in a temperature range of 700 to 1100 °C is used. The principle build-up of a hot wall CVD unit, used for coating cemented carbide inserts [30], is shown in Fig. 1. The feed gas mixture is composed of pure gases dosed by rotameters [31] or mass flow controllers and halides, which can be volatilized by bubbler principle, liquid injection or chlorination above the boiling point. For precursors, which are liquid at room temperature (i.e.  $\text{TiCl}_4$ ,  $\text{SiCl}_4$ ,  $\text{CH}_3\text{CN}$ ), the bubbler principle was substituted by liquid mass flow controllers, which are much more precise. The chlorination of solid precursor materials above their boiling point is used in industrial scale for the generation of  $\text{AlCl}_3$ ,  $\text{HfCl}_4$  and  $\text{ZrCl}_4$  in external reactors using preheated feed gas lines to prevent condensation. Computer controlled deposition systems using mass flow controllers for precise dosing of precursors are state of the art in production scale and enable the possibility to use hundreds of different steps and allow gradients between them for a smooth transition of gas composition.

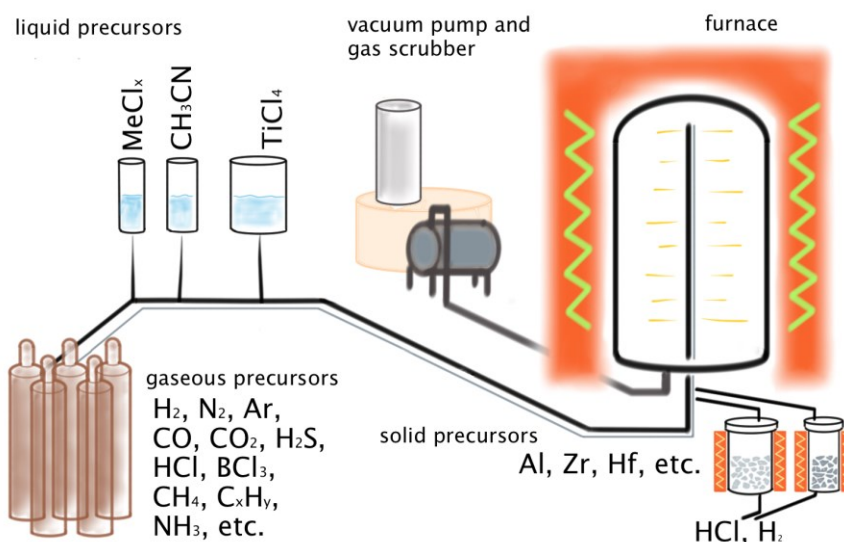


Fig. 1: Principle of an industrial scale low-pressure CVD system. The supply of gaseous precursors, liquid precursors and chlorinator for solid precursors, to the heated retort is shown. The off gas with by-products is neutralised in a gas scrubber [own work].

During the last century, different gas flow principles (c.f. Fig. 2) have been developed for coating cemented carbide inserts. The consequent reduction of path lengths, which a feed gas has to pass to attain all inserts of a batch, is necessary to obtain a homogenous coating structure and to avoid depletion of the feed gas. The evolution led from the bottom-to-top principle used for TiC, TiCN and TiN coatings, over alternative systems to the frequently used centric feed gas system [32]. This enables batch sizes of up to 15.000 half inch inserts and makes the coating process more cost efficient [33, 34].

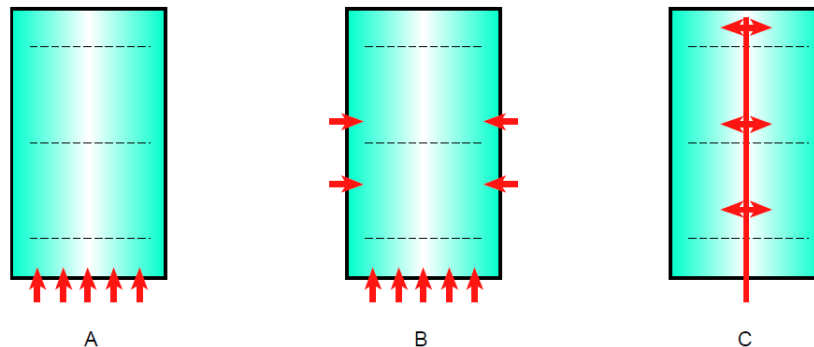


Fig. 2: Gas flow principles for coating cemented carbide inserts: (a) from bottom to top, (b) from bottom to top with additional gas inlets and (c) centric feed gas tube [33].

When the prepared gas mixture reaches the substrates, five crucial steps determine the deposition process (c.f. Fig. 3). The first step of the deposition process is the diffusion through the boundary layer (1), followed by the adsorption of the reactants on the substrate surface (2). The adsorbed species can diffuse on the surface depending on the substrate temperature and finally react to products and by-products (3). The desorption of the by-products (4) is followed by the diffusion through the boundary layer (5) and the evacuation of the by-products. When using chloride precursors, the main by-product is HCl which is neutralized in an associated gas scrubber [29].

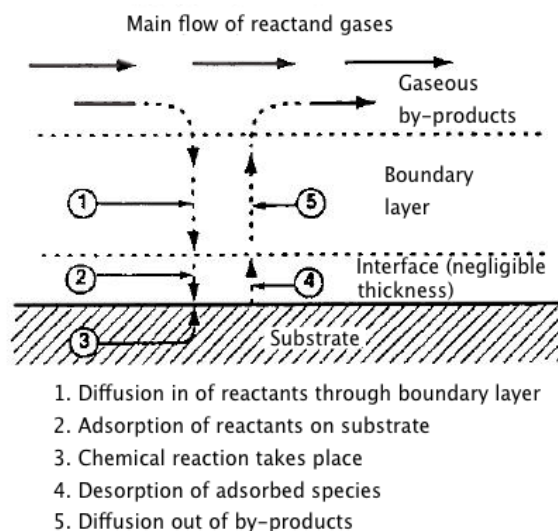


Fig. 3: Sequences of events during a CVD process [29].



The rate determining step of the deposition process is given by the deposition parameters. Substrate temperature, deposition pressure and gas velocity influence the boundary layer thickness and the diffusion rate as illustrated in Fig. 4. When a low pressure deposition process (i.e. low pressure CVD, LPCVD) is applied, the boundary layer thickness decreases due to increased gas velocities and decreasing molecular density, which results in a faster diffusion of reactants and by-products (c.f. Fig. 4 a). The deposition at higher pressures consequences lower gas velocity, which leads to an increased boundary layer thickness (c.f. Fig. 4b). The diffusion rate increases with increasing temperature according Arrhenius law [29].

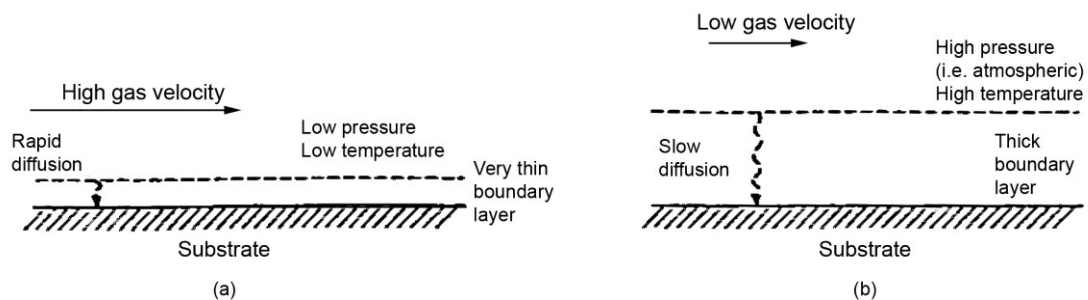


Fig. 4: Boundary layer thickness for low pressure (a) and high pressure deposition (b) [29].

The limitation of the deposition process can be expressed using an Arrhenius plot of deposition rate versus the deposition temperature shown in Fig. 5. With increasing deposition pressure from  $P_1$  over  $P_2$  to  $P_3$ , the mass transport limitation becomes more and more dominant; the deposition rate decreases and the transition from a mass transport controlled regime to a surface kinetics controlled region is shifted to lower temperatures [29, 35].

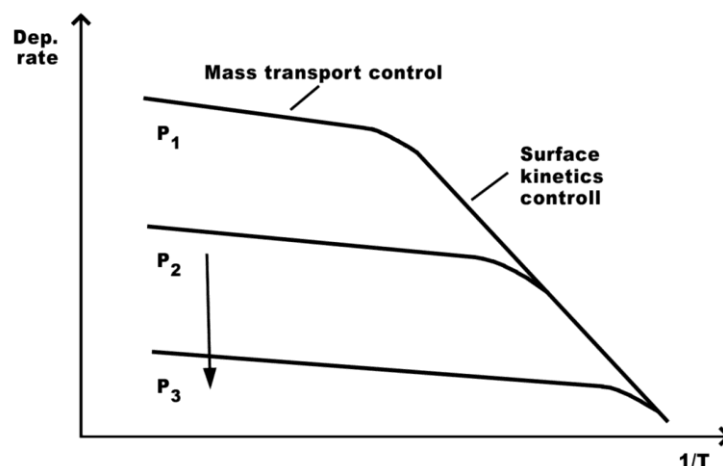


Fig. 5: Regions of mass transport limitation (high  $p$  and  $T$ ) and surface kinetics control (low  $p$  and  $T$ ) at different total pressures ( $P_1 < P_2 < P_3$ ) [35].

In combination with the deposition rate, the developing coating structure is strongly affected by the deposition parameters and feed gas composition. Cheng et al. [36] suggested a model for the structure of TiCN coatings for different deposition temperatures and gas mixtures (c.f. Fig. 6). In

numerous other studies, not only the influence of deposition parameters on the crystal shape of different layer systems like TiC, TiCN, TiN [36-40] as well as  $\text{Al}_2\text{O}_3$  [13, 14] but also by the use of doping agents [41-50] is presented.

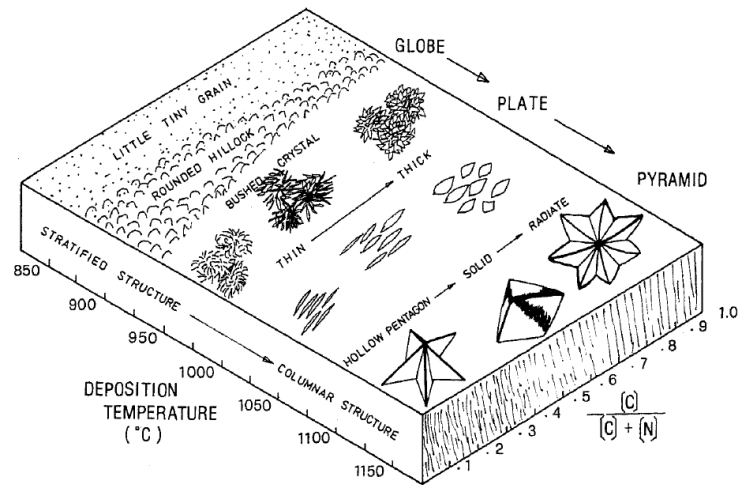


Fig. 6: Dependence of the morphology of TiCN coatings on their deposition temperature and composition [36].

Wagner et al. [37] pointed out that material properties like hardness not only depend on the chemical composition, but also on the microstructure. Consequently, an often followed goal is to design a deposition system and coating architecture to synthesize the selected materials and interfaces in an economic way in the desired structure, depending on deposition parameters and required gas preheating, as homogeneously as possible on thousands of inserts within one batch.

### 3 Coating systems for cutting inserts

#### 3.1 Historic development of TiN/TiCN/Al<sub>2</sub>O<sub>3</sub> coating systems

The evolution of coatings for indexable cemented carbide inserts started in 1969, where the first TiC coated inserts were presented. This few micron thick coating with enhanced wear resistance and chemical inertness increased the lifetime of the inserts significantly. The combination of TiC, TiCN and TiN coatings led to a further improvement of oxidation resistance and durability for the first multilayered coatings. One example of such a graded multilayer coating was the “Goldmaster” coating from Plansee Tizit, which was introduced in 1973 (c.f. Fig. 7).



Fig. 7: Goldmaster GM35 coating, total thickness of 12 µm with a coating architecture of TiC, four layers TiCN, with increasing nitrogen content and TiN, introduced in 1973 [51].

These properties were further enhanced by the introduction of Al<sub>2</sub>O<sub>3</sub> as coating material in 1975 [4, 5, 52-54]. The coating thickness of the early Al<sub>2</sub>O<sub>3</sub> layers was limited, because of the “dog bone” effect, where the deposition rate at the edges of the substrate is higher than on flat surfaces. This effect could be suppressed by the use of H<sub>2</sub>S as catalytic doping agent, which made it possible to deposit thick uniform Al<sub>2</sub>O<sub>3</sub> coatings [55] and increased the total deposition rate [44-46]. The first coatings were often mixtures of fine grained κ-Al<sub>2</sub>O<sub>3</sub> beside coarse α-Al<sub>2</sub>O<sub>3</sub> grains [56, 57]. Pure κ-Al<sub>2</sub>O<sub>3</sub> coatings can be grown on non-oxidized TiC, TiCN and TiN surfaces, when the oxygen partial pressure can be set to a minimum level. The adherence of those κ-Al<sub>2</sub>O<sub>3</sub> coatings is further enhanced by the use of bonding layers [10, 16, 58-60]. The transformation of metastable κ- to the thermodynamic stable α-Al<sub>2</sub>O<sub>3</sub> phase during the deposition process or application is coupled with a volume contraction of 7 vol.-%, resulting in cracks which deteriorate the coating performance.

### 3.2 $\kappa$ - to $\alpha$ -Al<sub>2</sub>O<sub>3</sub> phase transformation

The transformation of the metastable  $\kappa$ -Al<sub>2</sub>O<sub>3</sub> into the stable  $\alpha$ -Al<sub>2</sub>O<sub>3</sub> during the deposition process [61], during cutting operation [62, 63] or ex-situ [64-68] was investigated extensively. Tab. 1 gives an overview of the existing literature. The speed of transformation depends beside time and temperature strongly on the boundary conditions like atmosphere and pressure and can also be influenced by doping agents. These effects were investigated in detail by Hochauer et al. [69], who showed an increased transformation time when using vacuum instead of argon atmosphere and a slowdown of transformation due to the addition Ti and B. Further optimization was shown by Okude et al. [70] by using Zr for the stabilisation of the  $\kappa$ -Al<sub>2</sub>O<sub>3</sub> phase.

Tab. 1: Survey of publications dealing with  $\kappa$ -Al<sub>2</sub>O<sub>3</sub> coatings and the  $\kappa$  to  $\alpha$ -Al<sub>2</sub>O<sub>3</sub> phase transformation, including the used parameters

Author Year	Treatment	Temperature /Material	Pressure/ Tool geometry	Atmosphere/ Cutting parameters $v_c/f/a_p$	Duration	Al <sub>2</sub> O <sub>3</sub> thickness BL=Bilayer ML=Multilayer n = Number of layers
Chatfield 1989 [71]	ex situ	1030 °C	101.3 kPa	H <sub>2</sub>	60 / 120 / 180 min	$\alpha + \kappa$ 1 $\mu$ m
Skogsmo 1992 [64]	ex situ	1050 °C	101.3 kPa	Ar 100 l/h	60 / 200 min	$\kappa$ 4 $\mu$ m
Vuorinen 1992 [65]	ex situ and in situ	1030-1090 °C 1040 °C	101.3 kPa	Ar 100 l/h	7 - 500 min 180 min	$\kappa$ 4 $\mu$ m
Lindulf 1994 [66]	ex situ	1010-1090 °C	5 mPa	vacuum	30 - 1200 min	$\kappa_{ML}$ 8 $\mu$ m n = 8, 15, 32
Hansson 1995 [67]	ex situ	1030-1090 °C	5 mPa	vacuum	20 - 540 min	$\kappa$ 1 / 8 $\mu$ m
Larsson 1997 [72]	ex situ	1050 °C			270 min	$\alpha/\kappa$ 8 $\mu$ m
Ruppi 1997 [73]	longitudinal cutting	34CrNiMo6	SNUN 120412 WC-5.5 % Co, 9 % CC	200,250,275/ 0.4/2.5	1, 3, 6, 10 min	$\kappa_{ML}$ 8 $\mu$ m n = 1, 4, 8, 15, 32
Ruppi 1997 [74]	ex situ	1050 °C	SNUN 120412 WC-5.5 % Co, 9 % CC	Ar	100 min	1 $\mu$ m
Larsson 1998 [68]	ex situ	1030 °C	5 mPa	vacuum	0 - 420 min	$\kappa_{ML}$ 8 $\mu$ m n = 8
Larsson 1999 [62, 63]	longitudinal cutting	C45E	SNUN 120412 WC-5.5 % Co, 9 % CC	200/0.4/2.5 dry	1, 6, 10 min	$\kappa_{ML}$ 8 $\mu$ m n = 8
Osada 2006 [61]	in situ and ex situ	1020 °C		H <sub>2</sub>	120 min	$\alpha/\kappa$ 7 $\mu$ m
Fallqvist 2007 [75]	cutting abrasion test	34CrNiMo6	SNUN 120412 WC-5.5 % Co, 9 % CC			$\kappa_{ML}$ 8 $\mu$ m n = 1, 8, 15, 32
Hochauer 2010 [69]	ex situ	1000 °C	1 mPa / 101.3 kPa	vacuum, Ar, N <sub>2</sub>	0 - 1920 min	$\kappa_{BL}$ 2x1 $\mu$ m

Fig. 8 shows a detailed investigation on a worn cutting insert used in steel turning operation, using focused ion beam (FIB) milling. A cross-section was prepared at the end of tool live close to the crater wear region, where the maximum temperature can be assumed. An intense crack network, shown in Fig. 8c, developed due to the  $\kappa$  to  $\alpha$ -Al<sub>2</sub>O<sub>3</sub> phase transformation. This network can be clearly distinguished from the thermal cracks of CVD coatings in the virgin state after the deposition process visible in Fig. 8d. Formation of this network results in low coating cohesion, which is limiting the tool life when stainless steels or cast iron should be machined. Crack formation can be retarded when  $\kappa$ -Al<sub>2</sub>O<sub>3</sub> multilayer coatings are applied.

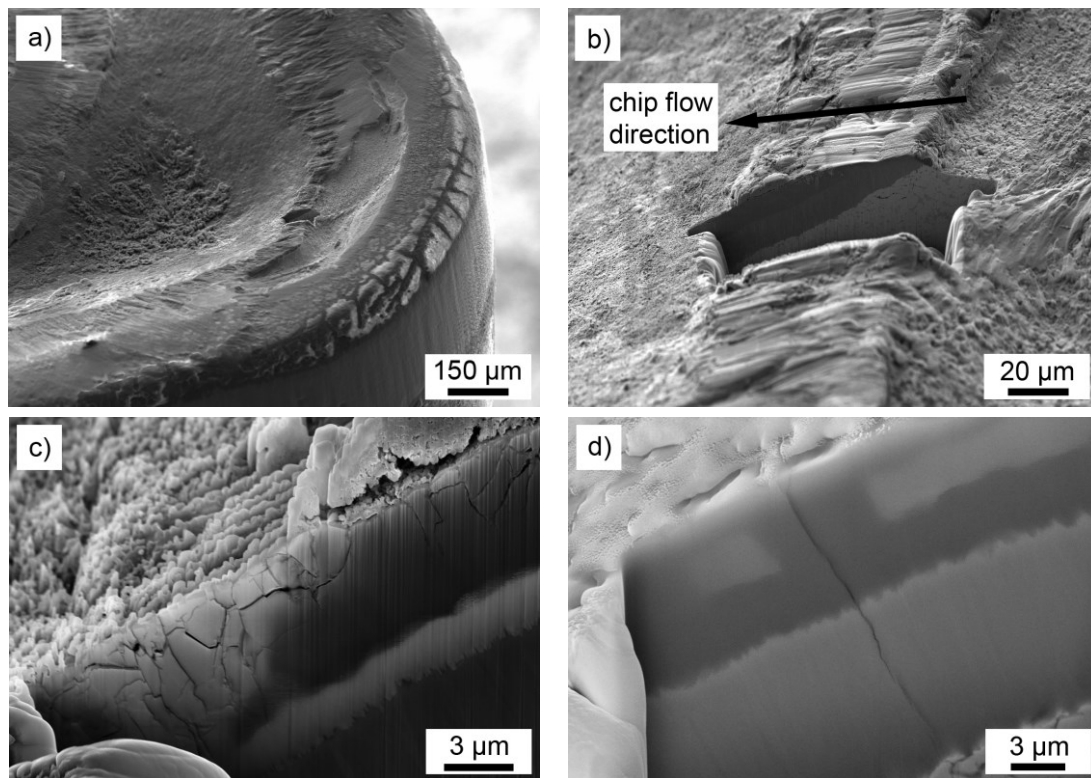


Fig. 8: Detailed scanning electron microscopy investigation of the  $\kappa$ - $\alpha$   $\text{Al}_2\text{O}_3$  transformation of a worn cutting tool (CNMG 120408EN-TM P15 grade WC-Co 6 % Co) in steel turning operation using 42CrMo4 (DIN 1.7225) work piece material, cutting speed  $v_c = 260$  m/min, feed rate  $f = 0.4$  mm/rev, depth of cut  $a_p = 3$ -2-1 mm with cooling lubricant: (a) overview and location of FIB milled cross-section, (b) cross-section close to the crater wear region, (c) crack network of the  $\kappa$ - $\text{Al}_2\text{O}_3$  coating due to the  $\kappa$ - to  $\alpha$ - $\text{Al}_2\text{O}_3$  transformation and (d) virgin insert showing a thermal crack [own work].

The use of multilayer oxide coatings was also very common during the 80ies of the last century. Due to renucleation at the interlayer, the  $\text{Al}_2\text{O}_3$  grain size could be reduced, which led to a decrease in surface roughness. Halvarsson et al. [76] reported an optimum number of 8 interlayers, which yielded superior cutting performance and transverse rupture strength. An example is given in Fig. 9, where a  $\kappa$ - $\text{Al}_2\text{O}_3$  coating was interrupted by TiN-TiNB-TiN interlayers. However, it should be noted that the adherence of the interface and its porosity was frequently the limiting factor in cutting operation [56, 59, 76-80].

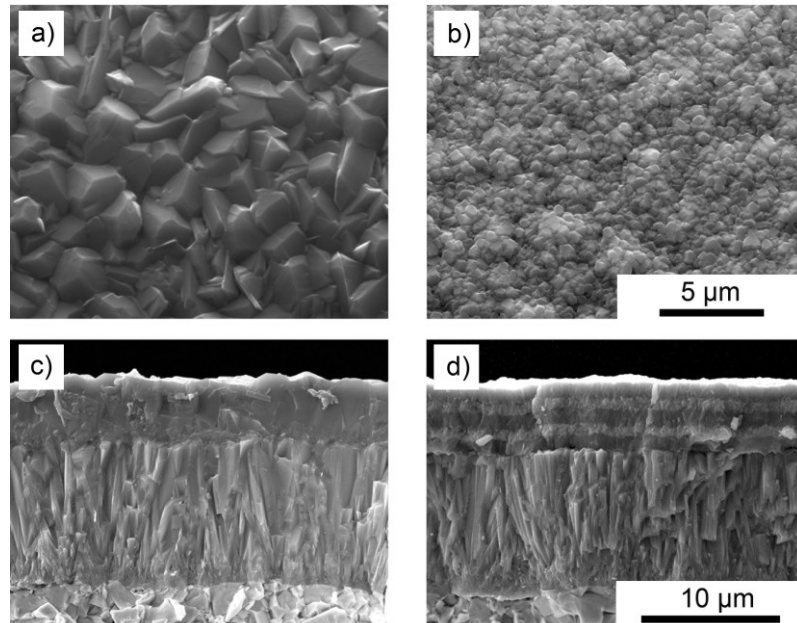


Fig. 9: Comparison of single layer (a & c) and multilayer ( $n = 3$ , b & d)  $\kappa$ - $\text{Al}_2\text{O}_3$  coating on a medium temperature TiCN base layer with respect to grain size in scanning electron microscopy top view micrographs and fracture cross-sections [81].

### 3.3 Improved $\alpha$ - $\text{Al}_2\text{O}_3$ coatings and interlayers

An important step in process technology occurred in the 90ies of the last century, when computer controlled deposition systems were introduced [32]. This increased the flexibility in coating architecture, enhanced the reproducibility of the coatings and made it possible to define very short sensitive steps and ramping functions. Due to the improved control of leakage rate and oxygen partial pressure during interlayer deposition and during the initial growth of the  $\text{Al}_2\text{O}_3$  layer, it was possible to deposit pure  $\alpha$ - $\text{Al}_2\text{O}_3$  coatings with high reliability [56, 78]. Starting in 1992, numerous patents were composed to obtain well defined (012) [82, 83], (104) [84] and (110) [85] texture of  $\alpha$ - $\text{Al}_2\text{O}_3$ . Also the differences of as deposited and thermally transformed  $\alpha$ - $\text{Al}_2\text{O}_3$  coatings were studied [72]. Osada et al. [61] pointed out that  $\alpha$ - $\text{Al}_2\text{O}_3$  coatings transformed immediately after coating deposition without prior cooling down to room temperature have also superior wear resistance, compared to  $\kappa$ - $\text{Al}_2\text{O}_3$  coatings or ex-situ transformed ones.

In the end of the last century an interlayer was claimed by Holzschuh, containing the  $\text{Al}_2\text{TiO}_5$  phase, resulting in an further improved adhesion [60]. Especially in combination with this interlayer, the growth orientation of the  $\alpha$ - $\text{Al}_2\text{O}_3$  was forced to (0001), e.g. an (006) texture. X-ray diffraction (XRD) measurements [86] of such a coating from the year 2001 on a Walter WAK20 insert [87], exhibiting a coating architecture of 0.5  $\mu\text{m}$  TiN, 7.5  $\mu\text{m}$  TiCN, 1.0  $\mu\text{m}$  Ti-Al-C-N-O, 10.8  $\mu\text{m}$   $\alpha$ - $\text{Al}_2\text{O}_3$  and a 0.3  $\mu\text{m}$  TiN top coating, are shown in Fig. 10, as well as the calculated orientation density function (c.f. Fig. 11). The (006)  $\alpha$ - $\text{Al}_2\text{O}_3$  peak, indicated in the  $\theta$ -2 $\theta$  scan, can be misinterpreted as TiC peak, which is close to this location. An unambiguous confirmation can be provided by pole figure measurements, especially when the peak intensity is low [88].

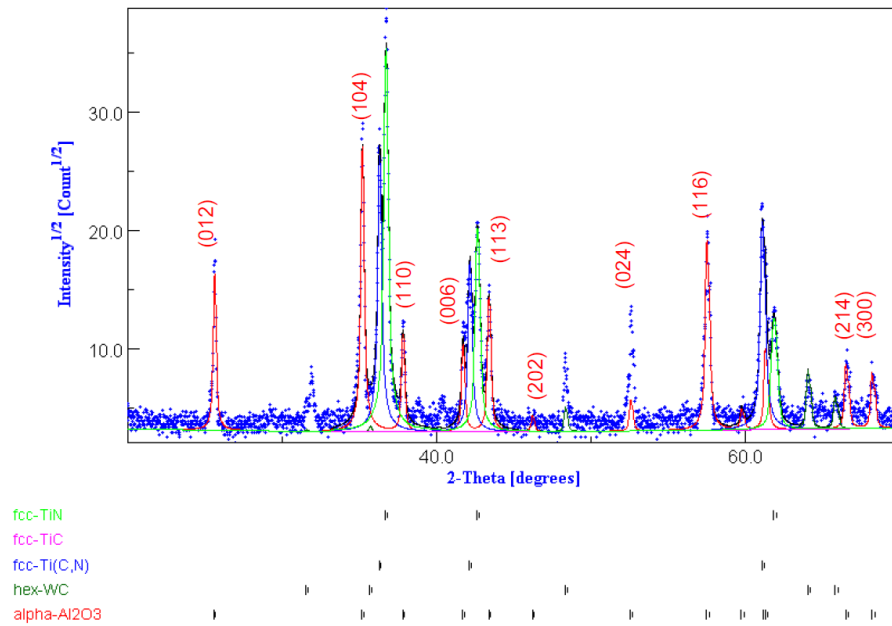


Fig. 10: X-ray diffractogram determined in  $\theta$ - $2\theta$  geometry using  $\text{Cu } k_{\alpha}$ -radiation; Walter WAK20 (2001) [86, 87]

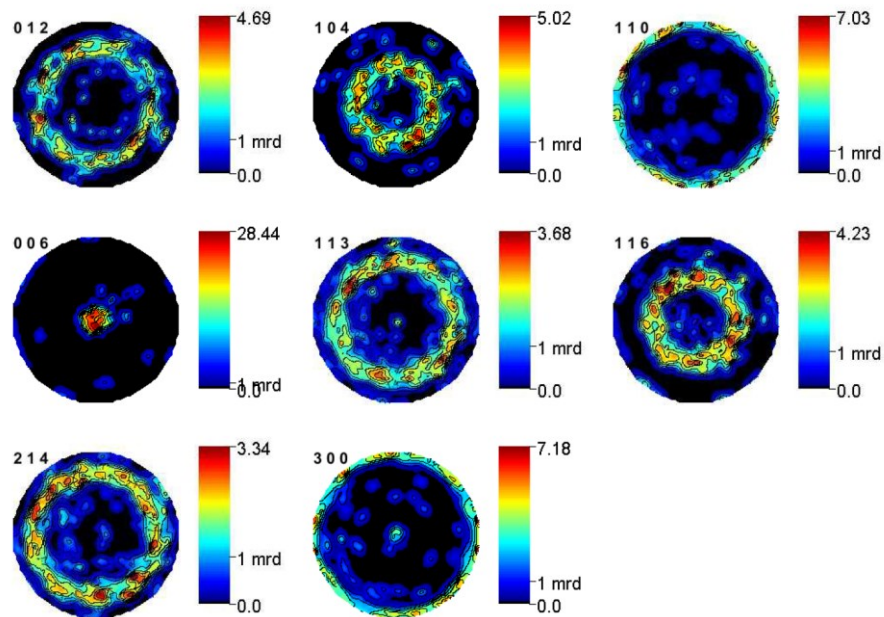


Fig. 11: Calculated orientation density function (ODF) of the measured (104), (113), (116) and (012) pole figures, using a maximum azimuth angle of  $90^\circ$ ; Walter WAK20 insert (2001) [86, 87].

Most of the patents claiming  $\alpha\text{-Al}_2\text{O}_3$  estimated the preferred orientation by the texture coefficient. This is done by using the maximum peak intensity [89, 90] in relation to JCPDF cards of  $\alpha\text{-Al}_2\text{O}_3$  according to eq. 1, where  $I(\text{hkl})$  is the measured maximum peak intensity and  $I_0(\text{hkl})$  is the value from the JCPDF reference. Depending on the number of reflections  $n$ , which are taken into account, the absolute value of TC can vary.

$$\text{TC}(\text{hkl}) = \frac{I(\text{hkl})}{I_0(\text{hkl})} \cdot \left[ \frac{1}{n} \sum_{n=1}^n \frac{I(\text{hkl})}{I_0(\text{hkl})} \right]^{-1} \quad (1)$$

This is demonstrated in Tab. 2, where all peaks which can be clearly distinguished from those originating from the substrate and the base layer are taken into account. A comparison of this calculation with those used in patents [91-94] by arbitrary selecting peaks is made. Here it can be seen that the magnitude of TC changes significantly, which is coupled also with the low standard intensity  $I_0(006)$  of 2 %. If peaks of low standard intensities are not taken into account, a misinterpretation of texture is possible. Another weakness of this method is that only the maximum intensity of the peaks was used. Peak broadening is caused by decreasing crystallite size, coupled with a decrease of maximum peak intensity while the integral peak intensity remains constant. The second approach is more significant in XRD analysis, especially when fine grained structures are desired [88, 95].

Tab. 2: Maximum peak intensity and calculated TC values based on an XRD  $\theta$ - $2\theta$  scan (c.f. Fig. 10) on a Walter WAK20 insert (2001) [87]; [own work].

Peak (hkl)	$2\theta$ [°]	I [%]	$I_0$ JCPDF 46-1212 [%]	$I/I_0$	TC (n=10) all peaks	TC (n=6) (012), (104), (110), (113), (024), (116)	TC (n=7) (012), (104), (110), (113), (024), (116), (300)	TC (n=8) (012), (104), (110), (006), (113), (202), (024), (116)	TC (n=6) (012), (104), (110), (006), (113), (116)
(012)	25.584	33.8	45	0.75	0.56	1.08	1.15	0.48	0.38
(104)	35.137	100.0	100	1.00	0.74	1.44	1.53	0.64	0.50
(110)	37.785	15.7	21	0.75	0.56	1.08	1.14	0.48	0.37
(006)	41.685	16.8	2	8.40	6.25			5.35	4.21
(113)	43.363	27.4	66	0.42	0.31	0.60	0.64	0.26	0.21
(202)	46.184	0.0	1	0.00	0.00			0.00	
(024)	52.553	19.5	34	0.57	0.43	0.83	0.88	0.37	
(116)	57.519	59.7	89	0.67	0.50	0.97	1.03	0.43	0.34
(214)	66.548	10.6	23	0.46	0.34				
(300)	68.198	11.2	27	0.41	0.31		0.63		
Calculation according patent						EP0603144B1 [91]	US20040202877A1 [92]	WO2008094104A1 [93]	EP1953258B1 [94]
Date of filing						1993	2004	2008	2008
Sum of TC taken into account						10.0	6.0	7.0	8.0

### 3.4 The evolution of base layer systems

Parallel to the improvements regarding to  $Al_2O_3$ , the medium temperature process for the deposition of the TiCN base layer (MT-TiCN) using  $CH_3CN$  and  $TiCl_4$  as precursor materials substituted the former process using  $CH_4$ ,  $N_2$  and  $TiCl_4$  almost completely in the mid 90ies of the last century. Beside the columnar structure, the main advantage of the MT-TiCN process is the suppression of the undesired  $\eta$ -phase formation in the cemented carbide [21, 96-99], due to the lower deposition temperature of 800 to 900 °C, compared to the 930 to 1050 °C necessary for the process using  $CH_4$  as carbon source. These high temperatures are needed to break the strong C-H bonds of  $CH_4$  [4, 100], but have a significant effect on the substrate material. Lee et al. [98] presented a schematic model of the  $\eta$ -phase formation shown in Fig. 12 and investigated the



influence on the deposition conditions. An increase of  $\eta$ -layer thickness was reported with increasing temperature and increasing Co content of the substrate material, where the diffusion is faster than in WC. The  $\eta$ -phase nucleates at the interface of WC grains in the surface near region and is mainly influenced by the diffusion of C in Co, that means that this process strongly depends on temperature as well as Co content of the cemented carbide.

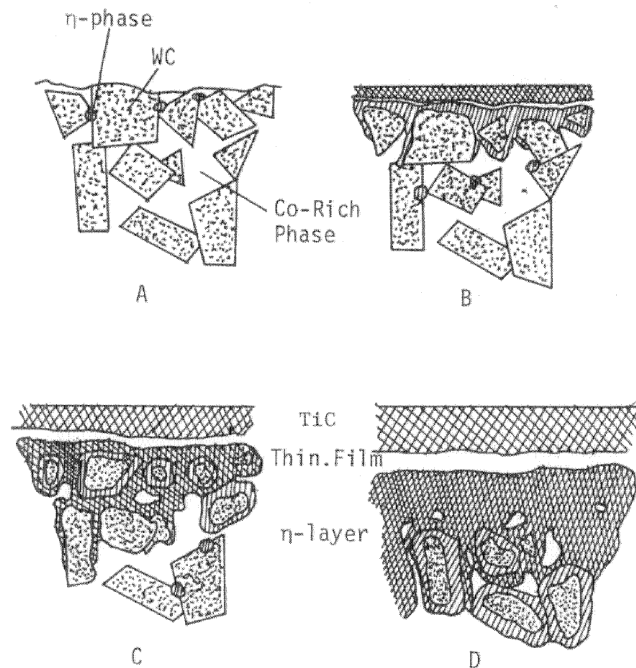


Fig. 12: Schematic model showing the nucleation and growth of the  $\eta$ -layer; (a) nucleation preferentially at the interface between WC grains near the surface, (b) growth of  $\eta$ -phase around WC grains proceeded by diffusion processes, (c)  $\eta$ -phase partially embedding WC grains, (d) Cessation of growth by reaching the solubility limit of W in Co-rich phase [98].

Due to the fact that this process is driven by diffusion, the formation of the  $\eta$ -phase (c.f. Fig. 13) occurs preferentially on edges, especially where the toughness of cutting tools is needed.

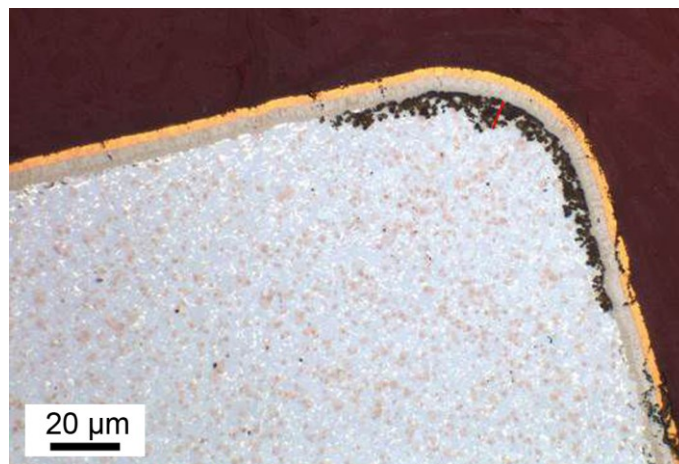


Fig. 13: Optical microscopy cross-section after Murakami etching of a Sandvik GC425 insert (1987) [101] with TiC-TiCN-TiN coating (8.5  $\mu\text{m}$ ) and pronounced  $\eta$ -phase at the cutting edge [own work].

This effect can also be shown when a 0.7  $\mu\text{m}$  thick TiN layer is deposited at 920  $^{\circ}\text{C}$  on polished cemented carbide inserts. As seen in Fig. 14, the TiN nucleates on the triangular WC grain epitaxially [4, 102]. A higher growth rate occurs close to the Co binder region, where the C is mobile, diffuses and reacts with the  $\text{TiCl}_4$  and  $\text{N}_2$  of the gas atmosphere to TiCN. This results in porosity at the interface as well as  $\eta$ -phase formation in the uppermost region of the substrate material. Such a TiN interlayer with well adapted deposition condition is necessary to minimize diffusion and porosity, and growth a well adherent, columnar MT-TiCN on top.

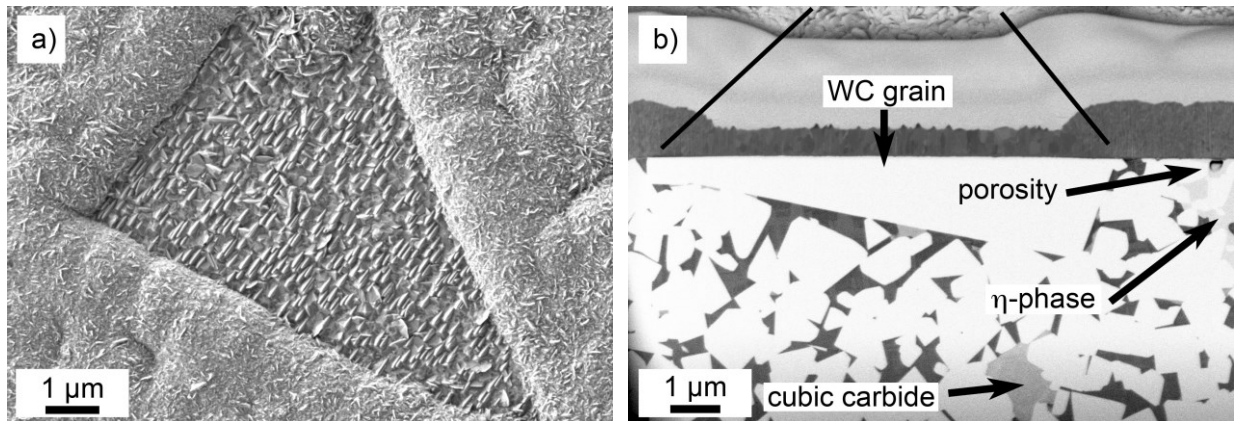


Fig. 14: Scanning electron microscopy top view (a) and FIB cross-section (b) of a 0.7  $\mu\text{m}$  TiN coated, polished WC-Co cemented carbide insert exhibiting 9 wt.% Co and 4 wt.% cubic carbides. The higher growth rates close to the Co binder, epitaxial growth of TiN on WC grain as well as porosity due to C diffusion and consequently reaction with  $\text{TiCl}_4$  to TiCN can be seen [own work].

In the end of the 1980ies, Kübel [103-106] demonstrated the increased lifetime and enhanced toughness of the MT-TiCN coatings compared to standard CVD TiCN and TiCN coatings grown by physical vapour deposition (PVD) in interrupted cutting and milling operations. It was also stated that this performance can be even further enhanced by the combination with  $\text{Al}_2\text{O}_3$  [104, 107]. Further improvements were made by controlling the crystal orientation and refining the columnar structure. There, additional species like B [43, 108], CO [41, 109] and different hydrocarbons [110] can be used. The effect of such an addition on the morphology of the coating is shown for the example of CO addition in Fig. 15.

Beside the use of  $\text{CH}_3\text{CN}$  in MT-TiCN coatings, also other approaches are reported to lower the deposition temperature for increased toughness of the tool. Investigations were done for TiNB and ZrBN coatings in a temperature range of 850-1050  $^{\circ}\text{C}$  [111, 112], while also the use of hydrocarbons like  $\text{C}_2\text{H}_6$  at 920  $^{\circ}\text{C}$  is feasible [113, 114]. For a further decrease of deposition temperature, more reactive precursors like metal organic compounds or ammonia are necessary [115].

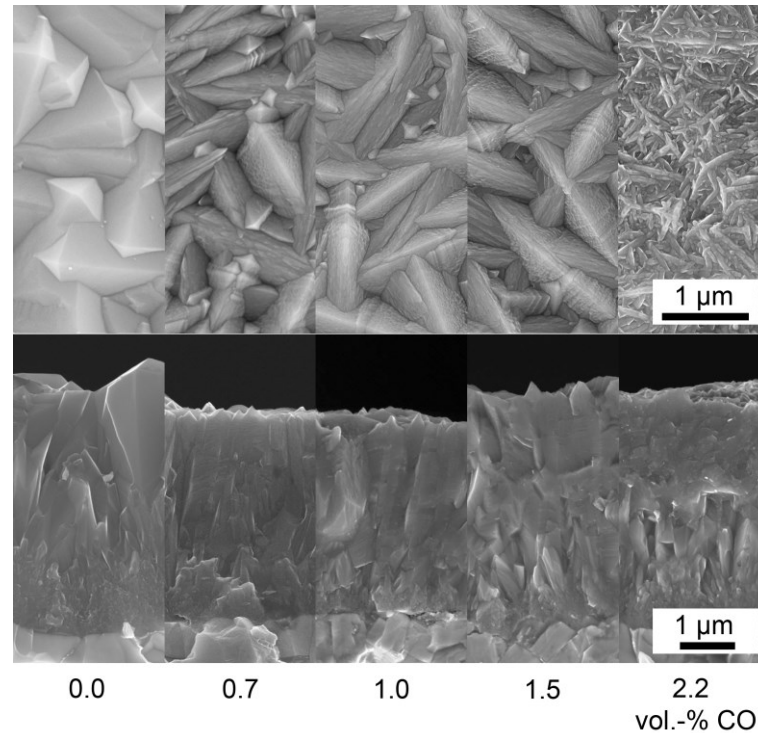


Fig. 15: Scanning electron microscopy surface images (top row) and fracture cross-sections (bottom row) of the  $MT-TiC_xN_{1-x}$  based coatings as function of the CO fraction in the feed gas [109].

### 3.5 Crystal orientation of $\alpha-Al_2O_3$

Within the last three decades, the main focus in patents and scientific literature was set to the well-defined growth of selected  $\alpha-Al_2O_3$  crystal orientations. Beside the systematic (012), (104) and (110) orientation, the (300) and (006) orientation could be synthesized via CVD. The anisotropic material properties and wear behaviour could be correlated with the orientation of the  $\alpha-Al_2O_3$  crystals and it could be shown that the (0001) growth orientation has the most beneficial properties in cutting application [13, 116-118]. A preferred (0001) growth orientation has also the advantage of a lower surface roughness due to formation of flat crystals, as illustrated in Fig. 16. Nearly all of the CVD coatings for cemented carbide cutting tools applied in turning, milling, parting or grooving show the above described TiN/MT-TiCN/ $Al_2O_3$  coating architecture, where  $\alpha-Al_2O_3$  is nowadays the most frequent polymorph. Depending on the cutting application, also TiN or TiCN top coatings can be applied for a better determination of flank wear, which can be removed on the cutting edge or the flank face due to suitable post treatment processes [119].

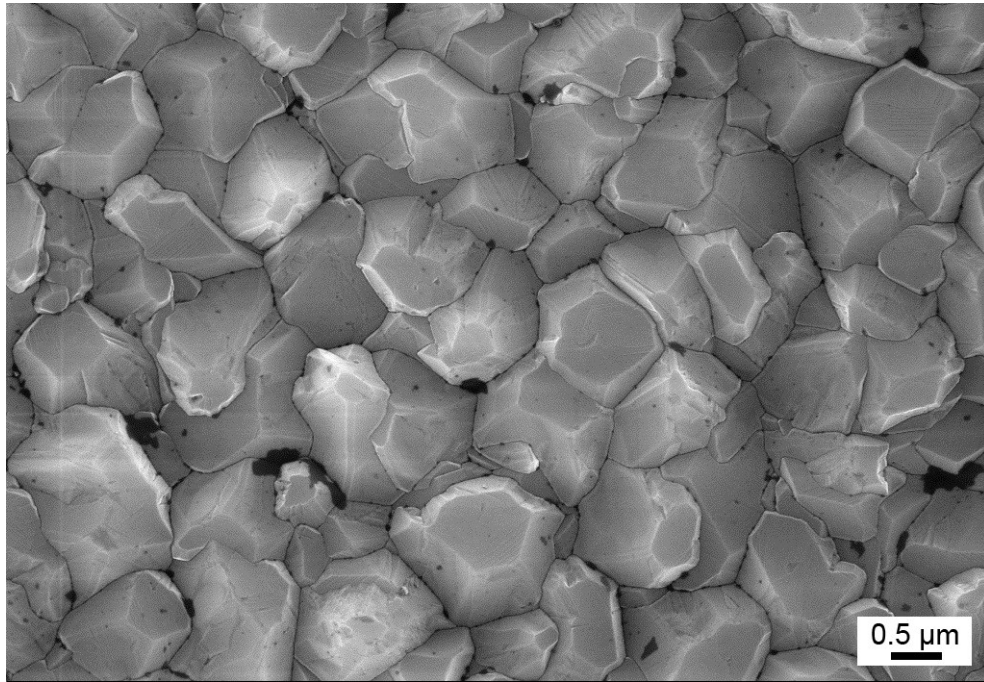


Fig. 16: Scanning electron microscopy top view image of an 8 μm (0001) oriented  $\alpha$ -Al<sub>2</sub>O<sub>3</sub> coating on a MT-TiCN base layer. The flattened domes of the crystals correspond to the (0001) basal plane [own work].

### 3.6 Post treatment of coatings and residual stresses

For different reasons, post treatment processes are applied for CVD hard coatings. In the beginning, they were used to obtain a homogenous colour and to smoothen the surface, especially the cutting edge of the inserts. Different processes, mainly brushing and wet or dry abrasive blasting with different media, can be applied. By using metallic blasting media, also the transfer of material can influence the uppermost region of the coating due to adhering blasting material. With this method, the tribology of the chip flow on the rake face can be influenced [120, 121].

One of the most important steps for an effective post treatment process is the improvement of coating adhesion, more precisely the adhesion of Al<sub>2</sub>O<sub>3</sub> due to optimized bonding layers, as explained in section 3.3. Now the residual tensile stresses, which are caused by the difference in thermal expansion coefficient of substrate and coating, coupled with the high deposition temperatures can be decreased by an intense blasting process. In combination with the (0001) oriented  $\alpha$ -Al<sub>2</sub>O<sub>3</sub> coating (c.f. Fig. 11), the famous TigerTec coating from Walter made it possible to change the residual stresses from tensile to compressive [22-24]. The TigerTec appearance with the black rake face, where the top coating was removed, and the yellow or silver flank face for better wear detection [119] was extended to nearly all products of Walter and the Sandvik Coromant Group (c.f. Fig. 17).



Fig. 17: Advertising of TigerTec product introduction in September 2001, extension within the Coromant Group to Sandvik GC3215 and further grades in 2003 and Walter news presenting the PVD-TigerTec coatings at the EMO exhibition 2005 in Hannover.

Fig. 18 shows the residual stress gradient of several post treated  $\alpha$ - $\text{Al}_2\text{O}_3$  coatings, measured from their surface. The high residual compressive stresses in the uppermost region of the coatings result in an increased toughness, especially at the cutting edge in interrupted cutting operations [23]. This effect can also be applied for other coatings like  $\text{Al}_2\text{O}_3$  [25, 26, 122], TiAlN [123] or PVD-TiAlN [124-127], but is limited by the adhesion of the coating.

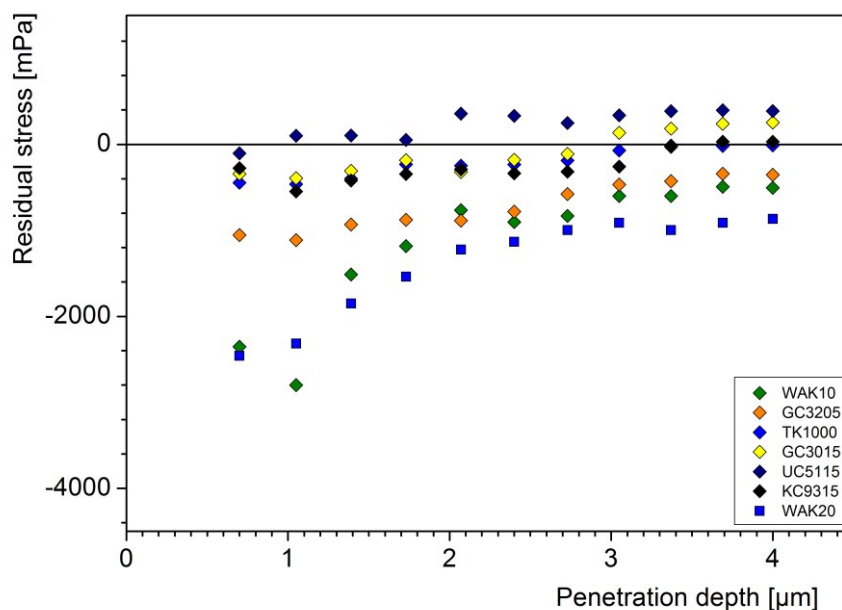


Fig. 18: XRD residual stress profiles determined using the  $\sin^2\psi$  method on post treated  $\alpha$ - $\text{Al}_2\text{O}_3$  coatings. Measurements were done on the rake face of CNMA 120408EN cutting tools of: Walter WAK10 (2006) [128], Walter WAK20 (2010) [129], Sandvik GC3205 (2006) [130], with removed top coating on the rake face (TigerTec), in comparison to Seco TK1000 (2006) [131], Mitsubishi UC5115 (2006) [132], Kennametal KC9315 (2006) [133] and Sandvik 3015 (2006) [134]; [own work].

For the modification of residual stresses of coated indexable inserts, mainly wet and dry abrasive blasting processes were used. Beside the pressure, i.e. particle velocity and exposure time, the material and shape of the blasting media is of major importance. Sharp edged as well as round blasting media are available in various grit sizes, which results in a huge variety of contact radii active during impact on the coating surface. In combination with the elastic and plastic material behaviour of the blasting media and work piece material, i.e. the relation of their hardness values, the elementary behaviour can be predicted. Schalk [135] showed the generation of residual tensile stresses and recovery due to thermal treatment for blasted  $\alpha$ - and  $\kappa$ -Al<sub>2</sub>O<sub>3</sub>. Two main processes, namely the Hertzian pressure showing a residual stress maximum underneath the surface and plastic stretching with the residual stress maximum at the surface, can be distinguished (c.f. Fig. 19). For hard coatings, treated with ceramic blasting media, behaviour according to Hertzian pressure is common [24, 124, 136].

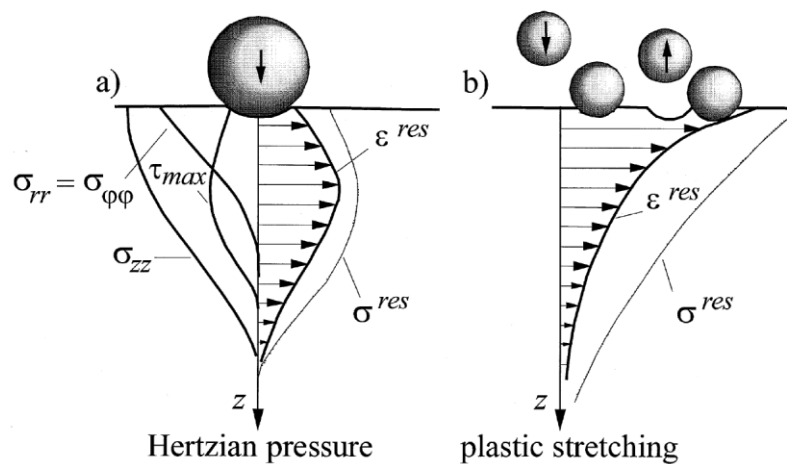


Fig. 19: Elementary processes and stress distribution due to blasting [137].

Schiffner and Droste gen. Helling [136] presented a numerical model, verified by experimental results, which illustrates the influence of the major process parameters. The residual stress gradient, the main investigated quantities and the influence of particle velocity and contact radius is illustrated in Fig. 20. The particle energy at the impact can be correlated to the particle radius, in combination with the density to the mass of the particle and the velocity. For the post treatment of multilayered hard coatings, most frequently the maximum energy is limited by the coating adhesion at the cutting edge.



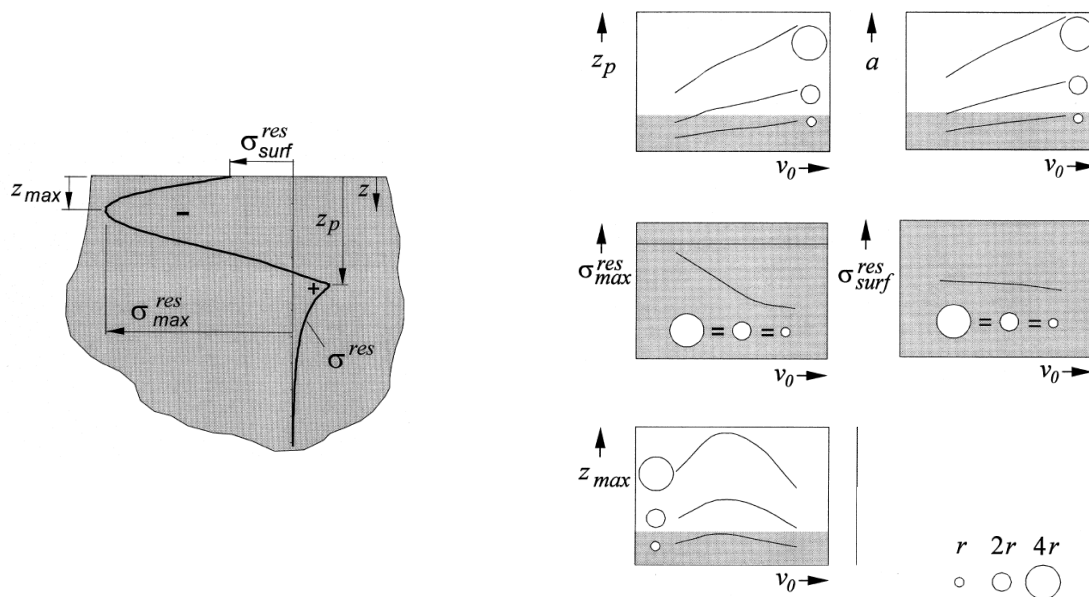


Fig. 20: Definition of the investigated quantities and calculated results for different parameters using 42CrMo4 work piece material. Contact radius  $r = 0.2\text{-}1.0$  mm, particle velocity  $v_0 < 100$  m/s, assuming that the spheres are much stiffer than the work piece material [136].

The development of residual stresses due to deposition conditions, the resulting microstructure and texture coupled with anisotropic material behaviour in combination with post treatments increased the necessity for a more detailed understanding of residual stress gradients. One very important part for this knowledge base is the improvement of stress measurement techniques for CVD multilayer coatings. Beside the classical XRD methods,  $\sin^2\phi$  and multiple hkl methods [88] using synchrotron radiation were developed. Klaus et al. presented a method using white synchrotron radiation on the surface of a tilted sample and energy dispersive diffraction as well as an angle dispersive approach [22, 23, 138]. The measurement principle is illustrated in Fig. 21a. Drawback of this method is the complex calculation of damping and the exact information depth. A different approach was presented by Keckes et al. [139] using a monochromatic 100 and 250 nm diameter synchrotron radiation beam and a FIB prepared specimen of 50  $\mu\text{m}$  thickness. By moving of the sample perpendicular to the beam and evaluation of the Debye-Scherrer rings, depth resolved microstructure and strain analyses can be conducted with high lateral resolution. The measurement principle is shown in Fig. 21b.

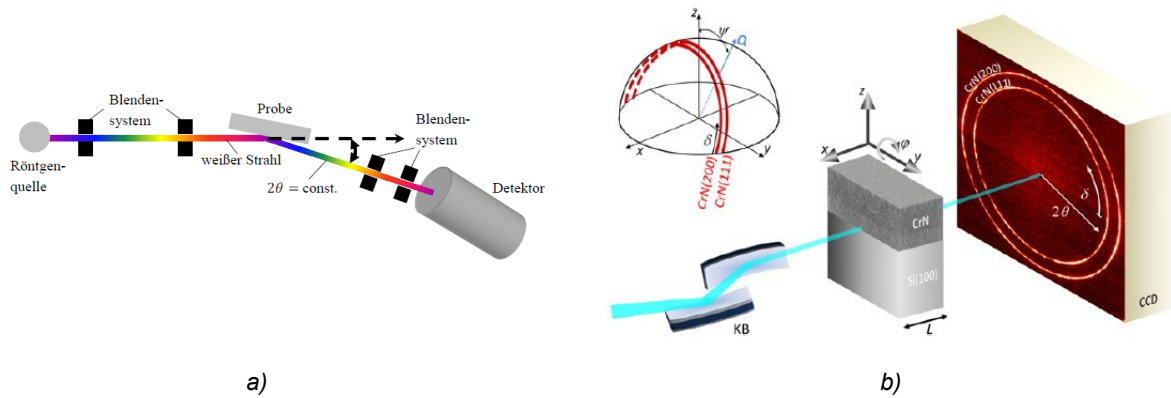


Fig. 21: Methods for depth resolved residual stress analysis presented by Klaus (a) [138] and Keckes et al. (b) [139].

Using this detailed information in combination with the computer controlled deposition systems described in section 3.3, an adapted design of coating architecture including graded layers and interfaces with well adapted post treatment process is feasible. In this context, CVD coatings with very atypical behavior on cemented carbides are highly interesting. Especially CVD  $\text{TiB}_2$  [111, 112, 140, 141] as well as CVD  $\text{TiAlN}$  [115, 123, 142], both showing residual compressive stresses after cooling, are of major interest. The deposition of  $\text{TiB}_2$  using  $\text{TiCl}_4\text{-BCl}_3\text{-H}_2\text{-Ar}$  atmosphere at moderate temperature is a well-known and slow deposition process [112]. In contrast, the deposition of  $\text{TiAlN}$  with  $\text{TiCl}_4\text{-AlCl}_3\text{-NH}_3$  precursors using  $\text{H}_2$ ,  $\text{N}_2$  or Ar carrier gas or mixtures thereof, is a very fast and difficult to control process. A separated gas distribution and inlets are necessary for a large scale production [143, 144].



### 3.7 Future developments - TiAlN coatings via CVD

TiAlN hard coatings have superior properties in cutting applications, compared to TiN and TiCN, when hardness, hot hardness and oxidation resistivity are needed. For PVD hard coatings applied in metal cutting application on cemented carbide substrates, the TiAlN-based systems cover the major proportion of cutting applications [6, 145, 146]. The residual compressive stresses especially in PVD coatings or post treated CVD coatings can lead to significant improvements of tool life [122, 147, 148].

Different attempts were made to deposit TiAlN coatings without plasma assistance using atmospheric pressure CVD (APCVD) or LPCVD. In this case,  $\text{NH}_3$  as reactive precursor for N in combination with  $\text{TiCl}_4$  and  $\text{AlCl}_3$  is necessary. Some of these experiments were performed in laboratory scale, but others also using industrial scale plants. The difficulty regarding to homogeneity is the distribution of coating thickness within the reactor, as well as the homogeneity regarding to phase composition. Several authors observed multicomponent systems with cubic TiN + cubic TiAlN [115, 144], wurtzite AlN + cubic TiAlN [115, 144, 149] or mixtures with nanocrystalline + amorphous structure [150]. Anderbouhr et al. [151] presented a  $\text{Ti}_{0.52}\text{Al}_{0.48}\text{N}$  composition in a single phased cubic structure, which was deposited at 700 °C. Analogously, Madar et al. [152] claimed the deposition of cubic  $\text{Ti}_{1-x}\text{Al}_x\text{N}$  for  $0 < x < 0.6$ , deposited between 550 and 650 °C. While the Al fraction of the  $\text{Ti}_{1-x}\text{Al}_x\text{N}$  coatings in the earlier works was moderate ( $0 \leq x < 0.6$ ), Endler et al. [115, 142-144] and Pitonak et al. [149, 153, 154] documented Al rich coatings up to  $x = 0.98$ . Tab. 3 gives an overview of publications dealing with CVD TiAlN deposition without plasma assistance.

Tab. 3: Overview of publications and corresponding process parameters dealing with CVD deposition of TiAlN without plasma assistance.

Author	Year	Type	Temp.	Gas system	Pressure	Scale
Liu [150]	1996	APCVD	650-850 °C	$\text{TiCl}_4\text{-AlCl}_3\text{-NH}_3\text{-He}$	atmospheric	Lab
Anderbouhr [151]	1997	LPCVD	700 °C	$\text{TiCl}_4\text{-AlCl}_3\text{-NH}_3\text{-Ar-H}_2$	11 mbar	Lab
Anderbouhr [155]	1999	LPCVD	500-700 °C	$\text{TiCl}_4\text{-AlCl}_3\text{-NH}_3\text{-Ar-H}_2$	0.55-1.40 mbar	Lab
Yoshikawa [156]	2001	CVD	700 °C	$\text{TiCl}_4\text{-AlCl}_3\text{-NH}_3\text{-H}_2$	-	-
Wagner [157]	2008	APCVD	550-600 °C	$\text{TiCl}_4\text{-AlCl}_3\text{-NH}_3\text{-Ar}$	atmospheric	Industrial
Endler [115]	2008	LPCVD	800-900 °C	$\text{TiCl}_4\text{-AlCl}_3\text{-NH}_3\text{-H}_2\text{-N}_2$	< 100 mbar	Lab
Endler [142]	2010	LPCVD	800-900 °C	$\text{TiCl}_4\text{-AlCl}_3\text{-NH}_3\text{-H}_2\text{-N}_2\text{-Ar-C}_2\text{H}_4$	< 100 mbar	Lab
Spieß [123]	2010	CVD	< 800 °C	$\text{TiCl}_4\text{-AlCl}_3\text{-NH}_3\text{-?}$	-	Industrial
Pitonak [149]	2013	LPCVD	800 °C	$\text{TiCl}_4\text{-AlCl}_3\text{-NH}_3\text{-H}_2\text{-N}_2$	30 mbar	Industrial

Beside the phase composition of CVD deposited TiAlN coatings, the chlorine content is of major importance, which should be as low as possible for cutting application. A decreasing Cl incorporation, could be reached by increasing deposition temperature, as well as increased  $\text{NH}_3$

fraction [151, 158]. Also a treatment in Ar-NH<sub>3</sub> atmosphere can reduce the Cl incorporation [151]. By the adaption of process parameters, Cl contents < 1 at.% are feasible. Most of the authors reported a strong (200) orientation of the cubic TiAlN phase [150, 155, 156, 159].

The first cutting tool on the market with a CVD AlTiN coating was the TeraSpeed grade (LCK15M) from Böhlerit, which was presented on the EMO 2011 [160, 161]. Early documents stated a nearly pure cubic structure [161, 162], while more detailed investigations showed a mixture of cubic-TiAlN and wurtzite-AlN [149]. Due to the deposition above the thermodynamic equilibrium, the phase separation takes place analogously than observed for PVD coatings [163]. The volume gain of approximately 20 % due to the cubic to wurtzite transformation [164] may be responsible for the residual compressive stresses within these CVD TiAlN coatings.

Beside all difficulties of manufacturing, this system opens a wide playground of coating systems, as already started, e.g., with TiAlCN coatings [142]. At moderate temperatures, the synthesis of metastable coating systems via CVD could be demonstrated, close to deposition temperatures of PVD processes. The implementation of these TiAlN or TiAlCN layers are feasible as base layer [165] or as top coating on a TiCN/Al<sub>2</sub>O<sub>3</sub> multilayer, having residual compressive stresses after the deposition process [166]. The applicability as top coating influencing the stress profile is also shown by Cho et al. [167], who described an Al-rich AlTiSiCrN top coating synthesised via CVD.

## 4 Conclusions and outlook

The aim of this thesis is to enhance the present understanding of the design of wear-resistant CVD multilayer coatings for cemented carbide cutting tools. The evolutionary development of the coatings from the first monolayer TiC to the highly textured TiN/MT-TiCN/ $\alpha$ -Al<sub>2</sub>O<sub>3</sub> coatings with well-defined interfaces is summarized. The effect of post treatment methods, their influence on residual stress profiles and consequently their impact on the lifetime of the cutting tools is reviewed. The most important characterization techniques necessary for a detailed improvement of coating architectures are explained.

Publication I included in this thesis demonstrates that not only the gas composition, but also the gas flow principle is of major importance. The distribution of the precursors significantly influences the homogeneity of coating thickness and structure. This becomes more important, the more reactive the precursor system is. Each layer type of the multilayer coating has a different optimum of deposition conditions like pressure, total gas flow and temperature, which all have to be covered by an optimum compromise of hardware arrangement and process recipes.

Using CVD, a wide range of materials and chemical compositions can be synthesized and combined within a multilayer system. These layer materials differ in their properties and have to be selected in an optimum way to meet the requirements in cutting application. Furthermore, coupled varying parameters like thermal expansion result in stress gradients. The influence of the coating architecture itself on stress gradients at comparable coating thickness as well as the cutting performance is demonstrated in Publication II.

The adaption of a single layer can also be done by using different precursor systems or by modification of microstructure. Publications III and IV show examples, where TiCN layers were deposited using C<sub>2</sub>H<sub>6</sub> as alternative carbon source instead of CH<sub>3</sub>CN. Both systems can be adjusted regarding their microstructure using additional species like CO and BCl<sub>3</sub>. A well-defined amount of additional species led in both cases to grain refinement and enhanced hardness. Both together improved the lifetime in cutting operations. A more detailed understanding of the material properties, especially the interfaces within a multilayer coating, enables the possibility for designing an optimized coating architecture. This can be realized e.g. by graded layers and smooth transitions at the interfaces. In combination with suitable post treatments, in particular the defined introduction of residual compressive stresses, the durability of the cutting inserts can be further improved.

A further progress in the performance of CVD coated cemented carbide tools can be achieved, when the large scale production of multi-layered systems including TiAlN based coatings becomes state of the art. Due to the much more complex deposition conditions and the separated feed gas lines necessary for the highly reactive precursors, an adaption of the hardware and gas supply is essential. When these challenges are solved, a progress due to the superior material properties like hot hardness, oxidation resistance and especially the residual compressive stresses of TiAlN can lead to a significant improvement in cutting performance for a huge range of applications.

## 5 Literature

- [1] T. Childs, K. Maekawa, T. Obikawa, Y. Yamane, *Metal Machining*, John Wiley, 2000.
- [2] G. Byrne, D. Dornfeld, B. Denkena, *CIRP Annals-Manufacturing Technology* 52/2 (2003) 483.
- [3] B. Mills, *Journal of Materials Processing Technology* 56/1-4 (1996) 16.
- [4] S. Ruppi, *Journal De Physique IV* 11/Pr3 (2001) 847.
- [5] S. Söderberg, M. Sjöstrand, B. Ljungberg, *Metal Powder Report* 56/4 (2001) 24.
- [6] D.T. Quinto, *International Journal of Refractory Metals & Hard Materials* 14/1-3 (1996) 7.
- [7] W. Grzesik, *Journal of Materials Processing Technology* 79/1-3 (1998) 133.
- [8] H.G. Prengel, W.R. Pfouts, A.T. Santhanam, *Surface & Coatings Technology* 102 (1998) 183.
- [9] M. Adamik, P.B. Barna, *Surface & Coatings Technology* 80/1-2 (1996) 109.
- [10] M. Halvarsson, H. Norden, S. Vuorinen, *Surface & Coatings Technology* 68 (1994) 266.
- [11] H. Chien, M.C. Gao, H.M. Miller, G.S. Rohrer, Z. Ban, P. Prichard, Y. Liu, *International Journal of Refractory Metals & Hard Materials* 27 (2009) 458.
- [12] S. Ruppi, *Surface & Coatings Technology* 202/17 (2008) 4257.
- [13] S. Ruppi, *International Journal of Refractory Metals & Hard Materials* 23/4-6 (2005) 306.
- [14] J.G. Kim, C.S. Park, J.S. Chun, *Thin Solid Films* 97/1 (1982) 97.
- [15] W. Lengauer, K. Dreyer, *Journal of Alloys and Compounds* 338/1-2 (2002) 194.
- [16] Z.J. Liu, Z.K. Liu, C. McNerny, P. Mehrotra, A. Inspektor, *Surface & Coatings Technology* 198/1-3 (2005) 161.
- [17] W.C. Russell, K.R. Padmanabhan, *Surface & Coatings Technology* 68-69 (1994) 221.
- [18] J. Liao, J.C. Li, K.H. Kuo, *Metallurgical Transactions a-Physical Metallurgy and Materials Science* 20/2 (1989) 279.
- [19] J. Skogsmo, A. Henjered, H. Norden, *Journal De Physique* 45/Nc9 (1984) 447.
- [20] J. Skogsmo, H. Norden, *Ultramicroscopy* 24/1 (1988) 77.
- [21] J. Skogsmo, H. Norden, *International Journal of Refractory Metals & Hard Materials* 11/1 (1992) 49.
- [22] M. Klaus, C. Genzel, H. Holzschuh, *Thin Solid Films* 517/3 (2008) 1172.
- [23] H. Holzschuh, M. Klaus, C. Genzel, *Advances in Powder Metallurgy & Particulate Materials*, Washington D.C., 2008, p. 100.
- [24] H. Holzschuh, J. Drobniowski, Patent No. WO2009101025A1, 2009.
- [25] C. Barbatti, J. Garcia, R. Pitonak, H. Pinto, A. Kostka, A. Di Prinzio, M.H. Staia, A.R. Pyzalla, *Surface & Coatings Technology* 203/24 (2009) 3708.
- [26] H. Westphal, V. Sottke, Patent No. DE10123554, 2002.
- [27] K.L. Choy, *Progress in Materials Science* 45 (2003) 57.
- [28] F.W. Bach, K. Möhwald, T. Wenz, *Moderne Beschichtungsverfahren*, Wiley-VCH, 2005.
- [29] H.O. Pierson, *Handbook of Chemical Vapor Deposition*, Noyes Publications, New Jersey, 1999.
- [30] W. Schedler, *Hartmetall für den Praktiker*, Plansee TIZIT, Düsseldorf, 1988.
- [31] H. Czirchos, M. Hennecke, *Hütte - Das Ingenieurwesen*, Springer-Verlag Berlin, Heidelberg New York, 2004.
- [32] E. Mohn, R. Bonetti, H. Wiprachtiger, *Journal De Physique* 50/C-5 (1989) 811.
- [33] C. Czettl, C. Mitterer, C. Michotte, M. Penoy, M. Kathrein, in: L.S. Sigl, P. Rödhammer, H. Wildner (Eds.), 17<sup>th</sup> Int. Plansee Seminar, Plansee Group, Reutte, Austria, 2009, p. HM71.1
- [34] H. Fischmeister, H. Jehn, *Hartstoffe zur Verschleißminderung*, Deutsche Gesellschaft für Metallkunde e.V., Bad Honnef, 1987.

- [35] J.O. Carlsson, *Thin Solid Films* 130 (1985) 261.
- [36] D.J. Cheng, W.P. Sun, M.H. Hon, *Thin Solid Films* 146/1 (1987) 45.
- [37] J. Wagner, C. Mitterer, M. Penoy, C. Michotte, W. Wallgram, M. Kathrein, in: G. Kneringer, P. Rödhammer, H. Wildner (Eds.), 16<sup>th</sup> Int. Plansee Seminar, Reutte, 2005, p. 917.
- [38] J. Wagner, C. Mitterer, M. Penoy, C. Michotte, W. Wallgram, M. Kathrein, *International Journal of Refractory Metals & Hard Materials* 26/2 (2008) 120.
- [39] D.H. Kuo, K.W. Huang, *Surface & Coatings Technology* 135/2-3 (2001) 150.
- [40] H. Kashani, M.H. Sohi, H. Kaypour, *Materials Science and Engineering a-Structural Materials Properties Microstructure and Processing* 286/2 (2000) 324.
- [41] S. Rупpi, A. Larsson, *Journal of Vacuum Science & Technology A* 21/1 (2003) 66.
- [42] M. Kathrein, W. Schintlmeister, W. Wallgram, U. Schleinkofer, *Surface & Coatings Technology* 163 (2003) 181.
- [43] H. Holzschuh, *International Journal of Refractory Metals & Hard Materials* 20/2 (2002) 143.
- [44] S. Rупpi, A. Larsson, *Thin Solid Films* 388/1-2 (2001) 50.
- [45] S. Rупpi, A. Larsson, *Fifteenth International Symposium on Chemical Vapor Deposition, The Electrochemical Society Inc.*, 2000, p. 372.
- [46] S. Rупpi, A. Larsson, *Journal De Physique IV* 9/P8 (1999) 349.
- [47] D. Hochauer, C. Mitterer, M. Penoy, C. Michotte, H.P. Martinz, M. Kathrein, *Surface & Coatings Technology* 203/3-4 (2008) 350.
- [48] M. Danzinger, J. Peng, R. Haubner, B. Lux, *Journal De Physique II* 1/C2 (1991) 571.
- [49] M. Danzinger, R. Haubner, B. Lux, in: T.S. Sudarshan, D.G. Bhat (Eds.), *Surface modification technologies III, The Minerals, Metals & Material Society*, 1990, p. 829.
- [50] A. Osada, M. Danzinger, R. Haubner, B. Lux, *Journal De Physique II* 1/C2 (1991) 557.
- [51] TIZIT Goldmaster - Da ist sie die bahnbrechende Neuerung in der Zerspanungstechnik; Reutte, 1973
- [52] W. Schintlmeister, W. Wallgram, J. Kanz, *Thin Solid Films* 107/2 (1983) 117.
- [53] R. Funk, H. Schachner, C. Triquet, M. Kornmann, B. Lux, *Journal of the Electrochemical Society* 123/2 (1976) 285.
- [54] M. Kornmann, H. Schachner, R. Funk, B. Lux, *Journal of Crystal Growth* 28/2 (1975) 259.
- [55] B. Ljungberg, M. Sjostrand, J. Lindström, Patent No. US005674564A, 1997.
- [56] A.A. Layyous, D.M. Freinkel, R. Israel, *Surface & Coatings Technology* 56/1 (1992) 89.
- [57] U.K.H. Smith, J.N. Lindstrom, H. Mantle, Patent No. US4180400, 1979.
- [58] M. Halvarsson, S. Vuorinen, *Surface & Coatings Technology* 76/1-3 (1995) 287.
- [59] M. Halvarsson, S. Vuorinen, *International Journal of Refractory Metals & Hard Materials* 15/1-3 (1997) 169.
- [60] H. Holzschuh, Patent No. EP1113092B1, 2000.
- [61] A. Osada, E. Nakamura, H. Homma, T. Hayahi, T. Oshika, *International Journal of Refractory Metals & Hard Materials* 24/5 (2006) 387.
- [62] A. Larsson, M. Halvarsson, S. Rупpi, *Surface & Coatings Technology* 111/2-3 (1999) 191.
- [63] S. Rупpi, M. Halvarsson, *Thin Solid Films* 353/1-2 (1999) 182.
- [64] J. Skogsmo, M. Halvarsson, S. Vuorinen, *Surface & Coatings Technology* 54/1-3 (1992) 186.
- [65] S. Vuorinen, L. Karlsson, *Thin Solid Films* 214/2 (1992) 132.
- [66] N. Lindulf, M. Halvarsson, H. Norden, S. Vuorinen, *Thin Solid Films* 253/1-2 (1994) 311.
- [67] P. Hansson, M. Halvarsson, S. Vuorinen, *Surface & Coatings Technology* 76/1-3 (1995) 256.
- [68] A. Larsson, M. Halvarsson, S. Vuorinen, *International Journal of Refractory Metals & Hard Materials* 16/4-6 (1998) 369.

- [69] D. Hochauer, C. Mitterer, M. Penoy, C. Michotte, H.P. Martinz, M. Kathrein, *Surface & Coatings Technology* 204/21-22 (2010) 3713.
- [70] M. Okude, K. Tomita, K. Yamaguchi, A. Osada, in: H.S. Kestler, L. S. (Ed.), 18<sup>th</sup> Int. Plansee Seminar, Kestler, H. & Sigl, L., Reutte, 2013.
- [71] C. Chatfield, J.N. Lindstrom, M.E. Sjostrand, *Journal De Physique* 50/C-5 (1989) 377.
- [72] A. Larsson, M. Halvarsson, S. Vuorinen, *Surface & Coatings Technology* 94-5/1-3 (1997) 76.
- [73] S. Rупpi, Patent No. US5700569, 1997.
- [74] S. Rупpi, Patent No. US5635247, 1997.
- [75] M. Fallqvist, M. Olsson, S. Rупpi, *Wear* 263/1-6 (2007) 74.
- [76] M. Halvarsson, S. Vuorinen, *Materials Science and Engineering* 209/1-2 (1996) 337.
- [77] M. Halvarsson, S. Vuorinen, *Surface & Coatings Technology* 80/1-2 (1996) 80.
- [78] M. Halvarsson, H. Norden, S. Vuorinen, *Surface & Coatings Technology* 61/1-3 (1993) 177.
- [79] S. Vuorinen, J. Skogsmo, *Thin Solid Films* 193/1-2 (1990) 536.
- [80] M. Halvarsson, J.E. Trancik, S. Rупpi, *International Journal of Refractory Metals & Hard Materials* 24/1-2 (2006) 32.
- [81] C. Czettl, C. Mitterer, M. Penoy, C. Michotte, M. Kathrein, in: H. Teuber (Ed.), SMT24, Fraunhofer Institute for Material and Beam Technology IWS Dresden, Dresden, 2010.
- [82] B. Ljungberg, A. Lenander, Patent No. US5487625, 1996.
- [83] B. Ljungberg, A. Lenander, Patent No. US5654035, 1997.
- [84] B. Ljungberg, Patent No. US5766782, 1998.
- [85] B. Ljungberg, Patent No. US5851687, 1998.
- [86] C. Wüstefeld, C. Czettl, unpublished work, 2010.
- [87] A. Schweißgut, CERATIZIT CT-Lab 4067 - Walter WAK20, WNMG 080416-NM4, 19-7-2001.
- [88] L. Spieß, R. Schwarzer, H. Behnken, G. Teichert, *Moderne Röntgenbeugung*, B. G. Teubner Verlag / GWV Fachverlage GmbH, Wiesbaden, 2005.
- [89] G.B. Harris, *Philosophical Magazine* 43/336 (1952) 113.
- [90] M.H. Müller, W.P. Chernock, P.A. Beck, *Transactions of The Metallurgical Society of AIME* 212 (1958) 39.
- [91] B. Ljungberg, A. Lenander, Patent No. EP0603144B1, 1993.
- [92] P. Martensson, Patent No. US20040202877A1, 2004.
- [93] E. Sundström, S. Ostlund, J. Zackrisson, Patent No. WO2008094104A1, 2008.
- [94] S. Rупpi, Patent No. EP1953258B1, 2011.
- [95] M. Birkholz, *Thin Film Analysis by X-Ray Scattering*, Wiley-VCH Verlag, Weinheim, 2006.
- [96] V.K. Sarin, J.N. Lindstrom, *Journal of the Electrochemical Society* 126/7 (1979) 1281.
- [97] E. Breval, S. Vuorinen, *Materials Science and Engineering* 42/1-2 (1980) 361.
- [98] C.W. Lee, J.S. Chun, in: J.M. Blocher, G.E. Vuillard, G. Wahl (Eds.), 8<sup>th</sup> Int. Conf. on Chemical Vapor Deposition, The Electrochemical Society, Inc., 1981, p. 554.
- [99] M. Bonetti-Lang, R. Bonetti, H.E. Hintermann, in: J.M. Blocher, G.E. Vuillard, G. Wahl (Eds.), 8<sup>th</sup> Int. Conf. on Chemical Vapor Deposition, The Electrochemical Society, Inc., 1981, p. 606.
- [100] A. Larsson, S. Rупpi, *Thin Solid Films* 402/1-2 (2002) 203.
- [101] L. Schmid, CERATIZIT CT-Lab 259 - Sandvik GC425, CNMG120408, 2-12-1987.
- [102] S. Vuorinen, R.H. Hoel, *Thin Solid Films* 232/1 (1993) 73.
- [103] E. Kübel, *Surface & Coatings Technology* 49/1-3 (1991) 268.
- [104] E. Kubel, *European Machining* 4/Juli/August (1992) 1.
- [105] E. Kübel, *Metal Powder Report/Dez 1988* (1988) 832.
- [106] E. Kübel, *VDI Berichte Nr. 670* (1988) 625.

- [107] E. Kubel, Metal Powder Report 47/10 (1992) 50.
- [108] H. Holzschuh, in: G. Kneringer, P. Rödhammer, H. Wildner (Eds.), 15<sup>th</sup> Int. Plansee Seminar, Plansee Holding AG, Reutte, 2001, p. 441.
- [109] C. Czettl, C. Mitterer, U. Mühle, D. Rafaja, S. Puchner, H. Hutter, M. Penoy, C. Michotte, M. Kathrein, Surface & Coatings Technology 206/7 (2011) 1691.
- [110] J. Wanatabe, Y. Sone, Patent No. EP1897970A1, 2008.
- [111] H. Holzschuh, in: G. Kneringer, P. Rödhammer, H. Wildner (Eds.), 16<sup>th</sup> Int. Plansee Seminar, Plansee Holding AG, Reutte, 2005, p. HM59.
- [112] H. Holzschuh, Thin Solid Films 469-70 (2004) 92.
- [113] C. Czettl, C. Mitterer, M. Penoy, C. Michotte, M. Kathrein, Surface & Coatings Technology 215/0 (2013) 127.
- [114] K. Hiroyuki, Patent No. EP1138800A1, 2001.
- [115] I. Endler, M. Hohn, M. Herrmann, R. Pitonak, S. Ruppi, M. Schneider, H. van den Berg, H. Westphal, Surface & Coatings Technology 203/5-7 (2008) 530.
- [116] P. Martensson, Surface & Coatings Technology 200 (2006) 3626.
- [117] M. Fallqvist, M. Olsson, S. Ruppi, Surface & Coatings Technology 202/4-7 (2007) 837.
- [118] S. Ruppi, A. Larsson, A. Flink, Thin Solid Films 516/18 (2008) 5959.
- [119] W. Vötsch, J. Drobniowski, Germany, Patent No. EP1193328A1, 2001.
- [120] W. Wallgram, U. Schleinkofer, K. Gigl, J. Thurner, W. Schintlmeister, Patent No. WO2006058353A1, 2006.
- [121] A. Riedl, N. Schalk, C. Czettl, B. Satory, C. Mitterer, Wear 289 (2012) 9.
- [122] H. Van den Berg, H. Westphal, M.D. Schneeweiß, S. Köhler, J. Glühmann, U. Gieland, Werkstatt und Betrieb 12 (2005) 50.
- [123] L. Spieß, H. Westphal, M. Tümmler, D. Schmidt, M. Wilke, T. Kups, in: L. Spieß, E. Rädlein, P. Schaaf (Eds.), Thüringer Werkstofftag 2010, Universitätsverlag Ilmenau, Ilmenau, 2010, p. 127.
- [124] K.D. Bouzakis, F. Klocke, G. Skordaris, E. Bouzakis, S. Gerardis, G. Katirtzoglou, S. Makrimallakis, Wear 271/5-6 (2011) 783.
- [125] K.D. Bouzakis, G. Skordaris, I. Mirisidis, N. Michailidis, G. Mesomeris, E. Pavlidou, G. Erkens, Surface & Coatings Technology 200/5-6 (2005) 1879.
- [126] K.D. Bouzakis, G. Skordaris, E. Bouzakis, A. Tsouknidas, S. Makrimallakis, S. Gerardis, G. Katirtzoglou, CIRP Annals - Manufacturing Technology 60/1 (2011) 587.
- [127] M. Arndt, H. Westphal, in: K.-D. Bouzakis, F.-W. Bach, B. Denckema, M. Geiger (Eds.), 7<sup>th</sup> Int. Conf. of Coatings in Manufacturing Engineering, Chalkidiki, Greece, 2008.
- [128] A. Schweißgut, CERATIZIT CT-Lab 5222 - Walter WAK10, CNMA 120408, 12-7-2006.
- [129] A. Schweißgut, CERATIZIT CT-Lab 12522 - Walter WAK20, CNMA 120408, 19-11-2010.
- [130] A. Schweißgut, CERATIZIT CT-Lab 5172 - Sandvik GC3205, CNMA 120408KR, 12-7-2006.
- [131] A. Schweißgut, CERATIZIT CT-Lab 5208 - Seco TK1000, CNMA 120408, 12-7-2006.
- [132] A. Schweißgut, CERATIZIT CT-Lab 5182 - Mitsubishi UC5115, CNMA 120408, 12-7-2006.
- [133] A. Schweißgut, CERATIZIT CT-Lab 5177 - Kennametal KC9315, CNMA 120408, 12-7-2006.
- [134] A. Schweißgut, CERATIZIT CT-Lab 5171 - Sandvik GC3015, CNMA 120408KR, 12-7-2006.
- [135] N. Schalk, PhD, Department of Functional Materials and Material Systems, Montanuniversität Leoben, Leoben, 2013.
- [136] K. Schiffner, C. Droste gen. Helling, Computers & Structures 72/1-3 (1999) 329.
- [137] B. Scholtes, Eigenspannungen in mechanisch randschichtverformten Werkstoffzuständen, DGM Informationsgesellschaft, Karlsruhe, 1990.



- [138] M. Klaus, Dr.-Ing. PhD Thesis, von der Fakultät III - Prozesswissenschaften der Technischen Universität Berlin, TU Berlin, Berlin, 2009.
- [139] J. Keckes, M. Bartosik, R. Daniel, C. Mitterer, G. Maier, W. Ecker, J. Vila-Comamala, C. David, S. Schoeder, M. Burghammer, *Scripta Materialia* 67/9 (2012) 748.
- [140] W. Wallgram, U. Schleinkofer, in: L.S. Sigl, P. Rödhammer, H. Wildner (Eds.), 17<sup>th</sup> Int. Plansee Seminar, Plansee Group, Reutte, Austria, 2009, p. HM32.
- [141] A. Paseuth, S. Okuno, H. Kanaoka, E. Iwai, T. Ichikawa, Patent No. WO2013128673, 2013.
- [142] I. Endler, M. Höhn, M. Herrmann, H. Holzschuh, R. Pitonak, S. Ruppi, H.v. den Berg, H. Westphal, L. Wilde, *Surface & Coatings Technology* 205/5 (2010) 1307.
- [143] I. Endler, Patent No. WO2007003648A1, 2007.
- [144] I. Endler, Patent No. WO2009050110A2, 2009.
- [145] EMUGE-Franken, *Handbuch der Gewindetechnik und Frästechnik* EMUGE-Franken, Erlangen, 2004.
- [146] M. Van Stappen, L.M. Stals, M. Kerkhofs, C. Quaeys, *Surface & Coatings Technology* 74–75, Part 2/0 (1995) 629.
- [147] B. Denkena, B. Breidenstein, L. Wagner, M. Wollmann, M. Mhaede, *International Journal of Refractory Metals & Hard Materials* 36/0 (2013) 85.
- [148] K.D. Bouzakis, E. Bouzakis, G. Skordaris, S. Makrimalakis, A. Tsouknidas, G. Katirtzoglou, S. Gerardis, *Surface & Coatings Technology* 205, Supplement 2/0 (2011) S128.
- [149] J. Keckes, R. Daniel, C. Mitterer, I. Matko, B. Sartory, A. Koepf, R. Weißenbacher, R. Pitonak, *Thin Solid Films* 545/0 (2013) 29.
- [150] Y.J. Liu, H.J. Kim, Y. Egashira, H. Kimura, H. Komiyama, *Journal of the American Ceramic Society* 79/5 (1996) 1335.
- [151] A. Anderbouhr, E. Blanquet, V. Ghetta, C. Bernard, in: M.D. Allendorf, C. Bernard (Eds.), *EUROCVI 14*, The Electrochemical Society, Inc., 1997, p. 356.
- [152] R. Madar, A. Rouault, E. Blanquet, A.M. Doutron, Patent No. US6238739B1, 2001.
- [153] R. Pitonak, R. Weissenbacher, A. Köpf, Patent No. AT510963B1, 2012.
- [154] R. Pitonak, R. Weissenbacher, A. Köpf, Patent No. AT510713B1, 2012.
- [155] S. Anderbouhr, V. Ghetta, E. Blanquet, C. Chabrol, F. Schuster, C. Bernard, R. Madar, *Surface & Coatings Technology* 115/2-3 (1999) 103.
- [156] N. Yoshikawa, M. Aoki, A. Kikuchi, S. Taniguchi, *International Journal of Materials and Product Technology* 16/1/2/3 (2001) 109.
- [157] J. Wagner, V. Edlmayr, M. Penoy, C. Michotte, C. Mitterer, M. Kathrein, *International Journal of Refractory Metals & Hard Materials* 26/6 (2008) 563.
- [158] N. Ramanuja, R.A. Levy, S.N. Dharmadhikari, E. Ramos, C.W. Pearce, S.C. Menasian, P.C. Schamberger, C.C. Collins, *Materials Letters* 57/2 (2002) 261.
- [159] W.-Y. Uen, Z.-Y. Li, S.-M. Lan, T.-N. Yang, S.-M. Liao, *Thin Solid Films* 516/1 (2007) 99.
- [160] The Cutting Grade of the Future: 639D/E-gültig ab valid since 09/2011; 2011
- [161] Fraunhofer-Alliance AdvanCer, 2012.
- [162] H. Röhr, MAV Innovationsforum 2011, 2011, p. 39.
- [163] C. Wüstefeld, D. Rafaja, M. Dopita, M. Motylenko, C. Baetz, C. Michotte, M. Kathrein, *Surface & Coatings Technology* 206/7 (2011) 1727.
- [164] Q. Xia, H. Xia, A.J. Ruoff, *Journal of Applied Physics* 73 (1993) 8198.
- [165] H. Van den Berg, H. Westphal, V. Sottke, Patent No. WO2009112115A1, 2009.
- [166] H. Van den Berg, H. Westphal, V. Sottke, Patent No. WO2009112116A1, 2009.
- [167] S. Cho, H.S. Kim, D.Y. Lee, D.S. Han, Y.H. Seo, S.Y. Ahn, D.B. Park, Patent No. DE112011101379T5, 2013.

## 6 Publications

### 6.1 List of included Publications

- I. Homogeneity of industrial scale thermal CVD processes for TiCN hard coatings  
C. Czettl, C. Mitterer, C. Michotte, M. Penoy, M. Kathrein,  
in: L.S. Sigl, P. Rödhammer, H. Wildner (Eds.),  
17<sup>th</sup> International Plansee Seminar, Reutte, Austria, 2009, p. HM71.1
- II. Stress state of CVD TiCN/ $\kappa$ -Al<sub>2</sub>O<sub>3</sub> hard coatings  
C. Czettl, C. Mitterer, M. Penoy, C. Michotte, M. Kathrein, in:  
H. Teuber (Ed.), SMT24, Fraunhofer Institute for Material and Beam Technology  
IWS, Dresden, 2010.
- III. CO addition in low-pressure chemical vapor deposition of medium-temperature  
TiC<sub>x</sub>N<sub>1-x</sub> based hard coatings  
C. Czettl, C. Mitterer, U. Mühle, D. Rafaja, S. Puchner, H. Hutter, M. Penoy, C.  
Michotte, M. Kathrein,  
Surface & Coatings Technology 206/7 (2011) 1691.
- IV. C<sub>2</sub>H<sub>6</sub> as precursor for low pressure chemical vapor deposition of TiCNB hard  
coatings  
C. Czettl, C. Mitterer, M. Penoy, C. Michotte, M. Kathrein,  
Surface & Coatings Technology 215/0 (2013) 127.

## 6.2 Publications related to this work

- V. Tribological properties of Al<sub>2</sub>O<sub>3</sub> hard coatings modified by mechanical blasting and polishing post-treatment  
A. Riedl, N. Schalk, C. Czettl, B. Sartory, C. Mitterer,  
Wear 289 (2012) 9.
- VI. Friction reduction by thermal treatment of arc evaporated TiAlTaN coatings in methane  
N. Schalk, C. Mitterer, I. Letofsky-Papst, C. Czettl, B. Sartory,  
M. Penoy, C. Michotte,  
Tribology International 67/0 (2013) 54.
- VII. Spatial correlation of tensile residual stress and thermal fatigue damage in coated cemented carbide milling inserts  
T. Tepperneegg, T. Klünsner, C. Tritremmel, C. Czettl, J. Keckes,  
T. Wroblewski, R. Ebner, R. Pippan, in: H. Kestler (Ed.),  
18<sup>th</sup> International Plansee Seminar, Reutte, 2013.
- VIII. Industrial-scale sputter deposition of Cr<sub>1-x</sub>Al<sub>x</sub>N coatings with  $0.21 \leq x \leq 0.74$  from segmented targets  
T. Weirather, C. Czettl, P. Polcik, M. Kathrein, C. Mitterer,  
Surface & Coatings Technology 232/0 (2013) 303.
- IX. Microstructure of TiAlN / AlTiRuN multilayers grown by cathodic arc evaporation  
C. Wüstefeld, M. Motylenko, D. Rafaja, D. Heger, C. Michotte,  
C. Czettl, M. Kathrein, in: H. Kestler (Ed.),  
18<sup>th</sup> International Plansee Seminar, Reutte, 2013.
- X. Dry-blasting of  $\alpha$ - and  $\kappa$ -Al<sub>2</sub>O<sub>3</sub> CVD hard coatings: Friction behaviour and thermal stress relaxation  
N. Schalk, C. Mitterer, C. Czettl, B. Sartory, M. Penoy, C. Michotte, Tribology Letters 52/1 (2013) 147.
- XI. The effect of droplets in arc evaporated TiAlTaN hard coatings on the wear behavior  
M. Tkadletz, C. Mitterer, B. Sartory, I. Letofsky-Papst, C. Czettl,  
C. Michotte  
Submitted to Surface & Coatings Technology
- XII. Nanoindentation of CVD Al<sub>2</sub>O<sub>3</sub> hard coatings at elevated temperatures  
M. Rebelo de Figueiredo, M.D. Abad, A.J. Harris, C. Czettl, C. Mitterer,  
P. Hosemann  
Submitted to Philosophical Magazine
- XIII. Applications - Coating applications to cutting tools  
U. Schleinkofer, C. Czettl, C. Michotte:  
Applications - Coating applications to cutting tools,  
in V. Sarin (ed), Comprehensive Hard Materials, in press.
- XIV. Schneidwerkzeug zur Bearbeitung metallischer Werkstoffe  
M. Kathrein, C. Czettl, W. Bürgin, J. Thurner, P. Lechleitner  
Patent No. AT12293U1, 2012.

- XV. Verfahren zur Herstellung einer Hartstoffschicht auf einem Substrat,  
Hartstoffschicht sowie Zerspanwerkzeug  
C. Czettl  
Patent No. AT13091U1, 2013.

## **6.3 My contribution to the included Publications**

### **Publication I**

Within this publication, my contribution was the design of the concept of the investigations as well as preparation and selection of the specimens. The requirement was that this sample arrangement could be used in all further publications, with same nomenclature in any available CVD device. Also the preparation of coating recipes, adaption of graphite parts for changed gas flow, and batching was done by myself, with technical assistance by Karl Gigl. Light optical microscopy, gravimetric measurements, scanning electron microscopy, thermodynamic calculations, nanoindentation experiments and preparation of the measured data was done by myself. I also evaluated the XRD measurements and stress analysis, conducted by Marianne Penoy, calculated texture coefficients and wrote the manuscript.

### **Publication II**

Also for this manuscript, the concept, preparation of samples, creation of coating recipes and realization of the deposition runs was done by myself. I have also investigated the samples by SEM and LOM, nanoindentation, and gravimetric analysis. Similar to the other publications, I evaluated the XRD data provided by Marianne Penoy. The cutting tests were performed in the Ceratizit tooling academy under my supervision. The worn cutting inserts were investigated and evaluated by myself and I prepared the major part of the manuscript.

### **Publication III**

The design of the concept, preparation of the samples, development of the coating process and batching according to Publication I was done by myself. I have conducted the gravimetric measurements, coating thickness and roughness measurements, nanoindentation, as well as the SEM analysis. The ToF-SIMS data, measured by Stefan Puchner, as well as XRD and GDOES analysis performed by Marianne Penoy, were evaluated and interpreted by myself. The TEM analysis, performed by Uwe Mühle, was included in the manuscript with his support. The manuscript was prepared by myself.

### **Publication IV**

Also for the last publication, the concept of the manuscript was developed by myself. I also prepared all samples, defined the coating recipes, the batching and the execution of the deposition runs. Gravimetric measurements, determination of coating thickness, nanoindentation, SEM analysis and roughness measurements were conducted by myself. I have processed data from GDOES and XRD measurements, performed by Marianne Penoy. The interpretation and

incorporation of TEM analysis as well as results from cutting tests performed at the Ceratizit tooling academy were done by myself. I also prepared the manuscript with the conditioned data.

### Summary

The proportion of my contribution in percent is summarized in the table below.

	Concept and planning [%]	Experiments [%]	Analysis and interpretation [%]	Manuscript preparation [%]
Publication I	100	100	100	100
Publication II	100	100	85	95
Publication III	100	100	95	100
Publication IV	100	100	95	100

Supervision is not included!

## **Publication I**

### **Homogeneity of industrial scale thermal CVD process for TiCN hard coatings**

C. Czettl, C. Mitterer, C. Michotte, M. Penoy, M. Kathrein

17<sup>th</sup> International Plansee Seminar 2009, Reutte, Austria, 2009, p. HM71.1

# Homogeneity of Industrial Scale Thermal CVD Process for TiCN Hard Coatings

C. Czettl\*, C. Mitterer\*\*, C. Michotte\*\*\*, M. Penoy\*\*\*,  
M. Kathrein\*\*\*\*

\* Materials Center Leoben Forschung GmbH Leoben, Austria

\*\* Department of Physical Metallurgy and Materials Testing, University of Leoben, Austria

\*\*\* CERATIZIT Luxembourg GmbH, Mamer, Luxembourg

\*\*\*\* CERATIZIT Austria GmbH, Reutte, Austria

## Abstract

Different gas flow setups were investigated in an industrial scale thermal CVD hot wall reactor. Features of TiCN hard coatings deposited on cemented carbides are analysed with regard to homogeneity of coating thickness and composition in a production batch. The experiments were carried out in the  $\text{TiCl}_4/\text{CH}_4/\text{N}_2/\text{H}_2/\text{Ar}$  gas system at constant temperature of 1020 °C using cemented carbide inserts. The influence of the reactor geometry and gas flow conditions on the deposited coatings were analysed by gravimetric measurements, light optical microscopy, scanning electron microscopy and X-ray diffraction and related to the sample position on the respective level and radius of the substrate holder.

In this study, different reactor setups were compared and the achieved thickness, chemical composition, surface topography, preferred orientation and internal stresses in axial or radial direction are shown. The variation of obtained coating features as well as their order of magnitude are discussed which leads to the beneficial reactor geometry for the coating of a whole batch of inserts keeping the scattering at a minimum level.

## Keywords

CVD, TiCN, hard coating, homogeneity, gas flow setup



## Introduction

High temperature chemical vapor deposition (HT-CVD) is still the most cost effective process for coating of cemented carbide cutting tools. Batches of up to 20.000 half inch inserts can be coated within one deposition run, to produce hard coatings of carbides, nitrides, carbonitrides, borides and oxides in different multilayer architectures with a total thickness of up to 30  $\mu\text{m}$  [1-3]. A uniform deposition of each coating layer as well as the homogeneous coating distribution in industrial scale CVD units were the focus of many papers published in the last decades, with the goal to minimise tolerances and to increase productivity [4-6]. The most common coating design for turning and milling of iron based materials starts with a titanium nitride layer (TiN), followed by a medium temperature titanium carbonitride layer (MT-TiCN), a bond layer based on high temperature titanium carbonitrides (HT-TiCN) or TiN, an aluminium oxide ( $\text{Al}_2\text{O}_3$ ) layer and frequently a top layer of TiCN and/or TiN [7]. The top layer is commonly removed on the cutting edge or on the complete rake face by post treatment processes to smoothen the surface, to modify the stress gradient within the underlying  $\text{Al}_2\text{O}_3$  layer and, thus, to prevent micro-chipping [8].

The HT process for the production of TiCN base layers with  $\text{TiCl}_4$ ,  $\text{N}_2$  and  $\text{CH}_4$  as precursors has almost completely been displaced by the MT-TiCN process using  $\text{TiCl}_4$  and  $\text{CH}_3\text{CN}$ , which prevents in combination with the first TiN layer the undesired  $\eta$ -phase formation [9]. However, HT-TiCN is still applied within the bond layer and the top layer of the coatings [10]. In case of the bond layer, not only the variation of thickness over the whole batch is important, but the homogeneity of structure is crucial for the following deposition steps, in particular for the nucleation of  $\text{Al}_2\text{O}_3$ . A uniform structure is also crucial for the top layer, regarding the uniformity of surface roughness, internal stresses and color.

Thus, the aim of this work was to investigate the homogeneity of mass gain and coating thickness, structure, chemical composition and internal stresses of TiCN coatings deposited in a HT-CVD process using three different gas flow setups.

## Experimental Details

TiCN depositions were carried out using a computer controlled industrial scale hot wall CVD unit. The homogeneity of mass gain, structure, composition and internal stresses were investigated, using three different deposition systems, shown schematically in Fig. 1 and labeled as setup A, B and C. The associated gas preheating systems differ in contact surface and residence time of the feed gas, which is due to continuous evolution of the gas flow setups from A to B and finally C. The inlet gas composition was 5.9 vol.%  $\text{CH}_4$ , 3 vol.%  $\text{TiCl}_4$ , 64.8 vol.%  $\text{H}_2$ , 7.5 vol.%  $\text{N}_2$  and 18.8 vol.% Ar at a constant deposition temperature of 1020  $^\circ\text{C}$ . The deposition time for each experiment was 90 minutes and the total gas flow was adjusted in relation to the reactor volume. The used specimens were commercial 11 wt.-% Co cemented carbide inserts in SNUN 120412 geometry

with a polished surface. To achieve a representative overview of the whole batch, specimens were positioned on levels in the top, middle and bottom region of the reactor. On each level, specimens were placed in the center, on the half radius and at close to the outside border of the sample holder, named  $R_0$ ,  $R_{1/2}$  and  $R$ , respectively.

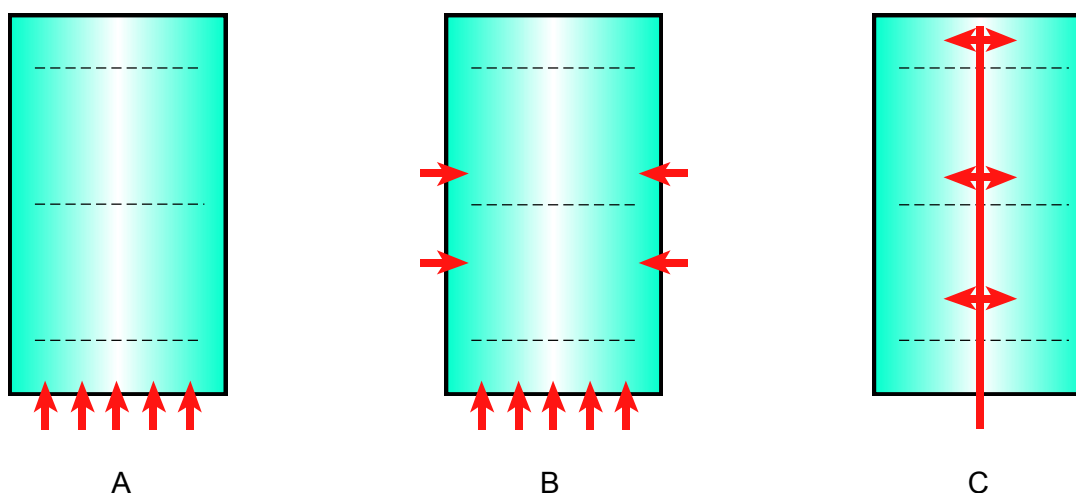


Fig. 1: Schematics of the gas flow setups used in the different deposition systems

Thermodynamics of TiN and TiCN formation was assessed using the software package HSC Chemistry [11]. The mass gain was determined using a Sartorius micro-balance with 0.1 mg accuracy. The coating thickness was measured on polished cross sections using a Nikon Epiphot 300 light optical microscope (LOM) with Image Access measurement software. The crystallographic structure of the deposited layer was determined using a Panalytical X'Pert Pro X-ray diffraction (XRD) unit with Cu  $K\alpha$  radiation and glancing angle (angle of incidence,  $2^\circ$ ) geometry. The C/(C+N) atomic ratio was determined by XRD via the stress corrected lattice parameter regarding to Vegard's law [12], as proven for many solid solutions of  $TiC_xN_{1-x}$  compositions [13-15]. The residual stresses of the coatings were studied by the  $\sin^2\Psi$  method. Surface topography was investigated using a FEI Quanta 200 scanning electron microscope (SEM).

## Results and Discussion

### Mass gain and layer thickness

The mean mass gain of the nine analysed samples per batch was  $16.6 \pm 1.3$  mg,  $9.4 \pm 1.7$  mg and  $8.9 \pm 2.2$  mg for the gas flow systems A, B and C, respectively. The highest mass gain was observed using gas flow setup A, where it was about 70 % higher than for B and C. This can be caused by a overproportional amount of feed gas and higher supersaturation [16]. The scattering of mass gain for the individual sample positions within each experiment is the lowest for setup A.

For the arrangements B and C, a slight decrease of mass gain towards the outside specimen at the top level can be seen, as illustrated in Fig. 2.

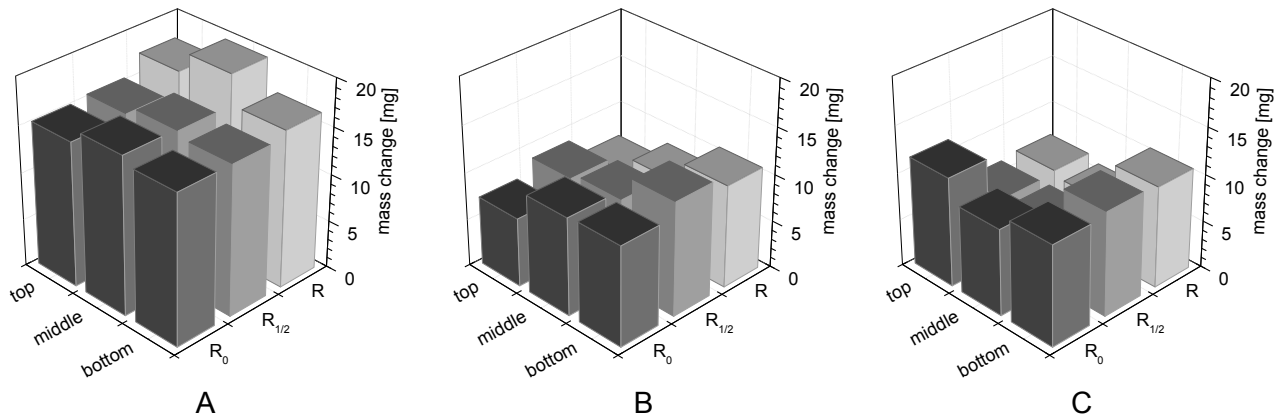


Fig. 2: Mass gain distribution in relation to gas flow setup and specimen position

The mean growth rate of  $32.0$ ,  $18.2$  and  $8.9 \text{ g cm}^{-2} \text{ min}^{-1}$  for the gas flow systems A, B and C, respectively, are higher than the values of  $2\text{-}6 \text{ g cm}^{-2} \text{ min}^{-1}$  reported by Cheng et al. [16]. This is due to the higher total gas flow rates used in our experiments, where the deposition temperature is close to the transition point from surface limited reaction to mass flow controlled reaction [17].

The average standard deviation of mass gain was calculated for each level and each radial position to assess the volume distribution for the three different setups. The obtained values are  $0.6$ ,  $1.9$  and  $2.1$  along the height of the reactor and  $0.6$ ,  $0.9$  and  $1.5$  in radial direction for the gas flow systems A, B and C, respectively. This denotes that the homogeneity of mass gain within one level is better than along the height of the reactor, especially for gas flow systems B and C.

The measured layer thickness distribution is shown in Fig. 3, which correlates well with the mass gain presented in Fig. 2, except for the specimen on the middle level, position R, in setup A. The higher mass gain of gas flow setup A results in an increased average layer thickness for the nine samples of  $5.9 \pm 0.2 \text{ }\mu\text{m}$ , compared to  $3.4 \pm 0.3 \text{ }\mu\text{m}$  and  $2.9 \pm 0.3 \text{ }\mu\text{m}$  for gas flow setup B and C, respectively.

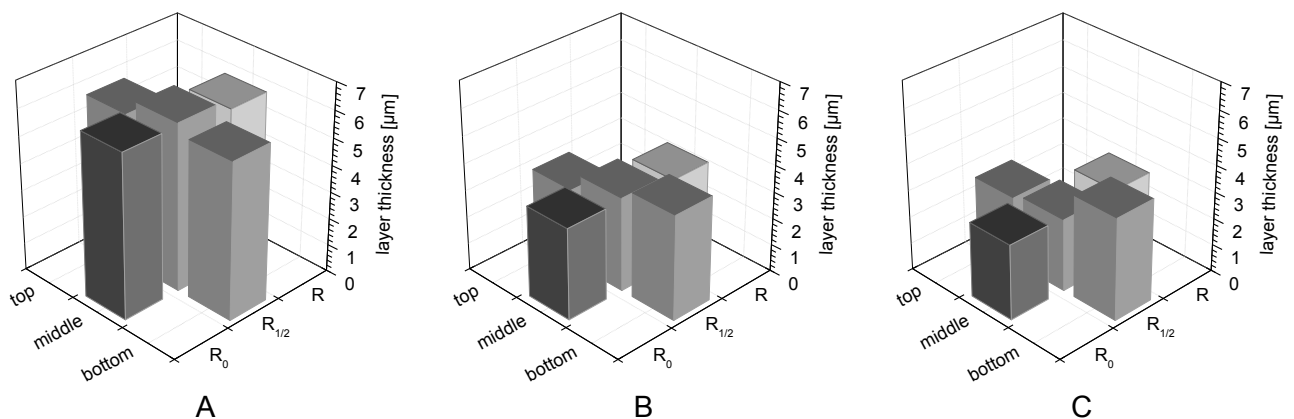


Fig. 3: Layer thickness distribution in relation to gas flow setup and specimen position

## Chemical composition

The mean C/(C+N) atomic ratio of five selected samples was  $0.45 \pm 0.05$ ,  $0.64 \pm 0.02$  and  $0.74 \pm 0.03$ , for the gas flow systems A, B and C, respectively (see Fig. 4). This is in a good agreement with earlier experiments conducted in setup B, where a C/(C+N) ratio of 0.62 has been reported for a comparable feed gas composition [18].

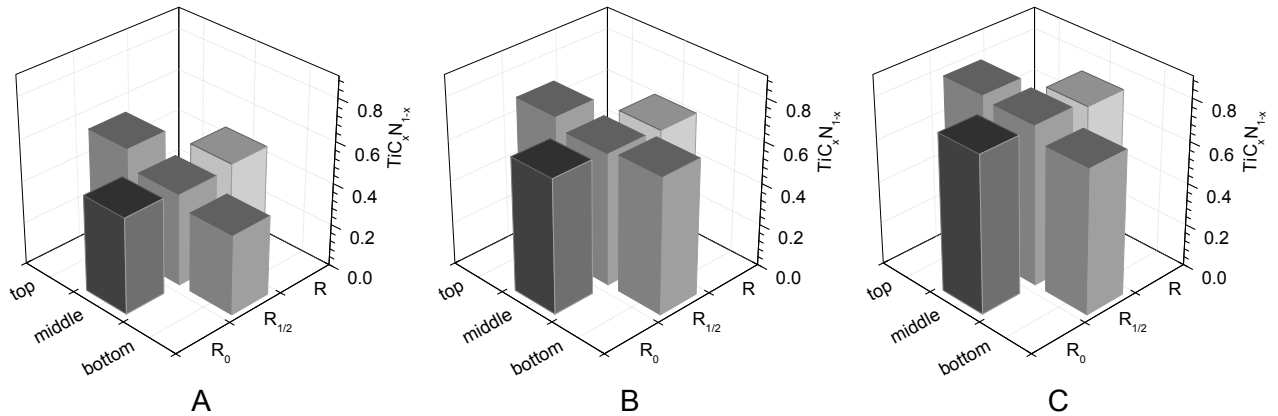


Fig. 4: TiCN composition in relation to gas flow setup and specimen position

From the thermodynamics point of view, the formation of TiN is more favorable at lower temperatures, as can be seen in Fig. 5. Thus, for setup A, the lower C/(C+N) atomic ratio shown in Fig. 5 indicates that the pre-heating of the feed gas is inadequate, i.e. the chemical reactivity of CH<sub>4</sub> decreases with decreasing temperatures, which causes the shift to lower C/(C+N) ratios of the deposited layers.

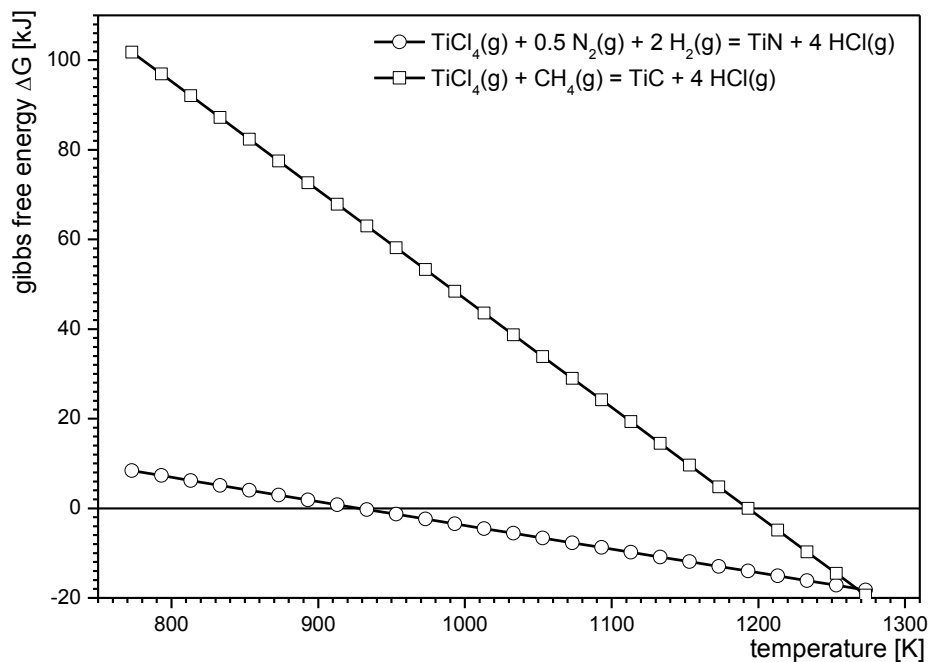


Fig. 5: Thermodynamical calculation of the Gibbs free energy of TiN and TiC formation.

The scattering of the C/(C+N) ratio within one level is low, as illustrated in Fig. 4. Considering the composition along the height of the reactor, a pronounced increase of the C/(C+N) ratio for gas flow setup A and a slight increase for gas flow setup C can be seen. Only gas flow setup B yields a quite homogenous profile, which can be explained by the additional gas inlets (see Fig. 1).

### Stress and Preferred Orientation

All coatings show peaks of the face-centered cubic TiCN solid solution in the XRD patterns. The internal coating stress of the five analysed samples shown in Fig. 6 was  $380 \pm 215$ ,  $441 \pm 60$  and  $559 \pm 22$  MPa for the gas flow setups A, B and C, respectively. There are pronounced differences of the internal stress regarding to the specimen positions in gas flow setup A, whereas the stresses in setup B are more uniform and in C nearly constant over all investigated positions. This can be correlated with the evenly distributed gas supply and the short gas pathways.

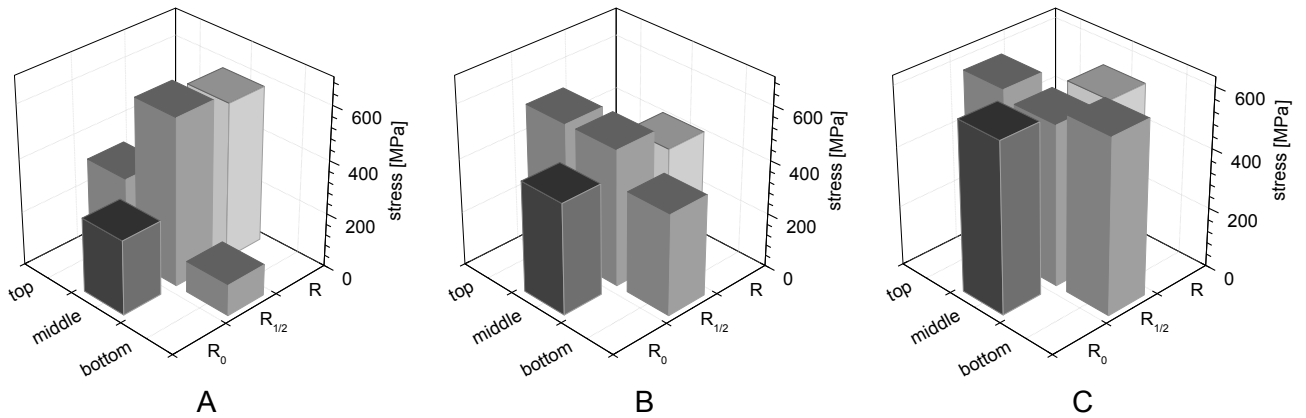


Fig. 6: Internal coating stresses in relation to gas flow setup and specimen position

The preferred orientation of the deposited layer is described with the texture coefficient  $TC_{(hkl)}$  according to Harris [19].  $TC_{(hkl)}$  is calculated as shown in equation 1, using the measured peak intensity  $I_{(hkl)}$  in relation to the standard peak intensity  $I_{0,(hkl)}$  from the JCPDS file # 00-042-1489 and the number of peaks considered  $n$ .

$$TC_{(hkl)} = \frac{I_{(hkl)} / I_{0,(hkl)}}{1/n \sum I_{(hkl)} / I_{0,(hkl)}} \quad (1)$$


A uniform preferred orientation can be seen at the middle level for gas flow setup A, B and C (see Table I). Only the specimens on the bottom level differ significantly from the positions located higher. The samples grown with gas flow setup A show a pronounced (222) and (311) orientation, with increasing TC from bottom to top, while those from setup B exhibit a more homogenous (200) and (222) orientation. Using gas flow setup C, a less pronounced (111) and (220) orientation could be observed.

Table I: Coating texture in relation to gas flow setup and specimen position

A	top		middle			bottom
	R <sub>1/2</sub>	R <sub>0</sub>	R <sub>1/2</sub>	R	R <sub>1/2</sub>	
111	0.61	1.11	1.05	1.07	2.54	
222	2.49	1.94	1.83	1.70	0.06	
311	1.60	1.53	1.31	1.28	0.44	
220	0.19	0.38	0.50	0.59	1.94	
200	0.10	0.04	0.31	0.36	0.02	

B	top		middle			bottom
	R <sub>1/2</sub>	R <sub>0</sub>	R <sub>1/2</sub>	R	R <sub>1/2</sub>	
111	0.16	0.11	0.50	0.17	0.53	
222	1.04	1.16	1.20	1.05	1.55	
311	0.83	0.88	0.88	0.89	0.87	
220	0.90	0.81	0.93	0.91	0.70	
200	2.06	2.04	1.50	1.97	1.34	

C	top		middle			bottom
	R <sub>1/2</sub>	R <sub>0</sub>	R <sub>1/2</sub>	R	R <sub>1/2</sub>	
111	1.44	1.21	1.34	1.24	0.86	
222	0.70	0.78	0.70	0.78	1.01	
311	0.81	0.79	0.79	0.78	0.85	
220	1.16	1.17	1.21	1.17	1.04	
200	0.89	1.04	0.97	1.04	1.25	



T.C. > 1,6  
1,2 < T.C. < 1,6  
T.C. < 0,7

## Coating Topography

SEM top view images along the reactor height are shown in Fig. 7. The samples positioned on the middle level of each gas flow setup show similar topography, and thus only the R<sub>1/2</sub> positions are shown. The slightly different appearance of the bottom levels agree with the determined textures. The fine grained structure at the bottom level in gas flow setup A fosters the proposed effect of a less pre-heated feed gas and the high supersaturation. A coarsening of the topography and the structure can be seen with increasing C/(C+N) ratio for all gas flow setups investigated (compare Figs. 4 and 7), stronger from A to B and less pronounced from B to C. The observed structures agree well with observations of Cheng et al. [16] who studied the effect of deposition temperature and C/(C+N) ratio on the morphology of TiCN coatings.

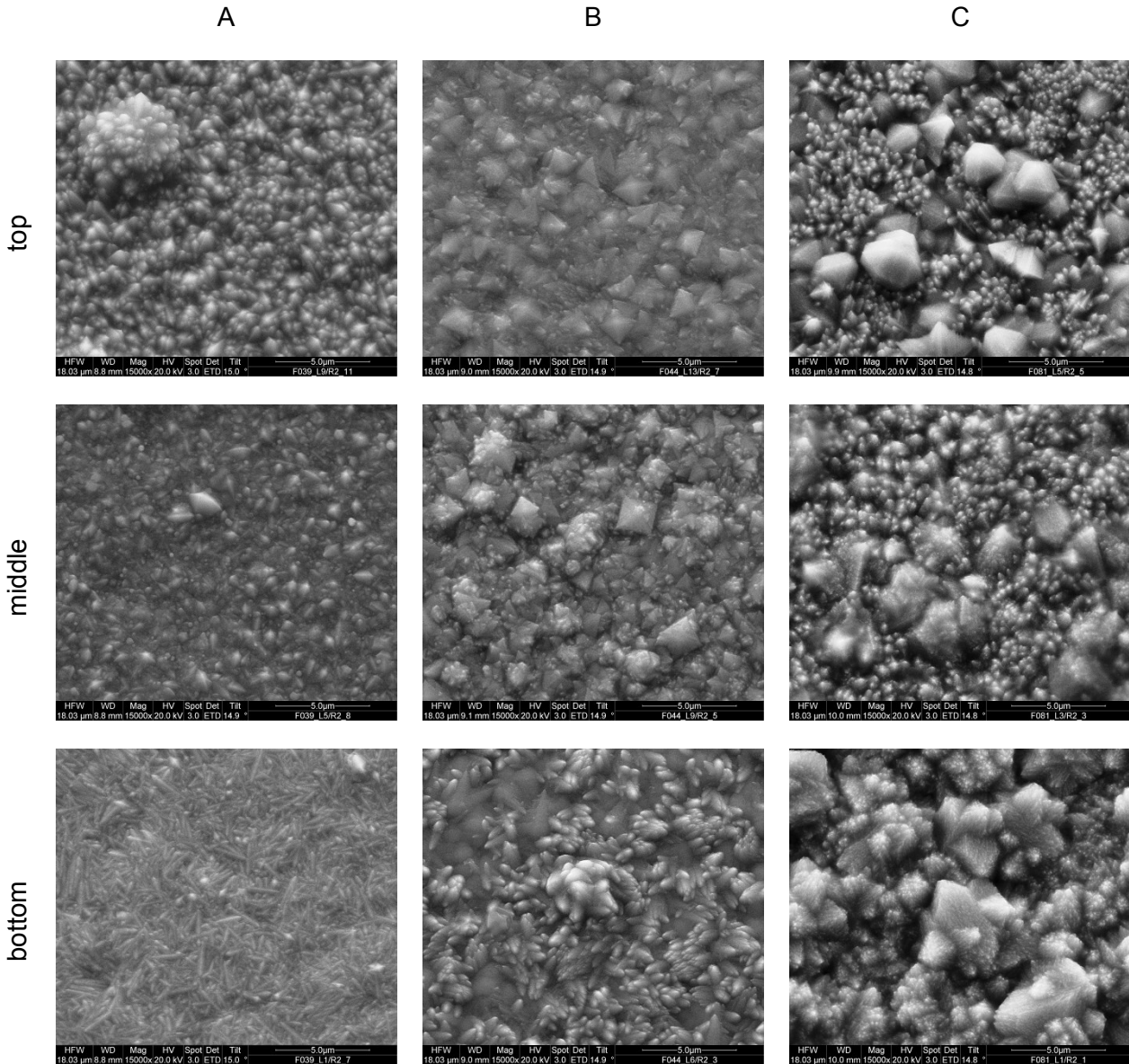


Fig. 7: SEM top view images in relation to gas flow setups and reactor height at position  $R_{1/2}$

## Conclusions

Three different gas flow setups were used for the deposition of TiCN coatings onto cemented carbide inserts in a computer controlled industrial scale hot wall CVD reactor, where setup A corresponds to a feed gas supply only from the bottom of the reactor, B has additional supplies from the circumference of the reactor, and C uses a central feed gas supply. The effect of these three different setups on coating mass gain, thickness, C/(C+N) ratio, preferred orientation, internal stresses and surface topography was investigated. All three setups showed uniform growth conditions and low scattering regarding to mass gain and coating thickness over all investigated specimen positions. Although the C/(C+N) ratio inside the reactor is quite homogenous, a pronounced shift in the C/(C+N) ratio was observed within the different setups comprising 0.45, 0.65, and 0.74 for setup A, B, and C, respectively, which can be attributed to an inadequate pre-heating of the feed gas. Setup A has shown a pronounced (222) and (311) orientation of the TiCN phase while those from setup B exhibit a more homogenous (200) and (222) orientation, and setup C a less pronounced (111) and (220) orientation. The intrinsic tensile stresses were in the range of 380 to 559 MPa, where the gas flow system C provides best uniformity. Furthermore, the surface topography of the coatings was found to be most homogenous for setup C. In conclusion, the central feed gas supply provides superior conditions for thermal chemical deposition of TiCN hard coatings.



## Acknowledgments

Financial support by the Austrian Federal Government and the Styrian Provincial Government, within the research activities of the K2 Competence Center on “Integrated Research in Materials, Processing and Product Engineering”, operated by the Materials Center Leoben Forschung GmbH in the framework of the Austrian COMET Competence Center Programme, is gratefully acknowledged.

## References

1. D.T. Quinto, *Int. J. Refractory Metals & Hard Materials*. **14** [1-3], pp. 7-20. (1996)
2. H.G. Prengel, W.R. Pfouts, and A.T. Santhanam, *Surface and Coatings Technology*. **102**, pp. 183-190. (1998)
3. F.W. Bach, K. Möhwald, and T. Wenz, *Moderne Beschichtungsverfahren*, pp: Wiley-VCH(2005)
4. J.N. Lindström and K.G. Stjernberg. *Euro CVD V*, Uppsala, Sweden, pp. 169-182 (1985)
5. P. Brunner. *Euro CVD III*, Neuachtel, Switzerland, pp. 56-70 (1980)
6. R. Bonetti and H. Wahl. *Euro CVD IV*, Eindhoven, Netherlands, pp. 510-516 (1983)
7. S. Rупpi, *J. De Physique IV*. **11** [Pr3], pp. 847-859. (2001)
8. M. Klaus, C. Genzel, and H. Holzschuh, *Thin Solid Films*. **517** [3], pp. 1172-1176. (2008)
9. A. Larsson and S. Rупpi, *Thin Solid Films*. **402** [1-2], pp. 203-210. (2002)
10. Z.J. Liu, Z.K. Liu, C. McNerny, P. Mehrotra, and A. Inspektor, *Surface & Coatings Technology*. **198** [1-3], pp. 161-164. (2005)
11. HSC Chemistry, ver. 6.12, Outotec Research Oy, (2007)
12. D.D. Klemm, *Mineralogische Monatshefte*, pp. 32-41. (1962)
13. K. Aigner, W. Lengauer, D. Rafaja, and P. Etmayer, *J. Alloys and Compounds*. **215**, pp. 121-126. (1994)
14. W. Lengauer, S. Binder, K. Aigner, P. Etmayer, A. Guillou, A. Debuigne, and G. Groboth, *J. Alloys and Compounds*. **217**, pp. 137-147. (1995)
15. K. Wolkulska, *J. Alloys and Compounds*. **264**, pp. 223-227. (1998)
16. D.J. Cheng, W.P. Sun, and M.H. Hon, *Thin Solid Films*. **146** [1], pp. 45-53. (1987)
17. H.O. Pierson, *Handbook of Chemical Vapor Deposition*, Noyes Publications. New Jersey. (1999)
18. J. Wagner, C. Mitterer, M. Penoy, C. Michotte, W. Wallgram, and M. Kathrein. *Proc. 16th Int. Plansee Seminar*, Reutte, pp. 917-931 (2005)
19. G.B. Harris, *Philosophical Magazine*. **43** [336], pp. 113-123. (1952)

## **Publication II**

### **Stress state of CVD TiCN/ $\kappa$ -Al<sub>2</sub>O<sub>3</sub> hard coatings**

C. Czettl, C. Mitterer, M. Penoy, C. Michotte, M. Kathrein

SMT24, Fraunhofer Institute for Material and Beam Technology IWS Dresden, 2010

## Stress state of CVD TiCN/ $\kappa$ -Al<sub>2</sub>O<sub>3</sub> hard coatings

C. Czettl\*, C. Mitterer\*\*, M. Penoy\*\*\*, C. Michotte\*\*\*,  
M. Kathrein\*\*\*\*

\* Materials Center Leoben Forschung GmbH, Leoben, Austria

\*\* Department of Physical Metallurgy and Materials Testing, Montanuniversität, Leoben, Austria

\*\*\* CERATIZIT Luxembourg S. à. r. l., Mamer, Luxembourg

\*\*\*\* CERATIZIT Austria GmbH, Reutte, Austria

### Abstract

TiCN/Al<sub>2</sub>O<sub>3</sub> hard coatings grown by chemical vapour deposition (CVD) are frequently utilized as wear resistant coatings on cemented carbide cutting tools. The stress state in the surface design of the tool i.e. substrate and coating architecture is considered as crucial for its performance. Therefore, three differently designed  $\kappa$ -Al<sub>2</sub>O<sub>3</sub> layers were deposited using an industrial-scale low-pressure CVD system onto a defined TiCN base layer, i.e. two single  $\kappa$ -Al<sub>2</sub>O<sub>3</sub> layers, with and without TiCN/TiN top coating, as well as a multilayer oxide arrangement with TiN/TiNB interlayer. The top coating comprises a sequence of TiCN and TiN layers. Microstructural and stress analysis was done by X-ray diffraction (XRD) and showed significant differences depending on the coating architecture. Single layer oxide and multilayer oxide coatings showed comparable stress profiles whereas a decrease of tensile stresses for the top coating architecture, caused by an intense crack network and compressive stress in the uppermost region were measured. This can be explained by the thermal mismatch of the TiN and  $\kappa$ -Al<sub>2</sub>O<sub>3</sub> layers. The surface topography as well as fracture cross-sections were investigated by scanning electron microscopy (SEM) and show the grain-finishing effect of the multilayer oxide arrangement. The chemical composition of the multilayer oxide was analysed by glow discharge optical emission spectroscopy (GDOES), excluding boron diffusion from the interlayer into the base layer or cemented carbide interface. The cutting performance was determined for the three different coating systems in turning and milling operations. In turning, all layer architectures showed comparable lifetime, whereas the milling operation is more sensitive on the stress state of the coating. There, the reduced tensile or even compressive stresses of the coating architecture with TiCN/TiN top coating led to an improvement of durability in interrupted cutting operation.

**Keywords:** CVD, hard coating, TiCN, Al<sub>2</sub>O<sub>3</sub>, residual stress

## 1. Introduction

Machining is one of the most important manufacturing technologies for wrought material and finished metal products. To perform metal cutting operations like milling, turning, parting and grooving, cost-effective tools with high durability are needed [1]. Iron-based work piece materials like steels represent an important fraction of metals to be cut. Especially for turning and milling of carbon steels and low-alloyed steels, coated cemented carbide indexable inserts are used. The most frequently applied coating technologies to increase the lifetime of these inserts are physical vapour deposition (PVD) and chemical vapour deposition (CVD). CVD is the dominating technology when thick coatings up to 25  $\mu\text{m}$  total thickness including alumina ( $\text{Al}_2\text{O}_3$ ) layers with their high hot hardness, thermal resistivity and oxidation resistance are needed [2, 3]. Those coatings consist typically of an architecture including a base layer of titanium carbonitride TiCN [4, 5], a bonding layer composed of (Ti, Al),(C, N, O, B) [6-8] and alumina in its  $\alpha$ - or  $\kappa$ -modification [9, 10]. The  $\text{Al}_2\text{O}_3$  polymorphs differ significantly in thermal conductivity, where  $\kappa$ - $\text{Al}_2\text{O}_3$  shows a three times lower thermal conductivity compared to the  $\alpha$ -modification [11]. Alumina can be deposited as single layer or multilayer coating [12-14], with and without top coating which consists usually of a combination of TiCN and TiN to achieve the shiny gold colour for better wear indication [15].

In CVD processes, the high deposition temperatures of 900 to 1050  $^\circ\text{C}$  and the differing thermal expansion coefficients of cemented carbide substrates and coating layers, which are in a range of  $4 - 8 \cdot 10^{-6} \text{ K}^{-1}$  and  $7.0 - 9.4 \cdot 10^{-6} \text{ K}^{-1}$  for the materials mentioned above, respectively [16-18], lead to disadvantageous tensile stresses and crack networks during the cooling sequence [19]. Thus, the aim of this study was to investigate the influence of the coating design on the residual stress in  $\kappa$ - $\text{Al}_2\text{O}_3$  layers grown on a TiCN base layer. Three different architectures are compared with respect to their composition and microstructure, residual stress, hardness, elastic modulus and cutting performance, i.e. a single layer  $\kappa$ - $\text{Al}_2\text{O}_3$ , a multilayer arrangement consisting of three  $\kappa$ - $\text{Al}_2\text{O}_3$  layers separated by a TiN-TiNB-TiN interlayer sequence, and a single layer  $\kappa$ - $\text{Al}_2\text{O}_3$  with TiCN-TiN top coating.

## 2. Experimental details

The deposition runs were carried out in an industrial-scale low-pressure CVD unit. All samples were placed in the centre of the batch, on the half radius of the tray, as described in [20]. The TiCN base layer was deposited using the medium temperature CVD process (MT-CVD) [4, 5] at 900  $^\circ\text{C}$  and a deposition pressure of 100 mbar. The used feed gas composition was 22.8 vol.-%  $\text{N}_2$ , 74.6 vol.-%  $\text{H}_2$ , 1.9 vol.-%  $\text{TiCl}_4$  and 0.7 vol.-%  $\text{CH}_3\text{CN}$ . The  $\kappa$ - $\text{Al}_2\text{O}_3$  was deposited on a (Ti),(C, N, O) adhesion layer [6] at 1000  $^\circ\text{C}$  deposition temperature and 75 mbar deposition pressure. The feed

gas was composed of 92.2 vol.-% H<sub>2</sub>, 1.8 vol.-% AlCl<sub>3</sub>, 3.7 vol.-% CO<sub>2</sub> and 2.1 vol.-% HCl. 0.3 vol.-% H<sub>2</sub>S was used as catalytic agent [21, 22]. Three different coating architectures have been synthesized on the TiCN base layer and the adhesion layer: (i) a single layer  $\kappa$ -Al<sub>2</sub>O<sub>3</sub>, (ii) a multilayer arrangement consisting of three  $\kappa$ -Al<sub>2</sub>O<sub>3</sub> layers separated by a 0.7  $\mu$ m thick TiN-TiNB-TiN interlayer sequence, and (iii) a single layer  $\kappa$ -Al<sub>2</sub>O<sub>3</sub> with 0.3  $\mu$ m thick TiCN and TiN bi-layer top coating. The total coating thicknesses including base and adhesion layers were 15  $\mu$ m and 6  $\mu$ m, respectively, where the thicker coatings were used for analytical investigations and turning tests and the thinner ones for milling tests.

The analytical investigations were carried out on 12 wt.-% Co cemented carbide inserts with mixed carbides in SNUN 120412 geometry coated with 10  $\mu$ m TiCN including the adhesion layer and 5  $\mu$ m  $\kappa$ -Al<sub>2</sub>O<sub>3</sub>. The characterization of the surface topography and fracture cross-sections was conducted using a Quanta FEI 200 scanning electron microscope (SEM). The coating thickness was determined by light optical microscopy (LOM) on polished cross-sections. The qualitative chemical composition was determined using a Jobin-Yvon Horiba JY10000 glow discharge optical emission spectroscope (GDOES) [23]. Microstructural characterization and stress measurements were done using a Panalytical X'Pert Pro diffractometer and Cu K $\alpha$  radiation. The determination of the phase composition was carried out using glancing angle X-ray diffraction (GAXRD) with 2° incidence angle. The  $\sin^2 \Psi$  method at  $2\theta=56^\circ$  using the sum of the (204) peak at 55.884° and the (134) peak at 56.033° was applied for determining the residual stress in the Al<sub>2</sub>O<sub>3</sub> layers [24, 25]. This method is limited to penetration depths above 0.5 to 0.7  $\mu$ m and assumes a biaxial stress state in an isotropic material. Gradients of indentation hardness and indentation modulus were measured using a CSM Nanoindenter. The measurements were carried out on polished inclined cross-sections of 10° using a Berkovich indenter and loads of 12.5 mN and 20 mN. The indentation hardness and indentation modulus was calculated using the method of Oliver and Pharr [26].

All inserts for the cutting experiments were post-treated using an abrasive wet blasting process [27]. For turning tests, P25 substrates with 7 wt.-% Co, mixed carbides and Co-enriched surface zone [28] in CNMG 120412-EN TRM geometry were used. The turning test was a segment turning test, which is a combination of face- and longitudinal turning operation, on DIN 1.7225 (42CrMo4) low-alloyed steel with cutting speed  $v_c = 220$  m/min and feed rate  $f = 0.4$  mm. Each segment consists of six cuts, i.e. three face and three longitudinal cuts with a varied depth of cut  $a_p = 3, 2$  and 1 mm. The turning tests were carried out using a coating architecture of 15  $\mu$ m total thickness (10  $\mu$ m TiCN including the adhesion layer and 5  $\mu$ m  $\kappa$ -Al<sub>2</sub>O<sub>3</sub>), whereas in milling a lower total coating thickness is needed to achieve sufficient toughness of the tool [29, 30]. Therefore, the fractions of TiCN and  $\kappa$ -Al<sub>2</sub>O<sub>3</sub> were reduced to 4  $\mu$ m and 2  $\mu$ m, respectively, giving a total thickness of 6  $\mu$ m. The milling tests were carried out with WC-Co substrates with 10 wt.-% Co in

RPHX 1204MO-EN M31 geometry. The milling test was a single edge milling test with cutting speed  $v_c = 220$  m/min, feed rate per tooth  $f_z = 0.4$  mm, depth of cut  $a_p$  2.5 mm and contact width  $a_e = 40$  mm on DIN 1.4021 (X20Cr13) martensitic steel.

### 3. Results and discussion

#### Coating structure

SEM top-view images and fracture cross-sections were recorded to compare the surface topography and morphology of the different coating architectures. The columnar growth of the TiCN base layer is visible in Fig. 1 for all three coatings.

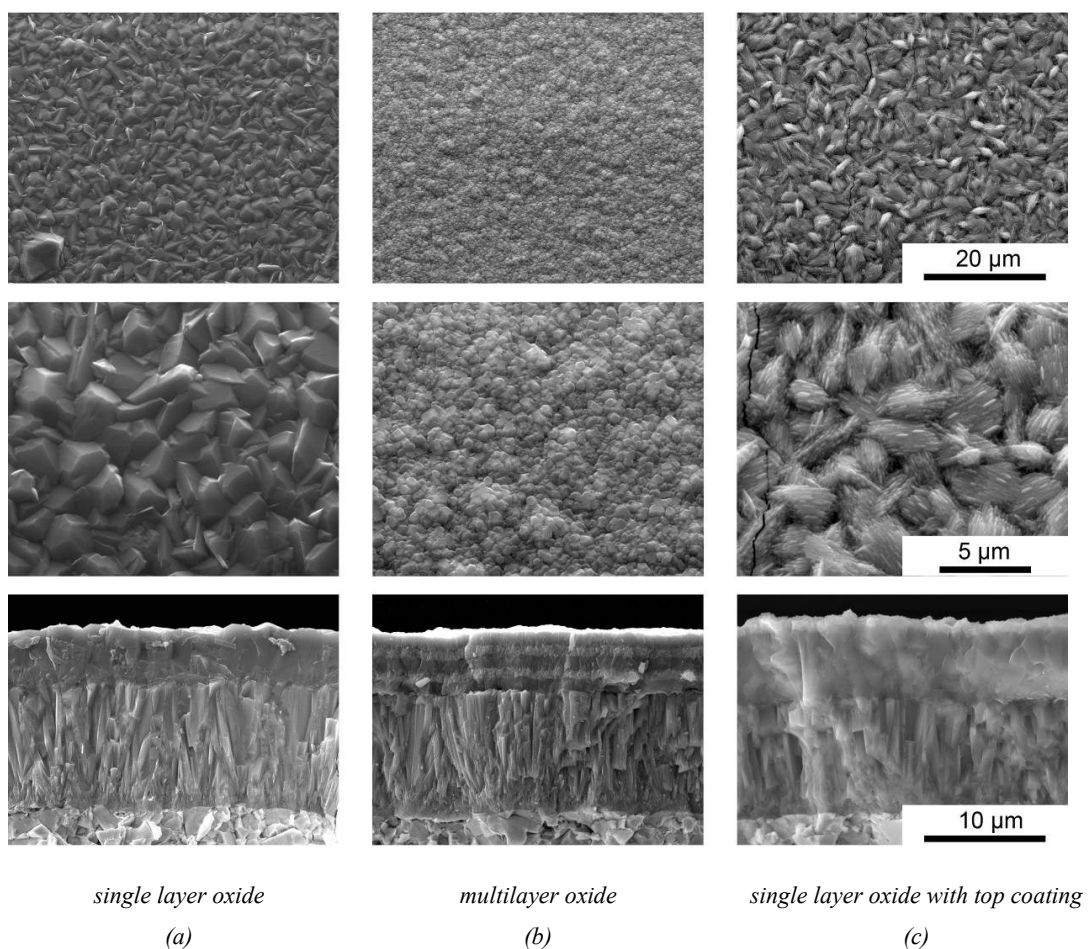


*Fig. 1: SEM images of the surface topography (i.e. the outermost layer, as shown in the upper two rows) and fracture cross-sections (lower row) of single layer oxide coating (a), multilayer oxide coating (b) and single layer oxide with TiCN-TiN top coating (c)*

Fig. 1 (a) shows the fine-grained  $\kappa$ -Al<sub>2</sub>O<sub>3</sub> as outermost layer with an average grain size  $< 3$   $\mu$ m. The interruption of the V-shaped growth of the  $\kappa$ -Al<sub>2</sub>O<sub>3</sub> layer [31] by the interlayer sequence and the following re-nucleation lead to a finer oxide structure with grain sizes  $< 0.8$   $\mu$ m for the multilayer coating (c.f. Fig. 1 (b)). The thin TiCN-TiN top coating covers the  $\kappa$ -Al<sub>2</sub>O<sub>3</sub> grains with a very fine structure, where the underneath  $\kappa$ -Al<sub>2</sub>O<sub>3</sub> structure is still visible (compare Fig. 1 (c) and Fig. 1 (a)).

For the latter coating, formation of tensile cracks is seen in the top-view images, which are typical for CVD alumina coatings on cemented carbide substrates [19] and could also be detected for the other coatings investigated.

From previous work [25] it is known that the chemical composition of the  $\kappa$ -Al<sub>2</sub>O<sub>3</sub> layers grown under comparable conditions is stoichiometric. Here, we focus on the composition of the multilayer oxide coating, containing the TiN-TiNB-TiN interlayer sequence. There, the addition of boron has been reported to result in a fine-grained structure, an increase of hardness and beneficial tribological properties [32]. However, the high mobility of boron at substrate temperatures of 1000 °C, as necessary for the deposition of Al<sub>2</sub>O<sub>3</sub>, in combination with disadvantageous process parameters can lead to a contamination of the MT-TiCN base layer or even to the formation of the Co-W-B phase at the cemented carbide interface, which deteriorates coating adhesion [33]. Fig. 2 shows the GDOES depth profile of the multilayer coating, where the interlayers are clearly visible. The boron can be found within the interlayer and no diffusion into  $\kappa$ -Al<sub>2</sub>O<sub>3</sub>, TiCN or the substrate material could be observed.

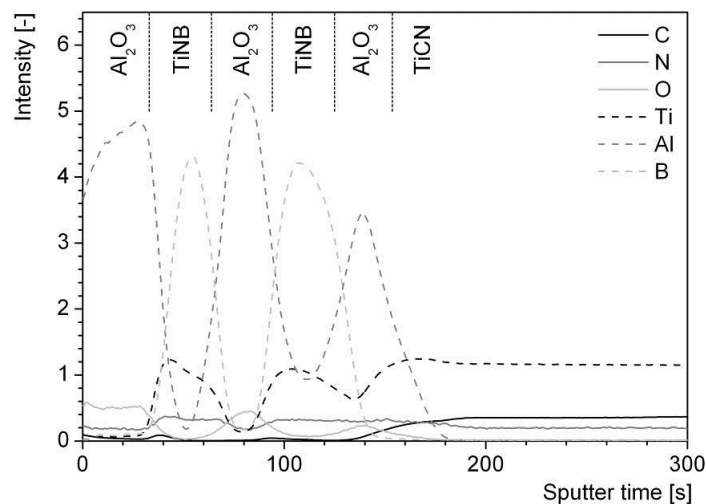


Fig. 2: Qualitative GDOES depth profile of the multilayer  $\kappa$ -Al<sub>2</sub>O<sub>3</sub> coating with TiN-TiNB-TiN interlayer

Fig. 3 shows the GAXRD patterns of the three different layer architectures deposited. The main phases identified are  $\kappa$ -Al<sub>2</sub>O<sub>3</sub>, TiN from the top coating and interlayer, TiCN from the base layer and Ti<sub>2</sub>O<sub>3</sub>, which is present in the bonding layer. The TiCN-TiN top coating leads to a reduction of the intensity of the  $\kappa$ -Al<sub>2</sub>O<sub>3</sub> peaks compared to the single layer without top coating. The multilayer arrangement showed very strong TiN peaks, which arise from the TiN-TiNB-TiN interlayer. The Ti<sub>2</sub>O<sub>3</sub> phase is part of the oxide bonding layer which is present at the nitride-oxide and the oxide-nitride interfaces. It can be found in the multilayer as well as in the single layer with top coating architecture, because of the lower distances of these interfaces to the surface compared to the single layer without top coating.





elaborated the correlation of crack network density and residual stress obtained by the  $\sin^2 \Psi$  method in  $\text{Al}_2\text{O}_3$  as a consequence of mechanical post-treatment using steel balls, where a more intense post-treatment consequences a higher crack density and decreasing residual tensile stress. Both groups report on a beneficial influence of the stress state of the modified coating surfaces, especially in interrupted cutting operation. In contrast, Barbatti et al. [27] investigated the as-deposited and post-treated stress profiles of the uppermost region of  $\kappa\text{-Al}_2\text{O}_3$  layers without top coating by a synchrotron X-ray method, using a wet abrasive micro-blasting process. No significant influence of blasting on the stress state has been reported. Higher blasting pressures result in crack formation and propagation, but no plastic deformation or increased defect density in near-surface zone of the  $\kappa\text{-Al}_2\text{O}_3$  layers could be observed by transmission electron microscopy.

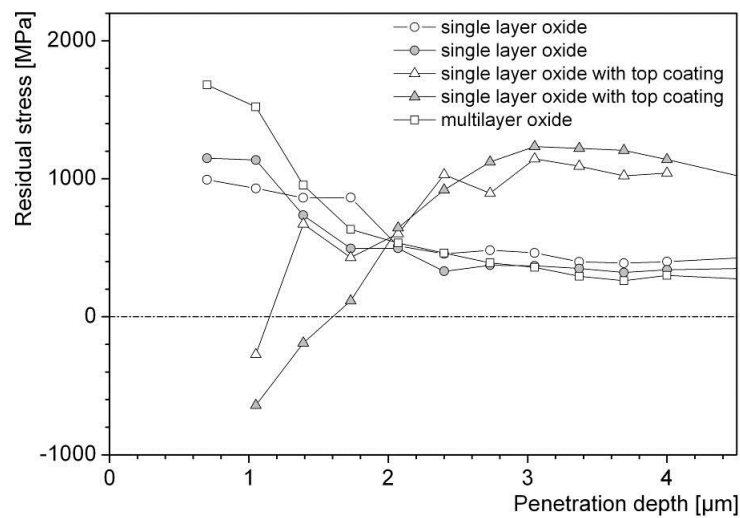


Fig. 4: Residual stress within the  $\kappa\text{-Al}_2\text{O}_3$  layer versus depth for the single layer oxide coating, multilayer oxide coating and single layer oxide with TiCN-TiN top coating. For both single layer coating types, two samples have been grown using the same deposition parameters to confirm the reproducibility

To illuminate the origin of the differences of the stress profiles presented in Fig. 4, a combination of LOM and SEM images of the polished surfaces is shown in Fig. 5. There, the visible TiCN particles originate from dust formation during the CVD process [36]. A significant difference of the single layer oxide with top coating compared to both, the single layer oxide and multilayer arrangements without top coating becomes visible. The intense crack network seen for the top coating (see Fig. 5 (c)) compared to those architectures without top coating (see Fig. 5 (a) and Fig. 5 (b)) might be attributed to the stress in the top coating and the lower tensile or even compressive stress within the  $\text{Al}_2\text{O}_3$  layer, as determined by XRD (see Fig. 4).

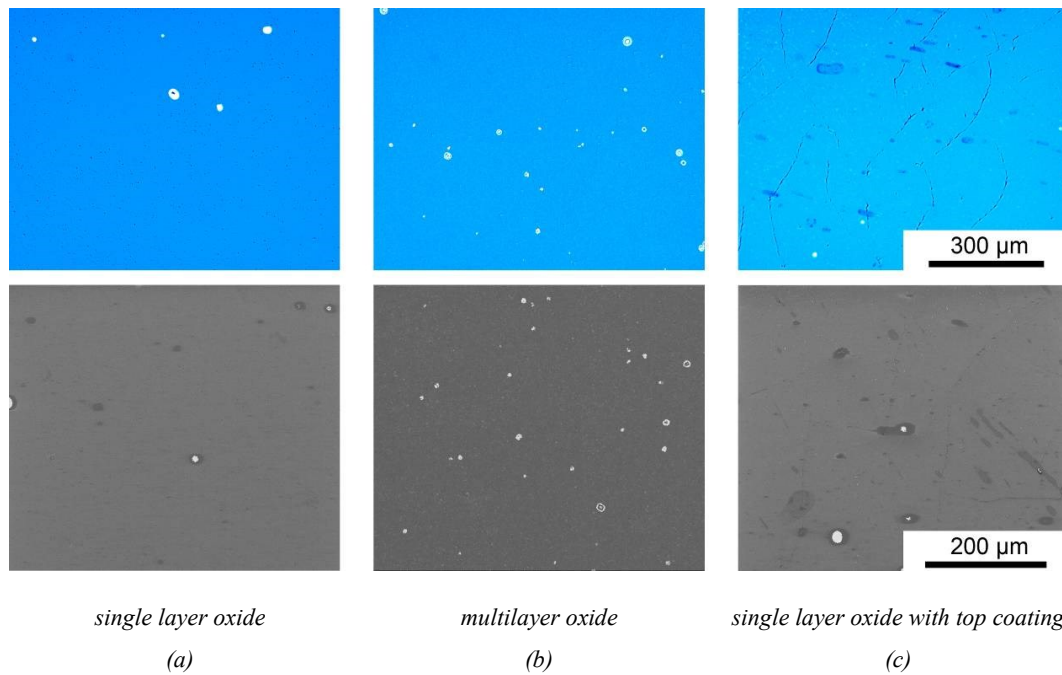


Fig. 5: LOM (upper row) and SEM (lower row) top view images of polished  $\kappa$ -Al<sub>2</sub>O<sub>3</sub> surfaces of single layer oxide coating (a), multilayer oxide coating (b) and single layer oxide with TiCN-TiN top coating (c). The bright areas indicate TiCN particles arising from dust formation during coating deposition

The higher thermal expansion coefficient of TiN ( $9.35 \cdot 10^{-6} \text{ K}^{-1}$  [31]) compared to  $\kappa$ -Al<sub>2</sub>O<sub>3</sub> ( $4 - 8 \cdot 10^{-6} \text{ K}^{-1}$  [17]) leads on the one hand to the formation of tensile stresses in the top coating during cooling down after deposition, which induces crack nucleation and propagation from the surface of the coating, obviously also through the  $\kappa$ -Al<sub>2</sub>O<sub>3</sub> layer (c.f. Fig. 1 (c)). On the other hand, these tensile stresses in the top coating have to be balanced by compressive stresses in the  $\kappa$ -Al<sub>2</sub>O<sub>3</sub> layer, provided that the strength of the top coating/ $\kappa$ -Al<sub>2</sub>O<sub>3</sub> interface is sufficient. Furthermore, compressive stresses are also retained within the islands between the crack network, where the fracture strength has not been reached, again provided that interfacial adhesion withstands the loads imposed by these stresses. The lower tensile stresses close to the surface of those coating architectures without top coating yields less crack formation, and thus less relaxation of tensile stresses via a crack network. It should be mentioned here that the described relaxation of tensile stresses by the top coating could not be observed, when TiN is used as an interlayer between two  $\kappa$ -Al<sub>2</sub>O<sub>3</sub> layers, like in the multilayer arrangement.

The indentation hardness and indentation modulus were determined for both single layer oxide coatings with and without top coating. The small layer thickness prevents these measurements for the multilayer coating. Depth profiles of indentation hardness and indentation modulus obtained by measurements on tapered polished cross-sections are shown in Fig. 6. The difference of indentation modulus of the TiCN base layer and the  $\kappa$ -Al<sub>2</sub>O<sub>3</sub> layers with 460 GPa and 340 GPa, respectively, is clearly visible. The obtained indentation hardness values of 25 GPa for TiCN and 22 GPa for  $\kappa$ -Al<sub>2</sub>O<sub>3</sub> correspond well to literature [37, 38]. For the single layer oxide with top coating,

the two different loads of 12.5 mN and 20 mN show similar indentation hardness and indentation moduli, which indicates a sufficient remaining layer thickness in the inclined section. No significant difference of indentation hardness and indentation modulus could be found for the single layer oxide coating with and without top coating. Moreover, due to its small thickness, the top coating could not be clearly distinguished from the  $\kappa$ -Al<sub>2</sub>O<sub>3</sub> layer. Obviously both, indentation hardness and indentation modulus seem to be not significantly influenced by the different stress values. Since it is well known that strength and hardness of polycrystalline materials are affected by the stress state [39, 40] it has to be concluded that either the applied measurement method is not sensitive enough or the effect of stress on the hardness is relatively low.

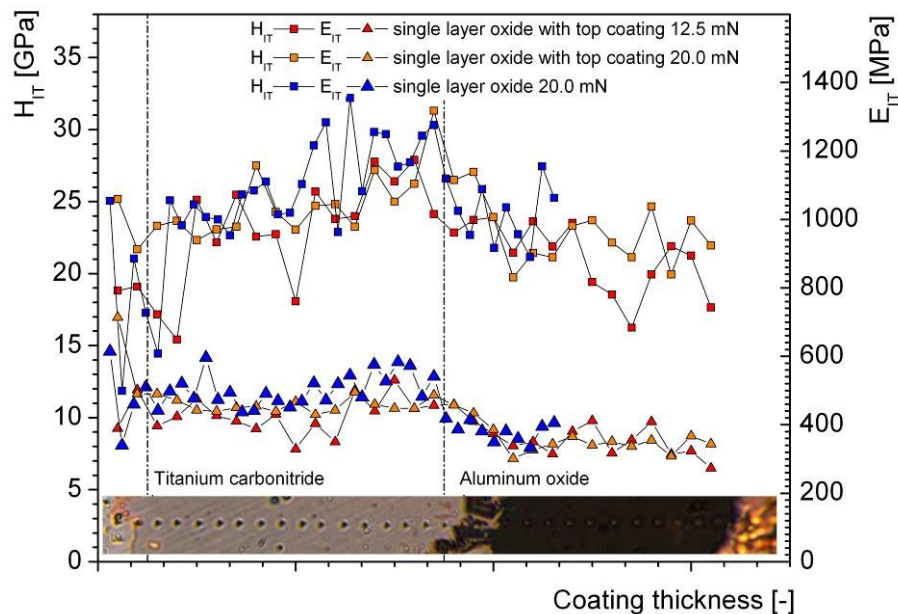
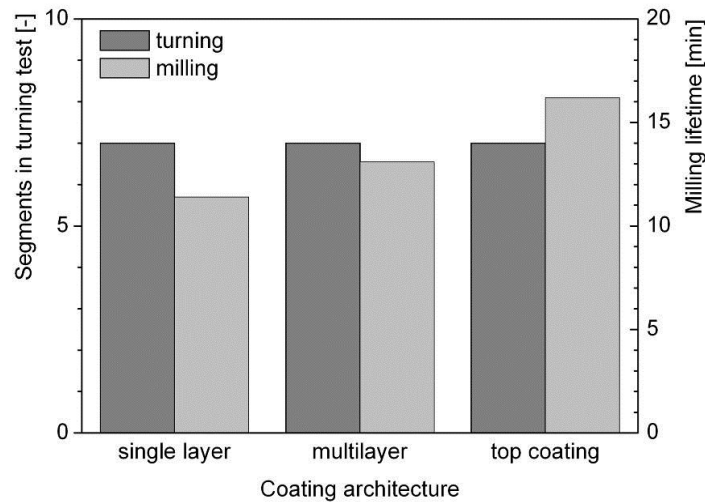


Fig. 6: Indentation hardness  $H_{IT}$  and indentation modulus  $E_{IT}$  of single layer coatings with and without top coating measured on a tapered polished cross-sections. The sample with top coating has been measured using two different indentation loads.

### Cutting performance

Cutting tests were done for two different cutting applications to compare the synthesized coating concepts in turning and milling. Turning is mainly characterised by abrasive wear on the flank and the rake face of the tool. In addition, sufficient toughness is necessary on the nose of the insert, especially in face turning. The lifetime of the insert is limited by the maximum flank wear or crater wear, which depends on the layer thickness [12, 41-43]. The main failure mechanism in milling is abrasive wear on the flank side of the insert and thermal fatigue due to thermal cyclic loads. These loads consequence thermal cracks at the cutting edge, which reach completely through the coating into the substrate material. Finally, the rupture between two of these cracks limits the lifetime of the tool [44]. Fig. 7 shows that the cutting performance of all three coating architectures investigated in turning is comparable, i.e. within the scattering of the applied segment turning test. In the milling

test, the single layer architecture with top coating showed the highest lifetime until a maximum flank wear of 0.3 mm was reached. A repetition of the experiments after removing the top coating by dry abrasive blasting with  $\text{Al}_2\text{O}_3$  before the post-treatment to exclude tribological effects due to the different friction coefficients of TiN [45] and  $\text{Al}_2\text{O}_3$  [46] led to a similar result.



*Fig. 7: Cutting performance of single layer oxide coating, multilayer oxide coating and single layer oxide with TiCN-TiN top coating in turning and milling operations.*

SEM observations of the worn inserts were performed after the cutting tests to identify the different wear mechanisms. Fig. 8 illustrates the crater wear on the rake face of the inserts after turning of seven segments, when the flank wear is comparable for the different coating architectures. Both, the  $\text{Al}_2\text{O}_3$  as well as TiCN layers are worn through and work piece material adheres to the cemented carbide substrate for all three samples. A detailed view of the cutting edge on the radius of the insert shows an insufficient adhesion of the multilayer architecture (c.f. Fig. 8 (b)), indicated by failure at the oxide-nitride interfaces. The dark grey  $\text{Al}_2\text{O}_3$  in Fig. 8 (c) can be distinguished from the light grey TiN/TiCN of the top coating, which is still visible at the cutting edge.

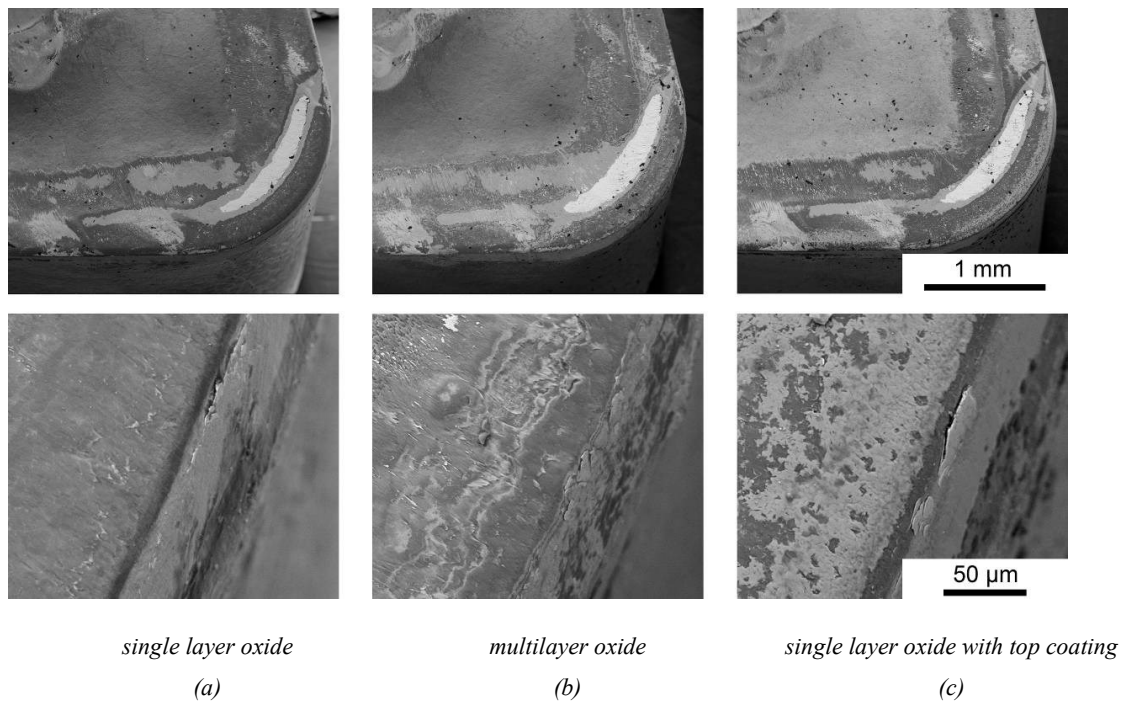


Fig. 8: SEM micrographs of the surfaces of worn cutting inserts coated with single layer oxide coating (a), multilayer oxide coating (b) and single layer oxide with TiCN-TiN top coating (c) after turning of 7 segments

SEM observations of the worn milling inserts make the damage due to thermal fatigue visible. Thermal cracks formed perpendicular to the cutting edge lead to failure of the insert with the single layer oxide coating (see Fig. 9 (a)). Similar to turning, the weak adhesion of the oxide-nitride interface of the multilayer oxide architecture caused failure of the coating at the cutting edge. This leads to more pronounced thermal crack growth (c.f. Fig. 9 (b)), due to absence of thermal protection of the substrate. The single layer oxide architecture with top coating (c.f. Fig. 9 (c)) showed minimal thermal cracks after 15 % higher cutting time, when reaching the lifetime criterion of 0.3 mm maximum flank wear.

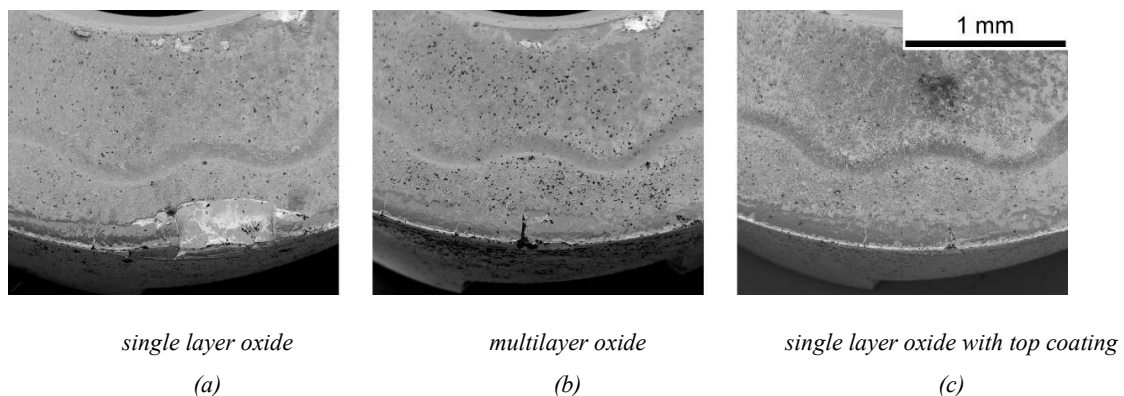


Fig. 9: SEM micrographs of the rake face of worn milling inserts coated with single layer oxide coating (a), multilayer oxide coating (b) and single layer oxide with TiCN-TiN top coating (c)

## 4. Summary and conclusions

Three different layer architectures deposited by low-pressure chemical vapour deposition onto cemented carbide cutting inserts were compared regarding to internal stresses and cutting performance in turning and milling. A single layer  $\kappa$ -Al<sub>2</sub>O<sub>3</sub>, a multilayer  $\kappa$ -Al<sub>2</sub>O<sub>3</sub> with TiN-TiNB-TiN interlayer, and a single layer  $\kappa$ -Al<sub>2</sub>O<sub>3</sub> with TiCN/TiN top coating were grown on a TiCN base layer. The obtained results enable to draw the following conclusions:

- The single layer oxide coating and the multilayer oxide coating without top coating showed comparable stress versus depth profiles, where the multilayer coating exhibited higher residual tensile stress values and failed in both turning and milling tests due to weak adhesion of the oxide-nitride interface.
- The deposition of a TiCN/TiN top coating on the single layer oxide yielded on the one hand higher tensile stresses in those parts of the  $\kappa$ -Al<sub>2</sub>O<sub>3</sub> layer close to the TiCN base layer; however, the different thermal expansion coefficients of top coating and alumina layer resulted in formation of compressive stresses in the areas closer to the surface. This coating architecture exhibits an intense crack network in the  $\kappa$ -Al<sub>2</sub>O<sub>3</sub> and top coating layers, enabling efficient relaxation of tensile stresses while compressive stresses are maintained in those areas without cracks.
- The reduction of tensile stresses due to the top coating leads to a significant improvement of durability in interrupted milling where flank wear and thermal fatigue limits lifetime. This operation is obviously more sensitive on the stress state of the coating than turning.

In summary, it has been shown that by applying a suitable coating architecture to CVD coated cemented carbide inserts beneficial stress versus depth profiles can be obtained which are highly efficient in improving their performance in interrupting cutting. The effect of a  $\kappa$ -Al<sub>2</sub>O<sub>3</sub> layer thermally constrained by a TiCN/TiN top coating is assumed to be comparable to compressive mechanical stresses introduced by post-treatment blasting processes.

### Acknowledgements

Financial support by the Austrian Federal Government and the Styrian Provincial Government, within the research activities of the K2 Competence Center in the framework of the Austrian COMET Competence Center Programme, is gratefully acknowledged.

## References

- [1] B. Mills, *Journal of Materials Processing Technology* 56/1-4 (1996) 16.
- [2] S. Ruppi, *Journal De Physique IV* 11/Pr3 (2001) 847.
- [3] H. Holleck, *Journal of Vacuum Science & Technology* 4/6 (1986) 2611.
- [4] M. Bonetti-Lang, R. Bonetti, H.E. Hintermann, D. Lohmann, *International Journal of Refractory Metals and Hard Materials* 1/4 (1982) 161.
- [5] A. Larsson, S. Ruppi, *Thin Solid Films* 402/1-2 (2002) 203.
- [6] M. Halvarsson, H. Norden, S. Vuorinen, *Surface & Coatings Technology* 68 (1994) 266.
- [7] Z.J. Liu, Z.K. Liu, C. McNerny, P. Mehrotra, A. Inspektor, *Surface & Coatings Technology* 198/1-3 (2005) 161.
- [8] Z.J. Liu, C. McNerny, P. Mehrotra, Y.X. Liu, Z.K. Liu, *Journal of Phase Equilibria and Diffusion* 27/1 (2006) 30.
- [9] S. Ruppi, A. Larsson, *Thin Solid Films* 388/1-2 (2001) 50.
- [10] S. Ruppi, *Surface & Coatings Technology* 202/17 (2008) 4257.
- [11] D.G. Cahill, S.M. Lee, T.I. Selinder, *Journal of Applied Physics* 83/11 (1998) 5783.
- [12] W. Schintlmeister, W. Wallgram, J. Kanz, *Thin Solid Films* 107/2 (1983) 117.
- [13] M. Halvarsson, S. Vuorinen, *Materials Science and Engineering* 209/1-2 (1996) 337.
- [14] M. Halvarsson, S. Vuorinen, *Surface & Coatings Technology* 80/1-2 (1996) 80.
- [15] W.A. Bryant, G.P. Grab Patent No. US 4.984.940, 1991.
- [16] K. Wolkulska, *Journal of Alloys and Compounds* 264 (1998) 223.
- [17] M. Halvarsson, V. Langer, S. Vuorinen, *Surface & Coatings Technology* 76/1-3 (1995) 358.
- [18] K. Aigner, W. Lengauer, D. Rafaja, P. Ettmayer, *Journal of Alloys and Compounds* 215 (1994) 121.
- [19] D. Hochauer, C. Mitterer, M. Penoy, C. Michotte, H.P. Martinz, M. Kathrein, *Surface & Coatings Technology* 203/3-4 (2008) 350.
- [20] C. Czettl, C. Mitterer, C. Michotte, M. Penoy, M. Kathrein, in: L.S. Sigl, P. Rödhammer, H. Wildner (Eds.), *Plansee Seminar 2009*, Plansee Group, Reutte, Austria, Reutte, (2009), p. HM71.
- [21] S. Ruppi, A. Larsson, *Fifteenth International Symposium on Chemical Vapor Deposition*, The Electrochemical Society Inc., (2000), p. 372.
- [22] S. Ruppi, A. Larsson, *Journal De Physique IV* 9/P8 (1999) 349.
- [23] T. Nelis, J. Pallosi, *Applied Spectroscopy Reviews* 41/3 (2006) 227.
- [24] M. Birkholz, *Thin Film Analysis by X-Ray Scattering*, Wiley-VCH Verlag, Weinheim, 2006.
- [25] D. Hochauer, C. Mitterer, M. Penoy, C. Michotte, H.P. Martinz, M. Kathrein, *Surface and Coatings Technology* 204/21-22 (2010) 3713.
- [26] W.C. Oliver, P.G. M., *Journal of Materials Research* 7/6 (1992) 1564.
- [27] C. Barbatti, J. Garcia, R. Pitonak, H. Pinto, A. Kostka, A. Di Prinzio, M.H. Staia, A.R. Pyzalla, *Surface & Coatings Technology* 203/24 (2009) 3708.
- [28] W. Lengauer, K. Dreyer, *Journal of Alloys and Compounds* 338/1-2 (2002) 194.
- [29] B. Lux, R. Haubner, C. Wohlrab, *Surface & Coatings Technology* 38/3 (1989) 267.
- [30] W. Schintlmeister, W. Wallgram, J. Kanz, K. Gigl, *Zeitschrift für Metallkunde* 75/11 (1984) 874.
- [31] H.O. Pierson, *Handbook of Chemical Vapor Deposition*, Noyes Publications, New Jersey, 1999.
- [32] J. Wagner, D. Hochauer, C. Mitterer, M. Penoy, C. Michotte, W. Wallgram, M. Kathrein, *Surface & Coatings Technology* 201/7 (2006) 4247.
- [33] H. Holzschuh, *Thin Solid Films* 469-70 (2004) 92.

- [34] H. Holzschuh, M. Klaus, C. Genzel, *Advances in Powder Metallurgy & Particulate Materials*, Washington D.C., (2008), p. 100.
- [35] S. Katayama, M. Hashimura, *Journal of Manufacturing Science and Engineering* 119 (1997) 50.
- [36] K.L. Choy, *Progress in Materials Science* 45 (2003) 57.
- [37] S. Rупpi, A. Larsson, A. Flink, *Thin Solid Films* 516/18 (2008) 5959.
- [38] W. Lengauer, S. Binder, K. Aigner, P. Etmayer, A. Guillou, A. Debuigne, G. Groboth, *Journal of Alloys and Compounds* 217 (1995) 137.
- [39] C. Kittel, *Einführung in die Festkörperphysik*, Oldenbourg Wissenschaftlicher Verlag, München, 2006.
- [40] E. Doege, B.A. Behrens, *Handbuch der Umformtechnik*, Springer Heidelberg Dordrecht London New York, Berlin, 2007.
- [41] S. Coromant, *Handbuch der Zerspanung*, Sandvik Coromant, 1996.
- [42] T. Childs, K. Maekawa, T. Obikawa, Y. Yamane, *Metal Machining*, John Wiley, 2000.
- [43] G. Vieregge, *Zerspanung der Eisenwerkstoffe*, Verlag Stahleisen, Düsseldorf, 1970.
- [44] G.J. Wolfe, C.J. Petrosky, D.T. Quinto, *Journal of Vacuum Science & Technology* 4/6 (1986) 2747.
- [45] J. Wagner, C. Mitterer, M. Penoy, C. Michotte, W. Wallgram, M. Kathrein, *International Journal of Refractory Metals & Hard Materials* 26/2 (2008) 120.
- [46] G. Bolelli, V. Cannillo, L. Lusvarghi, T. Manfredini, *Wear* 261/11-12 (2006) 1298.



## **Publication III**

### **CO addition in low-pressure chemical vapour deposition of medium-temperature $\text{TiC}_x\text{N}_{1-x}$ based hard coatings**

C. Czettl, C. Mitterer, U. Mühle, D. Rafaja, S. Puchner, H. Hutter,  
M. Penoy, C. Michotte, M. Kathrein

Surface and Coatings Technology 206/7 (2011) 1691

## CO addition in low-pressure chemical vapour deposition of medium-temperature $\text{TiC}_x\text{N}_{1-x}$ based hard coatings

C. Czettl<sup>1</sup>, C. Mitterer<sup>2</sup>, U. Mühle<sup>3</sup>, D. Rafaja<sup>3</sup>, S. Puchner<sup>4,7</sup>, H. Hutter<sup>4</sup>,  
M. Penoy<sup>5</sup>, C. Michotte<sup>5</sup>, M. Kathrein<sup>6,\*</sup>

<sup>1</sup> Materials Center Leoben Forschung GmbH, Roseggerstraße 12, A-8700 Leoben, Austria

<sup>2</sup> Department of Physical Metallurgy and Materials Testing, Montanuniversität, Franz-Josef-Straße 18, A-8700 Leoben, Austria

<sup>3</sup> Institute of Materials Science, TU Bergakademie Freiberg, Gustav-Zeuner-Straße 5, D-09599 Freiberg, Germany

<sup>4</sup> Institute for Chemical Technologies and Analytics, Technische Universität Wien, Getreidemarkt 9/164, A-1060 Wien, Austria

<sup>5</sup> CERATIZIT Luxembourg S. à. r. l., Route de Holzem, L-8201 Mamer, Luxembourg

<sup>6</sup> CERATIZIT Austria GmbH, A-6600 Reutte, Reutte, Austria

<sup>7</sup> KAI - Kompetenzzentrum für Automobil- und Industrieelektronik GmbH, A-9524 Villach, Austria

### Abstract

$\text{TiC}_x\text{N}_{1-x}$  base layers with  $\text{Al}_2\text{O}_3$  top layers, both grown by chemical vapour deposition (CVD), are state-of-the-art in metal cutting with cemented carbide inserts. In order to influence the microstructure and properties of the base layer, five different  $\text{TiC}_x\text{N}_{1-x}$  coatings were grown by medium-temperature CVD with increasing CO fractions in the  $\text{TiCl}_4\text{-CH}_3\text{CN-H}_2\text{-N}_2\text{-CO}$  feed gas using an industrial-scale low-pressure CVD system. With the CO fraction in the feed gas rising up to 2.2 vol.-%, oxygen contents of 2.2 at.-% could be detected, which are distributed homogeneously over the coating thickness. The originally equiaxed  $\text{TiC}_x\text{N}_{1-x}$  grains with preferred (110) orientation obtained without CO addition change to randomly distributed plate-like grains, while the grain size decreases to the sub-micron range. Also the surface roughness decreases with rising CO addition. The incorporation of oxygen leads to a homogenous distribution of dislocations within the  $\text{TiC}_x\text{N}_{1-x}$  grains and to an increasing density of twin boundaries. The residual tensile stress shows a minimum of  $200\pm 47$  MPa, while the hardness increases to  $29.1\pm 1.3$  GPa and the elastic modulus reaches a maximum  $569\pm 29$  GPa for CO fractions of 1.5 vol.-% in the feed gas.

**Keywords:** Chemical vapour deposition, hard coatings, TiCN, CO

\* **Present address:** PLANSEE SE, A-6600 Reutte, Austria

## 1. Introduction

Indexable inserts are widely used in metal cutting applications like turning, milling, parting, and grooving. Cemented carbide is often used as substrate material, mainly containing tungsten carbide, cubic (Ti, Ta, Nb)-carbides and a cobalt binder phase [1, 2]. To enhance cost efficiency and productivity as well as process reliability, hard coatings are applied on these substrates using physical vapour deposition (PVD) or chemical vapour deposition (CVD) [3]. Especially for turning steel or nodular cast iron, highly wear resistant and well adherent coatings up to 25  $\mu\text{m}$  total thickness are needed. To meet these goals,  $\text{Al}_2\text{O}_3$  top layers on  $\text{TiC}_x\text{N}_{1-x}$  base layers, both grown by CVD, are frequently used [4-6].

TiN, TiC and  $\text{TiC}_x\text{N}_{1-x}$  are applied since decades as wear resistant coatings using the  $\text{TiCl}_4\text{-H}_2\text{-N}_2\text{-CH}_4$  CVD precursor system. This process is carried out at temperatures of 950-1050  $^\circ\text{C}$  and pressures of 50-1000 mbar [7, 8]. Due to the high deposition temperatures, decarburization of the cemented carbide substrate takes place, which leads to the undesired and brittle  $\eta$ -phase at the substrate/coating interface [9-11]. During the last two decades of the 20<sup>th</sup> century, the conventional high-temperature process was almost completely replaced by the medium-temperature CVD (MT-CVD) process, where  $\text{TiC}_x\text{N}_{1-x}$  is deposited from a  $\text{TiCl}_4\text{-CH}_3\text{CN-H}_2\text{-N}_2$  atmosphere at 800-900  $^\circ\text{C}$ . Using this MT-CVD process, decarburization of the substrate material can be almost completely avoided [12-14] and MT- $\text{TiC}_x\text{N}_{1-x}$  base layers provide the necessary mechanical support and toughness for  $\text{Al}_2\text{O}_3$  top layers.

$\text{TiC}_x\text{N}_{1-x}$  coatings grown by the MT-CVD process exhibit columnar structure perpendicular to the substrate surface and have a limited carbon to nitrogen atomic ratio of  $x = 0.5 - 0.7$  [12]. Many attempts to influence the structure and composition of the MT- $\text{TiC}_x\text{N}_{1-x}$  coatings using additions of  $\text{ZrCl}_3$ ,  $\text{BCl}_3$  or CO are documented [14-17], to refine the structure, to increase hardness and to improve the surface topography. Also ethane is used beside other hydrocarbons as additional carbon source to increase the carbon content of the MT- $\text{TiC}_x\text{N}_{1-x}$  coating in combination with a refinement of the columnar structure [18]. The addition of CO in the MT-CVD process of  $\text{TiC}_x\text{N}_{1-x}$  was investigated by Rупpi and Larsson. [17] in a broad range up to 8 vol.-% CO in the feed gas, resulting in oxygen contents between 2 and 14 at.-% in the coating. It was shown that higher amounts of CO lead to nano-grained structures with increasing hardness, but the cutting performance, in particular the crater wear resistance decreased. However, in [17] the range of oxygen contents below 2 at.-% was not investigated. Consequently, for this study, the addition of CO was set to lower feed gas fractions of up to 2.2 vol.-%, which seems to be beneficial in cutting, and its effect on microstructure and mechanical properties is investigated in detail.

## 2. Experimental details

The deposition runs were carried out in a SuCoTec SCT600 TH industrial-scale low-pressure CVD unit. All samples were placed in the centre of the batch, on the half radius and the outermost area of the tray, as described in [19]. Five different coatings have been synthesized with increasing amount of CO in the feed gas.  $\text{TiC}_x\text{N}_{1-x}$  was deposited on a  $0.3 \mu\text{m}$  TiN starting layer, using the MT-CVD process. The deposition was done by using  $\text{TiCl}_4\text{-CH}_3\text{CN-H}_2\text{-N}_2\text{-CO}$  at  $900 \text{ }^\circ\text{C}$  and a deposition pressure of 100 mbar. The basic feed gas composition for the  $\text{TiC}_x\text{N}_{1-x}$  layer was 22.9 vol.-%  $\text{N}_2$ , 1.9 vol.-%  $\text{TiCl}_4$ , 0.7 vol.-%  $\text{CH}_3\text{CN}$ , and  $\text{H}_2$  as balance, where CO fractions of 0.7, 1.0, 1.5 and 2.2 vol.-% were added. The total gas flow was 60 l/min and the leakage rate of the system was better than  $33 \times 10^{-6} \text{ mbar l s}^{-1}$ . The deposition time of 60 min for the TiN and 350 min for the  $\text{TiC}_x\text{N}_{1-x}$  layers was kept constant for all coatings. The coating thickness was determined by light optical microscopy on polished cross-sections of samples positioned at the three positions within the reactor mentioned and averaged. The analytical investigations were carried out on 12 wt.-% Co containing cemented carbide inserts with mixed carbides in SNUN 120412 geometry according to ISO 1832 ( $12.6 \times 12.6 \times 4.8 \text{ mm}^3$ ), positioned on the half radius of the tray. The used specimens were polished before the deposition process.

The characterization of the surface topography and fracture cross-sections was conducted using a Zeiss Ultra 55 plus scanning electron microscope (SEM). Roughness values were determined using a Nano Focus  $\mu\text{Surf}^{\text{®}}$  profilometer. The average surface roughness  $R_a$  of the coatings was determined using a measurement area of  $800 \times 800 \mu\text{m}$  on three different positions according to DIN EN ISO 4287.

The chemical composition of the  $\text{TiC}_x\text{N}_{1-x}$  based coatings was determined using a Jobin-Yvon Horiba JY10000 glow discharge optical emission spectroscope (GDOES). The quantitative determination of the oxygen content was carried out using a FEI standard-less electron probe micro-analysis (EPMA) system with an acceleration voltage of 10 kV. The qualitative oxygen depth distribution was determined using a time-of-flight secondary ion mass spectrometer (a ToF-SIMS<sup>5</sup> instrument from IONTOF). Depth profiling was performed in the high current bunched mode [21] using a pulsed high energy analysis beam from a liquid metal ion gun (particles:  $\text{Bi}_1^+$ ; acceleration energy: 25 keV; cycle time 50  $\mu\text{s}$ , resolution:  $128 \times 128$  pixel, field of view  $100 \times 100 \mu\text{m}^2$ ), alternating with a second beam for material erosion (particles:  $\text{Cs}^+$ ; acceleration energy: 2 keV, field of view  $300 \times 300 \mu\text{m}^2$ ).

Microstructural characterization was done using a Panalytical X'Pert Pro diffractometer and Cu  $K\alpha$  radiation. The determination of the phase composition was carried out in glancing angle X-ray diffraction (GAXRD) arrangement with  $2^\circ$  incidence angle. The texture coefficient  $TC$  was

calculated according to equation (1) from the intensities of diffraction lines,  $I(hkl)$ , measured in Bragg-Brentano geometry:

$$TC(hkl) = \frac{I(hkl)}{I_0(hkl)} \cdot \left[ \frac{1}{n} \sum_{n=1}^n \frac{I(hkl)}{I_0(hkl)} \right]^{-1} \quad (1)$$

As texture-free intensities,  $I_0(hkl)$ , the relative intensities from JCPDF #01-071-6059 were employed.  $n$  is the number of peaks considered. Ten reflections, i.e. (111), (200), (220), (311), (222), (400), (311), (420), (422), and (511) have been considered for calculation. The residual in-plane stress was determined using the  $\sin^2\Psi$  method with  $2\Theta = 61^\circ$ , corresponding to the (220) peak of  $TiC_xN_{1-x}$ , using an open Euler cradle on the Panalytical X'Pert Pro diffractometer and  $\sin^2\Psi$  values ranging from 0 to 0.9. For this calculation, an elastic modulus of 388 GPa and a Poisson ratio of 0.19 [22] were assumed.

Several samples were investigated by transmission electron microscopy (TEM) for a detailed structural analysis. To meet the deposited layer, a target preparation using a focused ion beam was the best choice. A DualBeam<sup>TM</sup> instrument by FEI of the type „Strata 400“, equipped with an Omniprobe micromanipulator of the type AutoProbe<sup>TM</sup> 300 was utilized for in-situ lift-out preparation out of a metallographic section [20]. The TEM was a Jeol 2010 FEF with in-column energy filter, working at 200 kV. The application of diffraction contrast at different angles between the primary electron beam and the sample surface controlled by the angle between electron beam and sample, enabled to visualize the lattice defects.

Indentation hardness and elastic modulus were measured with a CSM Nanoindenter, on polished coating surfaces using a Berkovich indenter and 30 mN maximum load. Loading and unloading rates were 60 mN/min with a residence time of 2 s at maximum load.  $2 \times 16$  indentations were performed on each sample. The indentation hardness and elastic modulus were calculated using the Oliver and Pharr method [23], where a Poisson ratio of 0.19 [22] was assumed, and averaged. The determination of the area function of the tip was done on fused silica using an elastic modulus of 72 GPa.

### 3. Results

#### 3.1. Deposition rate

The deposition time of 60 min for TiN and 350 min for  $\text{TiC}_x\text{N}_{1-x}$  resulted in a mean thickness of 0.3  $\mu\text{m}$  and  $4.8 \pm 0.6 \mu\text{m}$ , respectively. This corresponds to a deposition rate for  $\text{TiC}_x\text{N}_{1-x}$  of 0.82  $\mu\text{m}/\text{h}$ .

#### 3.2. Chemical composition

The chemical composition  $x$  of  $\text{TiC}_x\text{N}_{1-x}$  for the investigated coatings was determined using GDOES. The mean compositions obtained from the depth profile were  $x = 0.62, 0.61, 0.63, 0.63$  and  $0.62$  for coatings with CO additions of 0, 0.7, 1.0, 1.5 and 2.2 vol.-%, respectively, indicating that  $x$  is not significantly affected by CO addition. The quantitative oxygen content determined by EPMA is illustrated in Fig. 1. The  $\text{TiC}_x\text{N}_{1-x}$  base system without CO addition contained 0.1 at.-% oxygen which confirms the low leakage rate of the CVD plant. The addition of CO leads to higher oxygen contents in the coating. The correlation of the CO amount in the feed gas with the amount of the incorporated oxygen is almost linear for the investigated range. The highest amount of 2.2 at.-% oxygen in the coating was measured for a CO addition of 2.2 vol.-%.

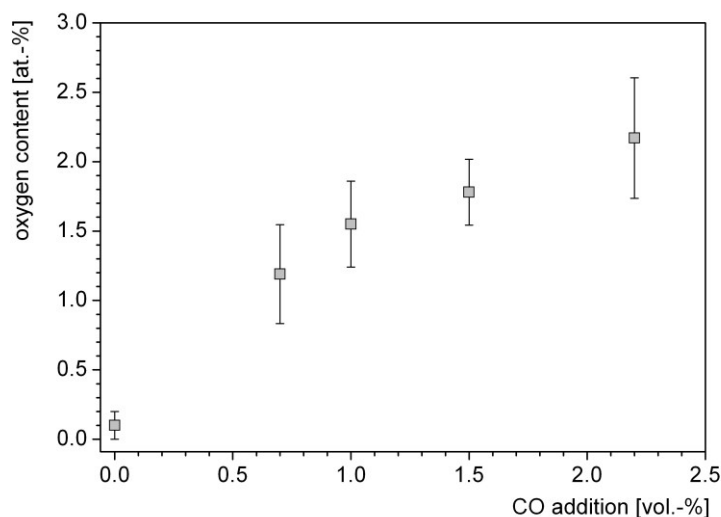


Fig. 22: Oxygen content of the  $\text{MT-TiC}_x\text{N}_{1-x}$  based coatings determined by EPMA as function of the CO fraction in the feed gas.

Qualitative measurements using ToF-SIMS were conducted to confirm the results of EPMA. The intensity of the oxygen signal versus sputter time is illustrated in Fig. 2. The achieved profiles indicate a homogeneous oxygen distribution over the investigated depth with an increase of oxygen towards the surface. The base system without CO addition showed the lowest intensity of the oxygen signal. Additions of 0.7, 1.0 and 1.5 vol.-% CO yielded signals which are about two orders of magnitude higher, with slight increases for increasing CO content. The addition of

2.2 vol.-% CO resulted in the highest intensity. Although due to lacking standards an accurate quantification of the ToF-SIMS results was not possible, the obtained trend corresponds well to the EPMA results. In the following sections, we will use the oxygen content determined by EPMA to distinguish between the different coatings.

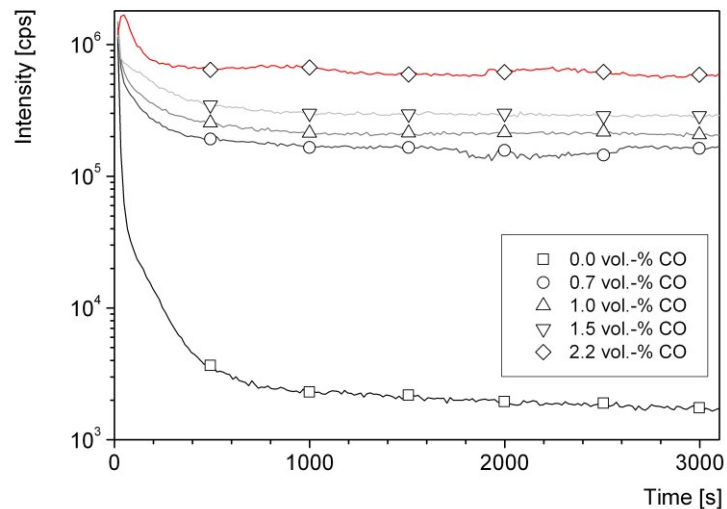


Fig. 23: ToF-SIMS depth profiles showing the oxygen signal versus sputter time of MT-TiC<sub>x</sub>N<sub>1-x</sub> based coatings grown with different CO fraction in the feed gas.

### 3.3. Topography and microstructure

The SEM investigation of the coating surface and crystal topography showed a smooth transition of the structural features with increasing oxygen content (Fig. 3). The flat crystal faces of the equiaxed grains of the TiC<sub>x</sub>N<sub>1-x</sub> base system change to a plate-like structure exhibiting distortions at the crystal surface due to the incorporation of oxygen. Additions of 1.2 to 1.8 at.-% O lead to comparable surface topography, while the remaining features of equiaxed grains gradually disappear. The grain size decreases with increasing oxygen amount as shown in Fig. 3. There, also fracture cross-sections of the synthesized coatings are shown, where a decrease in crystallite size with increasing oxygen content is visible especially close to the surface. A shift from columnar structure to the sub-micron-sized grains occurs for the coating grown with 2.2 at.-% O added.

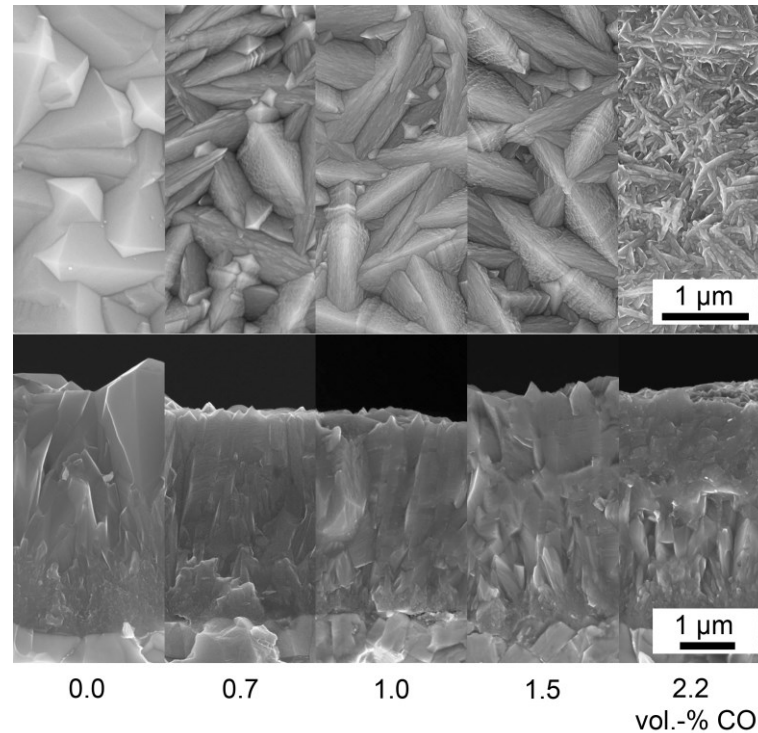


Fig. 24: SEM surface images (top row) and fracture cross-sections (bottom row) of the  $MT-TiC_xN_{1-x}$  based coatings as function of their oxygen content.

The values obtained for the average surface roughness  $R_a$  (see Fig. 4) agree well to the SEM surface images and fracture cross-sections (cf. Fig. 3). The surface roughness of the coatings is higher than that of the polished substrate surface for all coatings and decreases with increasing fraction of CO in the feed gas. For the interpretation of the roughness trend versus oxygen content it has to be considered that the coatings grown without CO addition and with 1.8 at.-% O are slightly thicker than the others (see Fig. 3). Thus, it can be assumed that the slightly higher roughness of these coatings is not an effect of CO addition, but related to their higher thickness due to the faceted columnar grains [12]. The general trend with increasing O incorporation can be correlated with the decreasing grain size of the crystals, which is comparable for the intermediate O contents of 1.2, 1.6 and 1.8 at.-%. The sub-micron grains in the range of the coating with the highest oxygen content showed the lowest surface roughness.



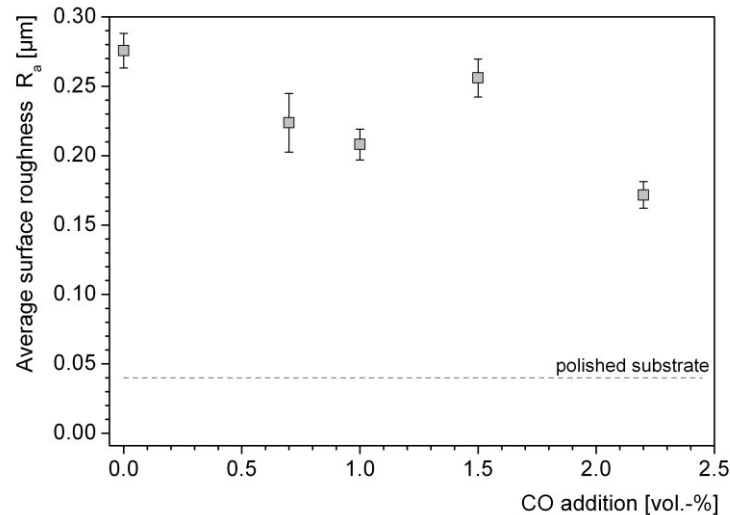


Fig. 25: Average surface roughness  $R_a$  of the as-deposited MT- $\text{TiC}_x\text{N}_{1-x}$  based coatings as function of their oxygen content .

According to the results of XRD, all coatings are single-phase containing the face-centred cubic  $\text{TiC}_{1-x}\text{N}_x$  solid solution. The calculation of texture coefficients  $TC$  [24] based on the measurements in Bragg-Brentano geometry showed a (110) preferred orientation of the  $\text{TiC}_x\text{N}_{1-x}$  base system without CO addition. The  $TC$  (220) values decrease with increasing oxygen content from 5.82 for the base system to 2.85 for the highest oxygen content of 2.2 at.-%. The calculated coefficients  $x$  in  $\text{TiC}_x\text{N}_{1-x}$  after stress correction using a series of sintered bulk  $\text{TiC}_x\text{N}_{1-x}$  calibration standards were in the range of  $0.57 \pm 0.02$ , which is only slightly lower than the values determined by GDOES. In agreement with the GDOES analysis, no significant effect of the CO fraction in the feed gas on  $x$  was obtained.

Detailed structural investigations by TEM indicate a grain size of a few  $\mu\text{m}$  in growth direction and lateral dimensions of  $\sim 0.5 \mu\text{m}$  for the  $\text{TiC}_x\text{N}_{1-x}$  base system (see Fig. 5(a)) and for low oxygen contents (see Fig. 5(b)), confirming the V-shaped growth of columnar grains [12]. The grains are characterized by a high density of homogeneously distributed dislocations. For an oxygen content of 1.2 at.-% in the coating, an increasing number of defects extended in the growth direction becomes visible (see Fig 5(b)). Beside the reduced grain size and high dislocation density observed for the sample with 2.2 at.-% O (see Fig 5(c)), a significant appearance of micro-twins was detected.

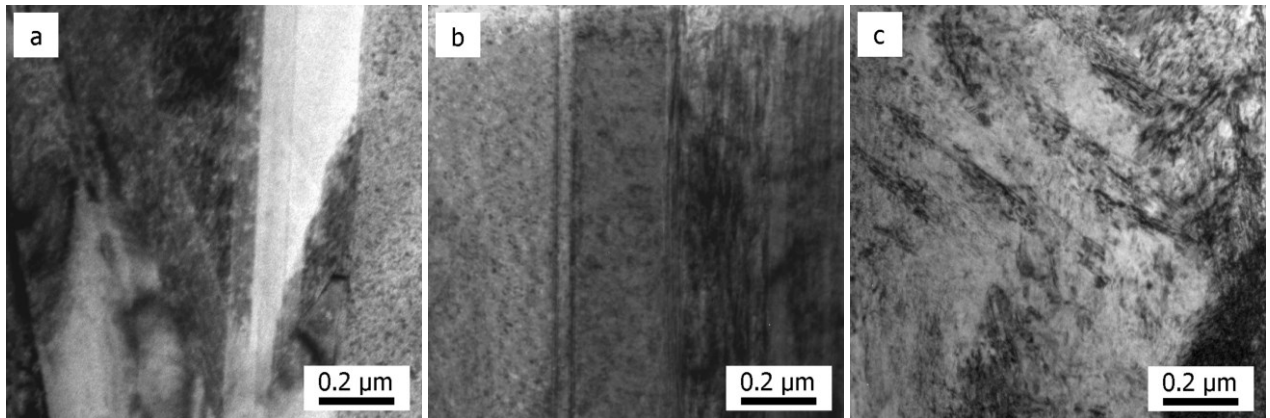


Fig. 5: TEM bright field cross-sections of MT- $\text{TiC}_x\text{N}_{1-x}$  based coatings without CO in the feed gas (a), with 1.2 at.-% O (b) and 2.2 at.-% O (c).

The features observed in the sample with an oxygen content of 1.2 at.-% have been investigated in more detail by high resolution imaging and fast Fourier transformation (see Fig. 6). The extended defects consist of an area with scrambled order of stacking, which could not be resolved in every crystal lattice plane. The orientation of the  $\text{TiC}_x\text{N}_{1-x}$  crystals at both sides of the boundary is equal in the case between the areas “b” and “c”, marked in Fig 6(a), and corresponds to a twin orientation with a (111) twinning plane between “d” and “e”. Thus, the increasing number of defects observed in Fig. 5 has to be attributed to a rising density of twin boundaries, where their formation is triggered by the incorporation of oxygen due to the increasing CO fraction in the feed gas.

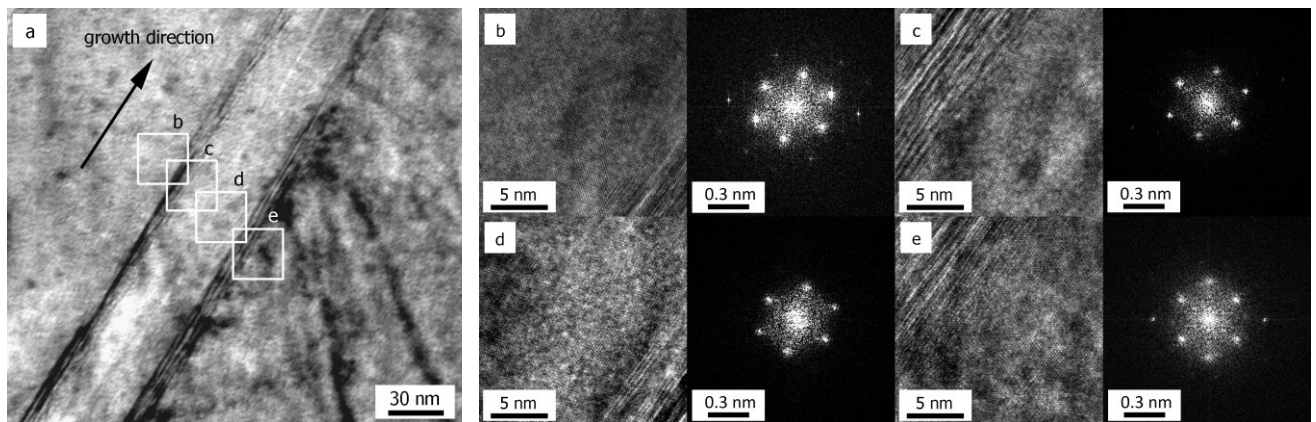


Fig. 6: MT- $\text{TiC}_x\text{N}_{1-x}$  based coating with 1.2 at.-% O: (a) High-resolution TEM bright-field cross-section and (b)-(e) selected cross-section areas and selected area diffraction patterns close to the extended defects visible in (a).

The distribution of dislocations in all  $\text{TiC}_x\text{N}_{1-x}$  grains is homogeneous, as demonstrated in Fig. 7, where one location of the sample is tilted in a way that different grains were in the diffraction position near the two beam case, enabling to recognize dislocations fulfilling the  $\mathbf{g} \cdot \mathbf{b}$  criterion.

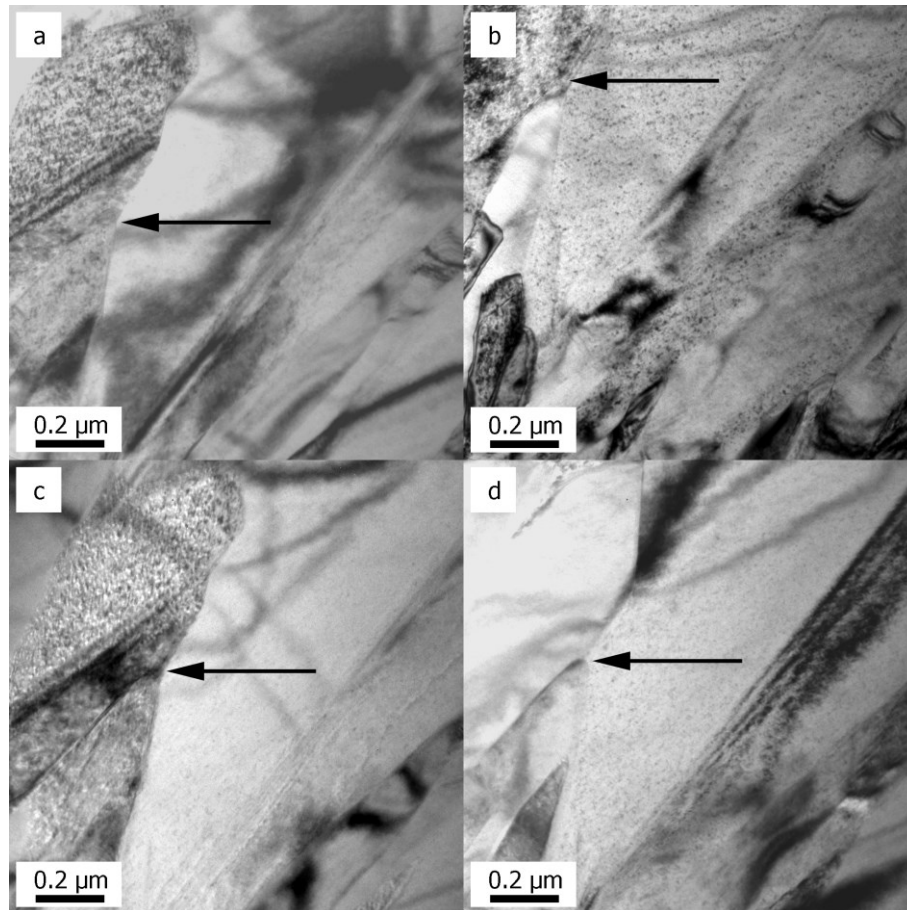


Fig. 7: TEM bright-field cross-sections of a MT-TiC<sub>x</sub>N<sub>1-x</sub> based coating with 2.2 at.-% O using 1° (a), -7° (b), 0° (c) and 8° (d) tilt angle showing the homogenous distribution of dislocations. The arrow marks an identical position.

### 3.4. Mechanical properties

The residual stress measurements using the  $\sin^2\Psi$  method showed the highest value of tensile stress for the TiC<sub>x</sub>N<sub>1-x</sub> base system deposited without CO addition (see Fig 8). The residual stresses decrease with increasing oxygen content reaching a minimum of 200 MPa for fractions of 1.6 at.-% O. Higher oxygen contents lead to an increase of the residual stress, most probably due to the decreasing grain size (see Fig 3) and the higher number of twin boundaries (see Fig. 5).

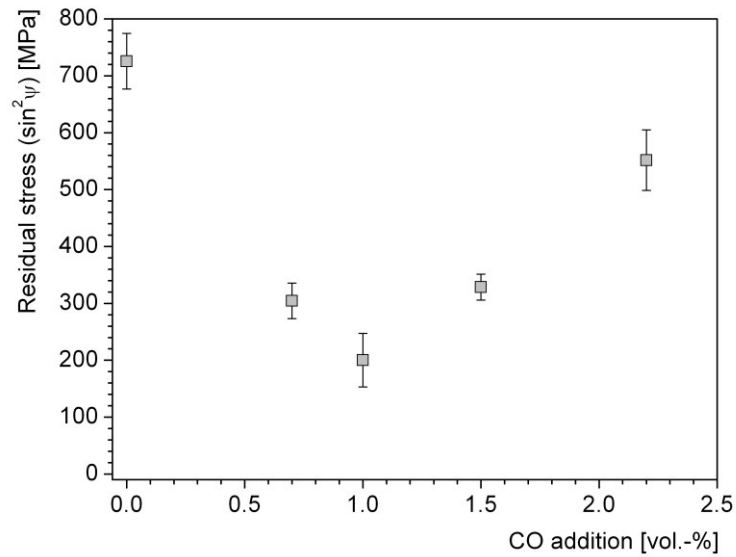


Fig. 8: Residual stress of the as-deposited MT-TiC<sub>x</sub>N<sub>1-x</sub> based coatings determined by the sin<sup>2</sup>ψ method as function of their oxygen content.

The determined indentation hardness and elastic modulus of TiC<sub>x</sub>N<sub>1-x</sub> coatings as a function of the oxygen incorporated in the coating is shown in Fig. 9. The indentation hardness of the TiC<sub>x</sub>N<sub>1-x</sub> base system of 22.9±0.7 GPa corresponds well to literature [25, 26], while the indentation modulus is higher than the reported values of about 400 GPa [27]. The increasing oxygen incorporation due to the higher CO fractions in the feed gas results in an increase in hardness with a maximum of 32.4±1.5 GPa for 1.8 at.-% O. The indentation modulus showed a maximum for moderate fractions of 1.2 to 1.8 at.-% O in the coating.

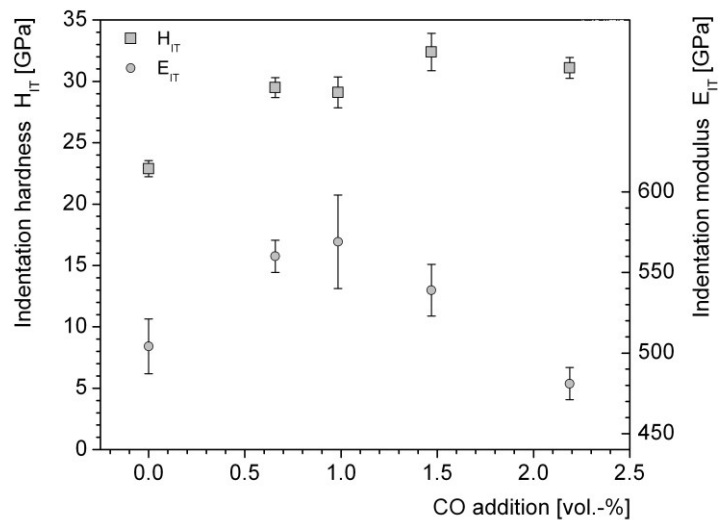


Fig. 9: Indentation hardness and elastic modulus of the MT-TiC<sub>x</sub>N<sub>1-x</sub> based coatings as function of their oxygen content.

## 4. Discussion

The presented results show a transition of surface topography, microstructure and mechanical properties of  $\text{TiC}_x\text{N}_{1-x}$  coatings grown by MT-CVD with increasing fractions of oxygen added. The transition of the equiaxed grains typical for the  $\text{TiC}_x\text{N}_{1-x}$  base system without oxygen addition [12] to the plate-like structure is attributed to the incorporation of oxygen (see Fig. 3), which leads to higher twinning tendency, in particular to formation of (111) twinning planes in growth direction. No evidence for oxide phases, e.g.  $\text{TiO}_2$ , was found, which leads to the conclusion that the oxygen is incorporated into the  $\text{TiC}_x\text{N}_{1-x}$  phase. However, this incorporation did not influence the carbon to nitrogen ratio and the lattice parameter of the  $\text{TiC}_x\text{N}_{1-x}$  phase. The higher density of twin boundaries observed for increasing oxygen contents thus leads to the conclusion that the oxygen is located at these defects. These stacks of parallel (111) twinning planes result in an elongation of the grains in the direction perpendicular to the twinning plane, and are thus assumed to be responsible for the observed plate-like grain structure (see Fig. 3). While low oxygen contents seem to be accommodated at the twin boundaries, a significant decrease of the grain size was observed for the highest oxygen content studied (see Fig. 5(c)), resulting in a distortion of the columnar structure and a transition to an equiaxed micro-twinned structure. This might be attributed to hindered crystal growth by the rising amount of oxygen impurities, as described by Barna and Adamik [28]. The higher density of grain and twin boundaries is associated with an increase of hardness, following the Hall-Petch mechanism [29]. The lower in-plane residual stress level of the coatings might be explained by the (111) twinning planes in growth direction, which reduce tensile stresses.

In comparison to the previous work from Rupp and Larsson [17], several differences could be found. Although a lower content of CO in the feed gas was used within this work, similar changes in crystal morphology were observed. The change from equiaxed to plate-like structure and finally sub-micron grains, which was reported in [17] for feed gas fractions of 4 and 6 vol.-% CO, respectively, was found in this work at significant lower fractions of 0.7 and 2.2 vol.-% CO. This can be attributed to the ~40 vol.-% lower total gas flow as well as the lower total amount of reactive gases  $\text{TiCl}_4$  and  $\text{CH}_3\text{CN}$  used in this study. Due to a lack of information onto reactor volume and gas preheating system in [17], a detailed discussion about gas velocity and residence time of the reactive species is unfeasible. However, the differences in total and reactive gas flow also explain the lower deposition rate of  $0.82 \mu\text{m/h}$  in this work, compared to  $1.3 - 1.4 \mu\text{m/h}$  reported in [17] for low CO amounts. In contrast to [17], no significant effect of CO addition on the growth rate could be observed, although a difference in morphology was found. However, it should be noted that higher CO fractions might affect the growth rate as well. Due to the different deposition conditions, also the preferred orientation differs from the one observed in [17], where a preferred (211)

orientation was found, which is in contrast to the (110) orientation observed within this work. In this investigation, for the  $\text{TiC}_x\text{N}_{1-x}$  base system with (110) orientation no twins could be observed. In contrast, the (211) orientation found by Rупpi and Larsson [17] shows these twins already in the  $\text{TiC}_x\text{N}_{1-x}$  base system without CO addition. Nevertheless, our hardness values agree well to those reported in [17, 30].

## 5. Summary and conclusions

The influence of the CO addition to the feed gas during the industrial-scale low-pressure chemical vapour deposition of  $\text{TiC}_x\text{N}_{1-x}$  coatings was investigated with the goal to improve their microstructure, surface roughness and mechanical properties. The oxygen content of the coatings shows a nearly linear correlation to the CO fraction provided by the feed gas. The microstructure changes with increasing CO fraction from equiaxed grains with plane faces via smaller plate-like grains exhibiting distortions and finally to a structure with sub-micron grains. The incorporated oxygen leads to grain refinement in combination with an increase of dislocation density and twins. It can be concluded that these twin boundaries accommodate the incorporated oxygen. The minimum of residual tensile stress was determined for an oxygen content of 1.6 at.-% in the coating, which showed an increased indentation hardness of  $29.1 \pm 1.3$  GPa. These improved material properties in combination with the low residual stress level seem to be promising for cutting applications.

## Acknowledgements

This work was supported by the Austrian Federal Government (in particular from the Bundesministerium für Verkehr, Innovation und Technologie and the Bundesministerium für Wirtschaft, Familie und Jugend) and the Styrian Provincial Government, represented by Österreichische Forschungsförderungsgesellschaft mbH and by Steirische Wirtschaftsförderungsgesellschaft mbH, within the research activities of the K2 Competence Centre on “Integrated Research in Materials, Processing and Product Engineering”, operated by the Materials Center Leoben Forschung GmbH in the framework of the Austrian COMET Competence Centre Programme.

## References

- [1] W. Schedler, Hartmetall für den Praktiker, Plansee TIZIT, Düsseldorf, 1988.
- [2] W. Lengauer, K. Dreyer, J. Alloy Compd. 338/1-2 (2002) 194.
- [3] H.G. Prengel, W.R. Pfouts, A.T. Santhanam, Surf. Coat. Technol. 102 (1998) 183.
- [4] S. Ruppi, J. Phys. IV 11/Pr3 (2001) 847.
- [5] B. Mills, J. Mater. Proc. Technol. 56/1-4 (1996) 16.
- [6] D.T. Quinto, Int. J. Refract. Met. Hard Mater. 14/1-3 (1996) 7.
- [7] W. Schintlmeister, O. Pacher, Metall 28/7 (1974) 690.
- [8] D.J. Cheng, W.P. Sun, M.H. Hon, Thin Solid Films 146/1 (1987) 45.
- [9] V.K. Sarin, J.N. Lindstrom, J. Electrochem. Soc. 126/7 (1979) 1281.
- [10] J. Skogsmo, H. Norden, Int. J. Refract. Met. Hard Mater. 11/1 (1992) 49.
- [11] S. Vuorinen, R.H. Hoel, Thin Solid Films 232/1 (1993) 73.
- [12] A. Larsson, S. Ruppi, Thin Solid Films 402/1-2 (2002) 203.
- [13] R. Bonetti, H. Wahl, in: J. Bloem, G. Verspui, L.R. Wolff (Eds.), Euro CVD IV, Eindhoven, Netherlands, 1983, p. 510.
- [14] S. Kudapa, K. Narasimhan, P. Boppana, W.C. Russell, Surf. Coat. Technol. 121 (1999) 259.
- [15] H. Holzschuh, Thin Solid Films 469-470 (2004) 92.
- [16] H. Holzschuh, J. Phys. IV 10/P2 (2000) 49.
- [17] S. Ruppi, A. Larsson, J. Vac. Sci. Technol. A 21/1 (2003) 66.
- [18] J. Wanatabe, Y. Sone, EP1897970A1 (2008)
- [19] C. Czettl, C. Mitterer, C. Michotte, M. Penoy, M. Kathrein, in: L.S. Sigl, P. Rödhammer, H. Wildner (Eds.), Plansee Seminar 2009, Plansee Group, Reutte, Austria, 2009, p. HM71.1
- [20] U. Mühle, S. Jansen, S. Leinert, D. Breuer, Prakt. Metallogr. 43 (2006) 306.
- [21] E. Niehuis, T. Grehl, in: A. Benninghoven (Ed.), 12<sup>th</sup> Int. Conf. on Sec. Ion Mass Spect., Brussels, 2000, p. 49.
- [22] H.O. Pierson, Handbook of Chemical Vapor Deposition, Noyes Publications, New Jersey, 1999.
- [23] W.C. Oliver, G.M. Pharr, J. Mater. Res. 7/6 (1992) 1564.
- [24] M.H. Müller, W.P. Chernock, P.A. Beck, Trans. Met. Soc. AIME 212 (1958) 39.
- [25] H. Chien, M.C. Gao, H.M. Miller, G.S. Rohrer, Z. Ban, P. Prichard, Y. Liu, Int. J. Refract. Met. Hard Mater. 27 (2009) 458.
- [26] W. Lengauer, S. Binder, K. Aigner, P. Ettmayer, A. Guillou, A. Debuigne, G. Groboth, J. Alloy Compd. 217 (1995) 137.
- [27] C. Kral, W. Lengauer, D. Rafaja, P. Ettmayer, J. Alloy Compd. 265/1-2 (1998) 215.
- [28] P.B. Barna, M. Adamik, Thin Solid Films 317 (1998) 27.
- [29] G. Gottstein, Physikalisch Grundlagen der Materialkunde, Springer, Berlin-Heidelberg-New York, 1998.
- [30] J. Wagner, C. Mitterer, M. Penoy, C. Michotte, W. Wallgram, M. Kathrein, in: G. Kneringer, P. Rödhammer, H. Wildner (Eds.), Plansee Seminar 2005, Plansee Group, Reutte, Austria, 2005, p. 917.

## **Publication IV**

### **C<sub>2</sub>H<sub>6</sub> as precursor for low pressure chemical vapor deposition of TiCNB hard coatings**

C. Czettl, C. Mitterer, M. Penoy, C. Michotte, M. Kathrein

Surface and Coatings Technology 215/0 (2013) 127



# **C<sub>2</sub>H<sub>6</sub> as precursor for low pressure chemical vapour deposition of TiCNB hard coatings**

C. Czettl<sup>1,4</sup>, C. Mitterer<sup>2</sup>, M. Penoy<sup>3</sup>, C. Michotte<sup>3</sup>, M. Kathrein<sup>4,\*</sup>

<sup>1</sup> Materials Center Leoben Forschung GmbH, Roseggerstraße 12, A-8700 Leoben, Austria

<sup>2</sup> Department of Physical Metallurgy and Materials Testing, Montanuniversität, Franz-Josef-Straße 18, A-8700 Leoben, Austria

<sup>3</sup> CERATIZIT Luxembourg S. à. r. l., Route de Holzem, L-8201 Mamer, Luxembourg

<sup>4</sup> CERATIZIT Austria GmbH, A-6600 Reutte, Austria

## **Abstract**

Multilayered TiN/TiCN/Al<sub>2</sub>O<sub>3</sub> hard coatings grown by chemical vapor deposition (CVD) are used for wear protection of cemented carbide inserts, applied for example in turning, milling, parting and grooving operations. Within this work, the TiC<sub>x</sub>N<sub>1-x</sub> coatings have been further optimized with respect to their structure and mechanical properties by addition of BCl<sub>3</sub> to the feed gas. The characterization of the coatings was done by light optical microscopy, glow discharge optical emission spectroscopy, X-ray diffraction, scanning and transmission electron microscopy, surface roughness measurements, nanoindentation and cutting tests. The increasing amount of BCl<sub>3</sub> in the feed gas resulted in boron contents of up to 3.96 at.% in the coating, where careful adjustment of the BCl<sub>3</sub> supply is necessary. By incorporation of boron, an increase of coating hardness due to an increasing density of structural defects was obtained. The grain size decreases for the highest boron content, while the structure changes from equiaxed grains to a fine lamellar structure. In milling and turning tests, an increased lifetime was obtained for coatings with low amounts of boron, compared to the TiC<sub>x</sub>N<sub>1-x</sub> reference.

## **Keywords**

Chemical vapour deposition, hard coatings, TiCNB, C<sub>2</sub>H<sub>6</sub>

**\* Present address:**

PLANSEE SE, A-6600 Reutte, Austria

## 1. Introduction

The demand for tools with high reliability and durability is well known since the early ages of mankind. This is especially valid for metal cutting applications, where the invention of high speed steels and cemented carbides enhanced the performance of the tools by orders of magnitude. The application of wear resistant coatings consisting of hard materials, starting in the late 1960ies, led to a further tremendous improvement regarding to their durability [1]. When coated cemented carbides are considered, mainly two vapour deposition methods are dominant, i.e. chemical vapour deposition (CVD) and physical vapour deposition (PVD). CVD is applied, when high coating thickness up to 25  $\mu\text{m}$  and  $\text{Al}_2\text{O}_3$  coatings for thermal insulation and hot hardness are needed. PVD is dominant for highly interrupted cutting conditions like milling, threading and drilling operations [2]. The main fraction of CVD coatings consist of TiN, TiC and  $\text{TiC}_x\text{N}_{1-x}$  coatings, commonly in combination with  $\text{Al}_2\text{O}_3$  where bonding layers containing small amounts of oxygen or boron are used to stabilize the desired oxide polymorph and to affect the texture of the oxide [3, 4]. To avoid decarburisation and formation of the brittle  $\eta$ -phase [3], the medium temperature titanium carbonitride (MT-TiCN) process using  $\text{CH}_3\text{CN}$  instead of  $\text{CH}_4$  as carbon feeding precursor is used for the base layer, which allows deposition temperatures below 950  $^\circ\text{C}$  [5, 6]. Besides the variation of deposition parameters, dopants are used to influence the structure and mechanical properties of the coatings. The most common dopants of TiC,  $\text{TiC}_x\text{N}_{1-x}$  and TiN are  $\text{BCl}_3$ ,  $\text{AlCl}_3$ ,  $\text{HfCl}_4$ ,  $\text{ZrCl}_4$  as well as CO and  $\text{C}_2\text{H}_6$  [7-17]. The mentioned chlorides except  $\text{BCl}_3$  can be easily generated from their metals by in situ chlorination using HCl.  $\text{BCl}_3$  is gaseous at room temperature at ambient pressure and can be dosed via mass flow controllers like CO and  $\text{C}_2\text{H}_6$ . Because of its high diffusivity at temperatures above 900  $^\circ\text{C}$ ,  $\text{BCl}_3$  has to be used very carefully. Its interaction with cemented carbides, where hard and brittle W-Co-B phases like the  $\eta$ -phase, can be formed, was earlier used to increase the wear resistance of cemented carbides by diffusion methods [18], but is unwanted in state of the art CVD hard coatings due to their brittleness [19, 20]. Taking these limitations into account and choosing carefully the deposition parameters,  $\text{BCl}_3$  can be a very interesting precursor for wear resistant coatings without contamination of the substrate material, as already shown for  $\text{TiB}_2$  deposition via CVD [21]. Because of the enhanced oxidation resistance of Ti based coatings when small amounts of boron are incorporated [22], B addition via  $\text{BCl}_3$  seems to be promising. Thus, the Ti-N-B system was investigated in a wide range of deposition temperatures from 850 to 1500  $^\circ\text{C}$  by several authors [11, 13, 20, 23, 24]. The  $\text{TiC}_x\text{N}_y\text{B}_{1-(x+y)}$  system, in particular, was investigated by Holzschuh [12, 19] using  $\text{CH}_4$  and  $\text{CH}_3\text{CN}$  as carbon feeding gas, where high temperatures are needed for  $\text{CH}_4$  dissociation and the carbon-to-nitrogen ratio is limited for  $\text{CH}_3\text{CN}$ , respectively. The limitations with both precursor gases can be explained by their chemical bonding and reaction characteristics. This work shows the feasibility to deposit

TiC<sub>x</sub>N<sub>y</sub>B<sub>1-(x+y)</sub> coatings using C<sub>2</sub>H<sub>6</sub> as carbon feeding precursor at low temperatures of 920 °C, to minimize substrate contamination.

## 2. Experimental details

The deposition runs were carried out in a SuCoTec SCT600 TH industrial-scale low-pressure CVD unit. All samples for analytical investigations were placed in the centre of the batch, on the half radius of the tray, as described in [25]. Four different coatings have been synthesized with increasing amount of BCl<sub>3</sub> in the feed gas. The TiC<sub>x</sub>N<sub>y</sub>B<sub>1-(x+y)</sub> layers were deposited on a 0.4 μm thick TiN starting layer. The depositions were done using the TiCl<sub>4</sub>-C<sub>2</sub>H<sub>6</sub>-H<sub>2</sub>-N<sub>2</sub>-BCl<sub>3</sub> system at 920 °C and a deposition pressure of 1.6×10<sup>4</sup> Pa. The basic feed gas composition for the TiC<sub>x</sub>N<sub>y</sub>B<sub>1-(x+y)</sub> layer was 23.3 vol.% N<sub>2</sub>, 1.2 vol.% TiCl<sub>4</sub>, 1.5 vol.% C<sub>2</sub>H<sub>6</sub>, and H<sub>2</sub> as balance, where BCl<sub>3</sub> fractions of 0, 150, 380 and 1070 ppm were added. The total gas flow was 65.4 l/min and the leakage rate of the system was better than 33 × 10<sup>-6</sup> mbar l s<sup>-1</sup>. The deposition time of 60 min for the TiN and 470 min for the TiC<sub>x</sub>N<sub>y</sub>B<sub>1-(x+y)</sub> layers was kept constant for all coatings. The coating thickness was determined by light optical microscopy on polished cross-sections of three positions within the reactor, i.e. centre, half radius and outermost area of the tray. The mass gain was measured using a precision balance on 33 inserts out of a full batch. The analytical investigations were carried out on coatings deposited on WC-Co cemented carbide inserts with 12 wt.% Co, 4 wt.% TiC and 8 wt.% (Ta,Nb)C in SNUN 120412 geometry according to ISO 1832 (12.6 × 12.6 × 4.8 mm<sup>3</sup>). The used specimens were polished before the deposition process.

The characterization of the surface topography and fracture cross-sections was conducted using a Zeiss Ultra 55 plus scanning electron microscope (SEM). Roughness values were determined using a Leica DCM3D profilometer at 100× magnification in confocal mode. The average surface roughness S<sub>a</sub> of the coatings was determined using a measurement area of 127 × 96 μm on three different positions according to DIN EN ISO 25178.

The chemical composition of the TiC<sub>x</sub>N<sub>y</sub>B<sub>1-(x+y)</sub> coatings was determined using a Jobin-Yvon Horiba JY10000 glow discharge optical emission spectroscopy (GDOES). The calibration was done on isostatic hot pressed reference materials, made of powder mixtures with varying compositions. Microstructural characterization was done by X-ray diffraction using a Panalytical X'Pert Pro diffractometer and Cu Kα radiation. The determination of the phase composition was carried out in locked coupled mode. The texture coefficient *TC* was calculated according to equation (1) from the intensities of diffraction lines, *I*(hkl):

$$TC(hkl) = \frac{I(hkl)}{I_0(hkl)} \cdot \left[ \frac{1}{n} \sum_{n=1}^n \frac{I(hkl)}{I_0(hkl)} \right]^{-1} \quad (1)$$

As texture-free intensities,  $I_0(hkl)$ , the relative intensities from JCPDF #01-071-6059 were employed.  $n$  is the number of peaks considered. Ten reflections, i.e. (111), (200), (220), (311), (222), (400), (311), (420), (422), and (511) have been considered for calculation. The residual in-plane stress was determined using the  $\sin^2\Psi$  method with  $2\Theta = 61^\circ$ , corresponding to the (220) peak of  $\text{TiC}_x\text{N}_{1-x}$ , using an open Euler cradle on the Panalytical X'Pert Pro diffractometer and  $\sin^2\Psi$  values ranging from 0 to 0.9. For this calculation, an elastic modulus of 388 GPa and a Poisson ratio of 0.19 [26] were assumed.

Several samples were investigated by transmission electron microscopy (TEM) for a detailed structural analysis. For exact preparation of the deposited layer, target preparation using a focused ion beam was done. A FEI DualBeam™ instrument of type Strata 400, equipped with an Omniprobe AutoProbe™ 300 micromanipulator, was utilized for in-situ lift-out preparation out of a metallographic section [27]. The TEM was a Jeol 2010 FEF with in-column energy filter, working at 200 kV.

Indentation hardness and elastic modulus were measured on polished coating surfaces using a CSM Instruments Nanoindenter with Berkovich indenter and 30 mN maximum load. Loading and unloading rates were 60 mN/min with a residence time of 1 s at maximum load. 20 indentations were performed on each sample. The indentation hardness and elastic modulus were calculated using the Oliver and Pharr method [28], where a Poisson ratio of 0.19 [26] was assumed, and averaged. The determination of the area function of the tip was done on fused silica using an elastic modulus of 72 GPa.

For turning tests, P25 WC-Co substrates with 7 wt.% Co, 2.6 wt.% TiC, 5.5 wt.% (Ta,Nb)C and Co-enriched surface zone in CNMG 120412-EN TRM geometry were used. The turning test was a segment turning test, which is a combination of face- and longitudinal turning operation, on DIN 1.7225 (42CrMo4) low-alloyed steel with cutting speed  $v_c = 220$  m/min, feed rate  $f = 0.4$  mm and cooling lubricant. Each segment consists of six cuts, i.e. three face and three longitudinal cuts with a varied depth of cut  $a_p = 3, 2$  and 1 mm. The milling tests were carried out with WC-Co substrates with 10 wt.% Co in RPHX 1204MO-EN M31 geometry. The milling test was a single edge milling test with cutting speed  $v_c = 220$  m/min, feed rate per tooth  $f_z = 0.4$  mm, depth of cut  $a_p = 2.5$  mm and contact width  $a_e = 40$  mm on DIN 1.4021 (X20Cr13) martensitic steel in dry cutting operation.

### 3. Results

#### 3.1. Deposition rate

The deposition time of 60 min for TiN and 470 min for  $\text{TiC}_x\text{N}_y\text{B}_{1-(x+y)}$  resulted in a mean thickness of  $0.4\pm 0.2\ \mu\text{m}$  and  $6.0\pm 0.2\ \mu\text{m}$ , respectively. This corresponds to a deposition rate for  $\text{TiC}_x\text{N}_y\text{B}_{1-(x+y)}$  of  $0.77\ \mu\text{m}/\text{h}$ . The mass gain, which gives a good overview of the batch homogeneity visualized by the error bars in Fig. 1, indicates that the  $\text{BCl}_3$  in the feed gas does not affect the deposition rate.

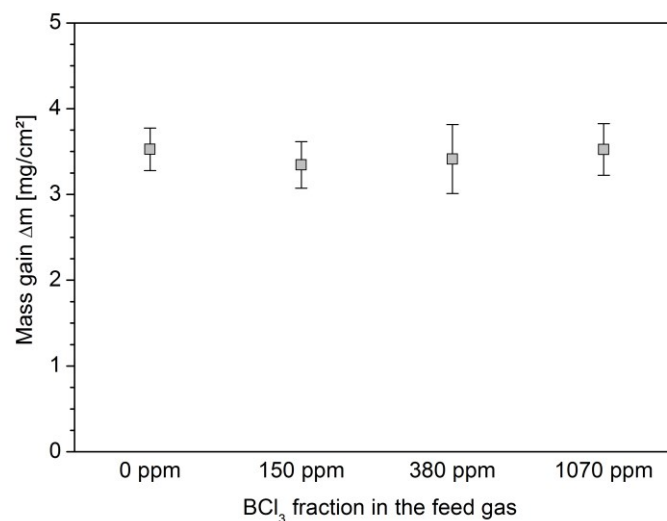


Fig. 1: Mass gain of the coatings versus  $\text{BCl}_3$  fraction in the feed gas.

#### 3.2. Chemical composition

The chemical composition of the  $\text{TiC}_x\text{N}_y\text{B}_{1-(x+y)}$  layers was determined using GDOES. The obtained mean compositions given in Table 1 are calculated from the depth profiles, which are exemplarily shown for B in Fig. 2. The fraction of titanium is very close to stoichiometry, which is expected for CVD coatings at the deposition temperatures used. The carbon content of the coatings with additions of  $\text{BCl}_3$  is higher compared to the  $\text{TiC}_x\text{N}_{1-x}$  reference coating and decreases with increasing amount of  $\text{BCl}_3$  in the feed gas. Fig. 2 indicates that the boron content determined shows a nearly exponential dependence on the  $\text{BCl}_3$  fraction in the feed gas. The amount of 0.01 at.% B of the boron-free  $\text{TiC}_x\text{N}_{1-x}$  reference coating deposited without  $\text{BCl}_3$  addition, which is also similar in the substrate material, can be interpreted as offset of the calibration line; contamination was excluded by further experiments. Therefore, the nomenclature <0.01 at.% B will be used for the  $\text{TiC}_x\text{N}_{1-x}$  reference system. Essentially, coatings with two different composition ranges can be distinguished, i.e. low boron- ( $\leq 0.12$  at.% B) and high boron contents (i.e. 3.96 at.% B).

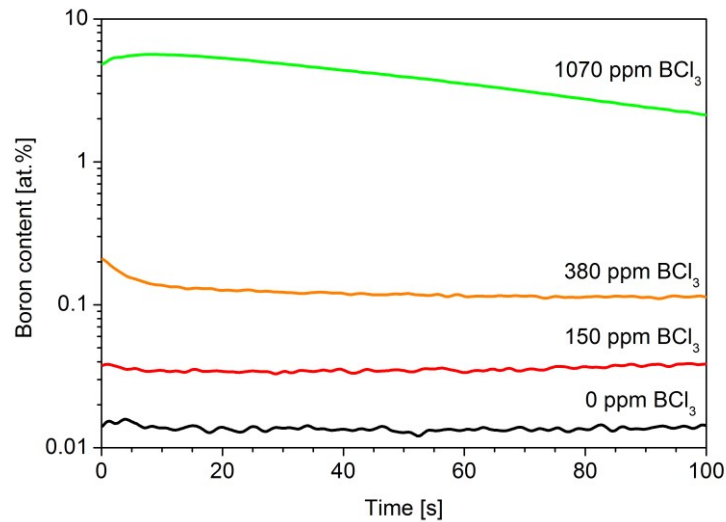


Fig. 2: GDOES depth profiles of the boron content in the deposited coatings using different BCl<sub>3</sub> fractions in the feed gas.

### 3.3. Topography and microstructure

The surface morphology and fracture cross-section of the coatings were investigated using SEM. Fig. 3 shows the equiaxed columnar grains of the TiC<sub>x</sub>N<sub>1-x</sub> reference system. In contrast, an increasing number of defects formed for increasing boron contents, till the structure transforms into a lamellar type for the highest amount of 3.96 at.% B. For this boron content, the columnar structure is completely suppressed.

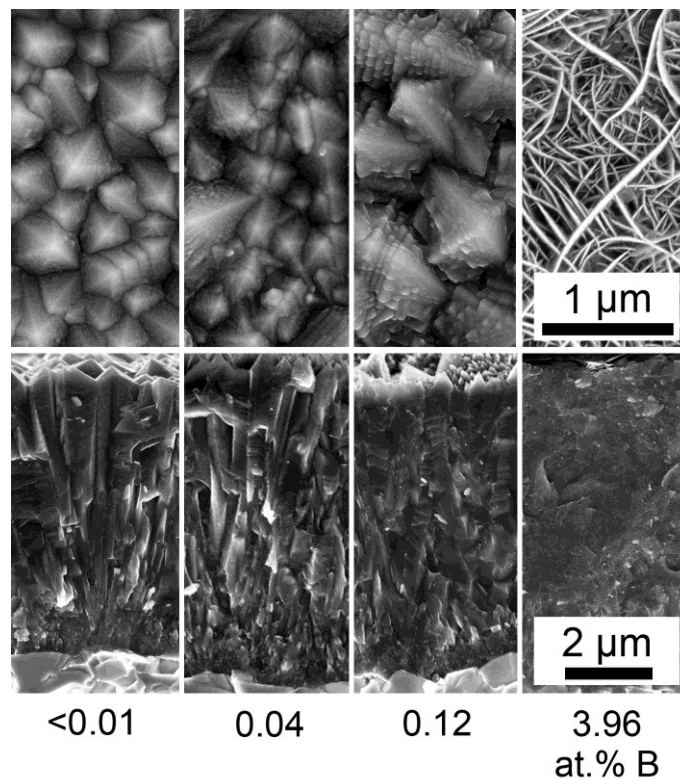


Fig. 3: SEM surface images and fracture cross-sections of the deposited coatings with different boron contents.

The two-dimensional arithmetic surface roughness  $S_a$  illustrated in Fig. 4 increases from  $43.3 \pm 0.7$  nm for the  $\text{TiC}_x\text{N}_{1-x}$  reference coating to  $86.9 \pm 1.5$  nm and  $95.0 \pm 2.1$  nm for 0.04 and 0.12 at.% B, respectively, and decreases again to  $31.2 \pm 1.3$  nm when 3.96 at.% B are incorporated. This trend is in good agreement with the evaluation of the SEM fracture cross-sections, where sharp tips of the crystal facettes can be seen for 0.04 and 0.12 at.% B.

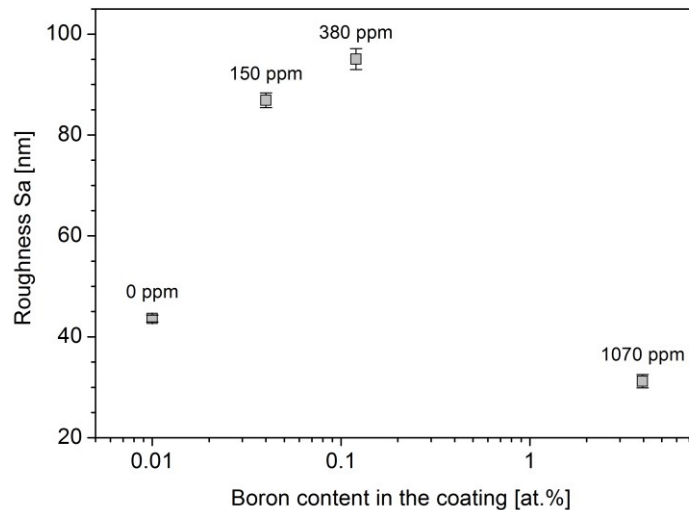


Fig. 4: Surface roughness  $S_a$  of the coatings with  $\text{BCl}_3$  fractions of 0, 150, 380 and 1070 ppm, resulting in boron contents in the coating of <0.01, 0.04, 0.12 and 3.96 at.%.

The structure and phase composition of the coatings was determined using XRD. Fig. 5 shows the diffraction patterns of the synthesized coatings with the dominating (220)  $\text{TiC}_x\text{N}_{1-x}$  peak (based on a solid solution between TiC and TiN), which reaches the highest intensity. The TC(220) of 5.32 for the  $\text{TiC}_x\text{N}_{1-x}$  reference coating decreases only slightly to 4.00 for coatings with the highest boron content. The reference coating also shows traces of the  $\text{Co}_6\text{W}_6\text{C}$   $\eta$ -phase, which could not be found for the other coatings. For the highest amount of boron in the coating, a peak broadening of the (220) peak, a low fraction of  $\text{TiB}_2$  and traces of the  $\eta$ -phase  $\text{CoW}_2\text{B}_2$  can be identified. In contrast, the low B contents obtained for 150 and 380 ppm  $\text{BCl}_3$  in the feed gas can be assumed to be incorporated in the  $\text{TiC}_x\text{N}_{1-x}$  solid solution [11].

Fig. 6 shows TEM bright-field images of the  $\text{TiC}_x\text{N}_{1-x}$  reference coating as well as the coatings with 0.04 and 3.96 at.% B, respectively. The growth direction of all three coatings is from bottom right to top left, as indicated in Fig. 6. A high number of defects like voids and dislocations can be identified in all coatings. For the  $\text{TiC}_x\text{N}_{1-x}$  reference system and the coating with 0.04 at.% B, grains can be identified which appear bright and seem to be essentially free of defects. However, for these grains the precondition for diffraction is not fulfilled, they become visible when the specimen is tilted [16].

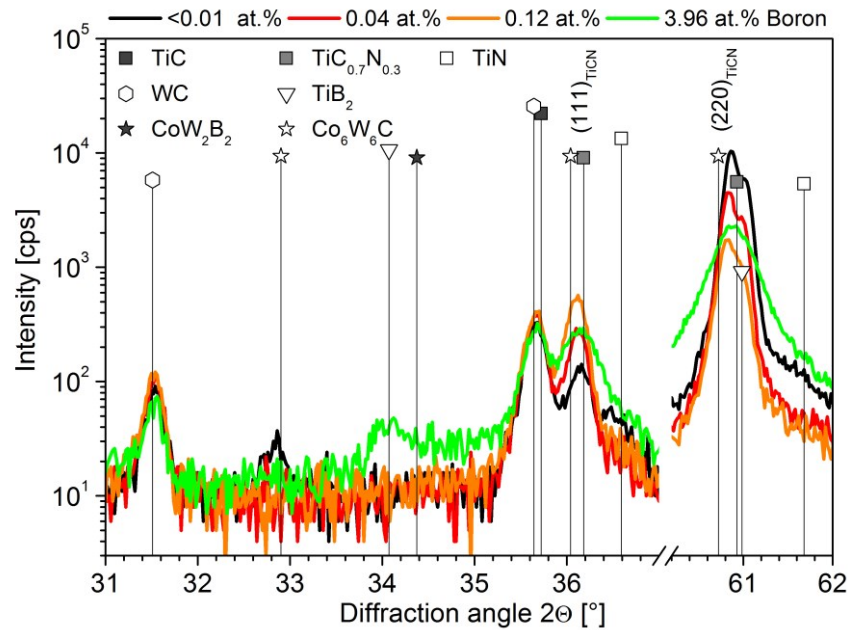


Fig. 5: XRD patterns of coatings with <math><0.01</math>, <math>0.04</math>, <math>0.12</math> and <math>3.96</math> at.% B.

The average grain width, estimated by a line intersection method, decreases with increasing B incorporation. The coating with 0.04 at.% B shows a grain width of 130 to 230 nm, while for the coating with the highest boron content 50 to 120 nm could be determined. This corresponds to the lamella width of the SEM top view image shown in Fig. 3.

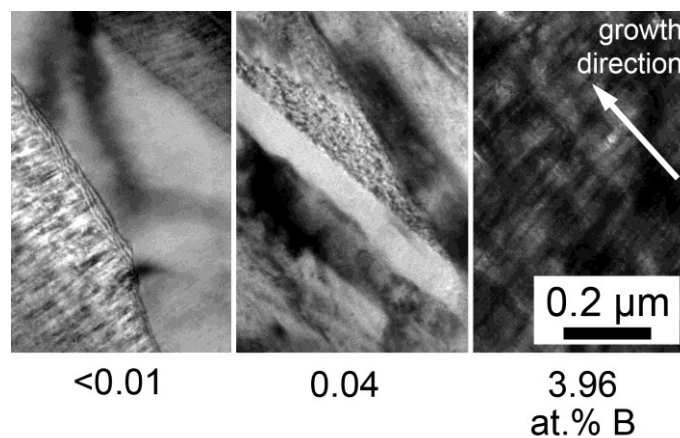


Fig. 6: TEM bright field cross-sections of the coatings with different boron contents.

### 3.4. Mechanical properties

The residual stress of the coatings was determined using the  $\sin^2\Psi$  method and its dependency on the boron content is illustrated in Fig. 7. Due to the fact that CVD  $\text{TiC}_x\text{N}_{1-x}$  based coatings usually show thermal cracks, only the remaining stresses after cracking can be measured. The influence of the B content on the thermal expansion coefficient is assumed to be minor and thus the cracking behavior of the investigated coatings should be comparable. The increasing incorporation of boron



in the coatings led to an increase of the residual tensile stress from  $542 \pm 35$  GPa for the  $\text{TiC}_x\text{N}_{1-x}$  reference system to  $638 \pm 23$ ,  $617 \pm 25$  and  $794 \pm 28$  GPa for 0.04, 0.12 and 3.96 at.% B, respectively.

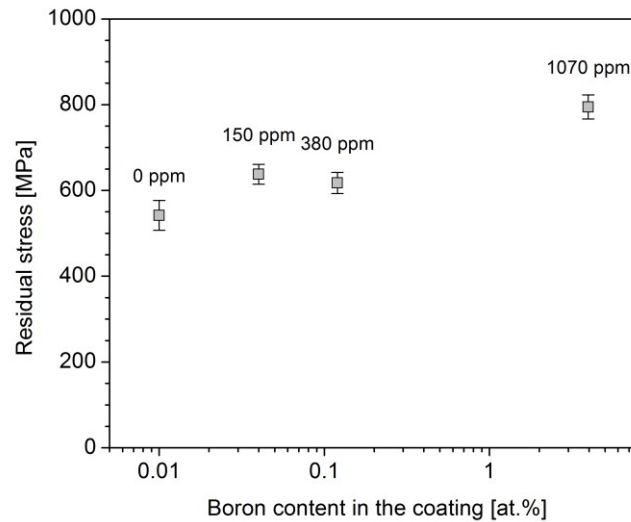


Fig. 7: Residual stress of the coatings determined with the  $\sin^2\Psi$  method depending on their boron content.

Hardness and elastic modulus were determined using nanoindentation. The hardness of the coatings (cf. Fig. 8) increases from  $26.9 \pm 1.1$  GPa to values of  $28.9 \pm 1.5$ ,  $30.1 \pm 1.2$  and  $30.5 \pm 1.3$  GPa for boron contents of 0.04, 0.12 and 3.96 at.%, respectively. The hardness of the  $\text{TiC}_x\text{N}_{1-x}$  reference coating as well as the increase due to the incorporation of boron correspond well to literature [19, 29]. The decrease of the elastic modulus from  $543 \pm 19$  GPa for  $\text{TiC}_x\text{N}_{1-x}$ , which corresponds to earlier work [16], to  $485 \pm 11$  GPa for the coating with the highest boron content shows an approximately exponential correlation to the incorporated boron, but higher values compared to literature [30]. Additional measurements on a (001) sapphire single crystalline reference sample with elastic modulus of 410 GPa yielded values of  $404.5 \pm 13$  GPa, thus calibration errors could be excluded.

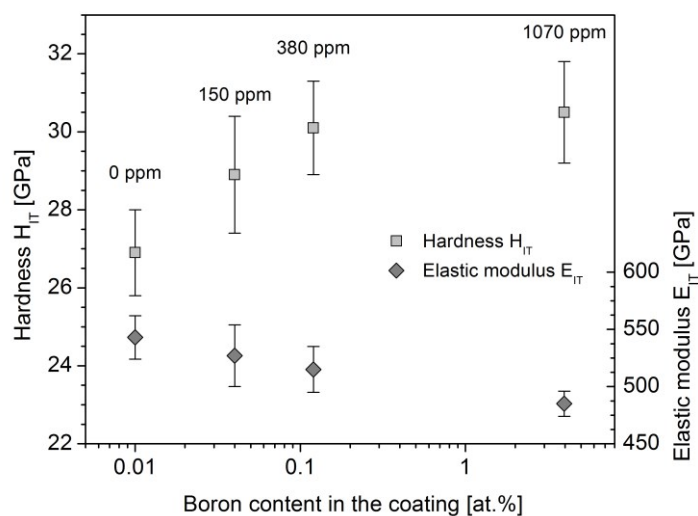


Fig. 8: Indentation hardness  $H_{1T}$  and elastic modulus  $E_{1T}$  depending on the boron content of the coatings.

### 3.5. Cutting performance

For the evaluation of the cutting performance, segment turning and milling tests were conducted on cemented carbide inserts with the synthesized coatings. Fig. 9 shows the maximum flank wear of the cutting inserts in both cutting operations depending on the boron content of the coatings. For the continuous turning operation, a clear improvement could be identified for the coating with a low boron content of 0.04 at.%. In contrast, the maximum content of 3.96 at.% led to an increasing tendency for crater wear and also to increased flank wear. For the milling operation, also significant improvement was obtained for low amounts of boron in the coating. In this cutting operation, not only the continuous wear, but also the formation of thermal cracks limits the lifetime. Due to the comparable coating thickness, the formation of these thermal cracks was similar for all investigated coatings and thus we focused on the examination of the flank wear. No chipping at the cutting edge could be observed. A significant increase in lifetime and a decrease of flank wear could be found for the coatings with 0.04 and 0.12 at.% B. Similar to the turning operation, a decrease of the cutting performance could be observed for the highest amount of boron, i.e. 3.96 at.%, but not as pronounced as for turning.

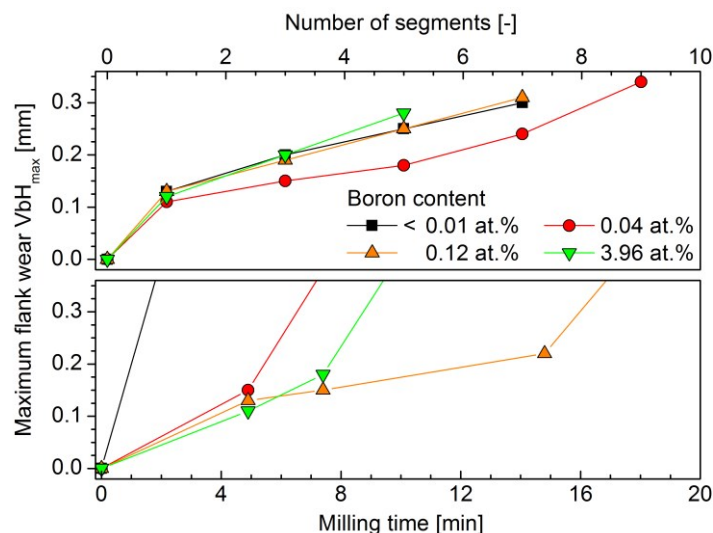


Fig. 9: Maximum flank wear of the coatings in segment turning and milling operation depending on the boron content of the coatings.

## 4. Discussion

The results obtained demonstrate the feasibility to deposit  $\text{TiC}_x\text{N}_y\text{B}_{1-(x+y)}$  hard coatings using the  $\text{TiCl}_4\text{-C}_2\text{H}_6\text{-H}_2\text{-N}_2\text{-BCl}_3$  gas system at 920 °C. The columnar structure of the  $\text{TiC}_x\text{N}_{1-x}$  reference system without B (c.f. Fig. 3) and the preferred (110) texture are comparable to MT-TiCN coatings investigated in an earlier work [16]. The obtained higher hardness is caused by the higher carbon content (c.f. Fig. 8) in the coating and in good agreement to results published by Holzschuh [19, 31] for coatings deposited at 1015 °C using  $\text{CH}_4$  as carbon feed gas. In contrast to these

observations, the deposition rate was unaffected by the  $\text{BCl}_3$  addition in this work. The chemical composition of the  $\text{TiC}_x\text{N}_y\text{B}_{1-(x+y)}$  coatings (c.f. Tab. 1) shows carbon fractions of  $0.8 < x < 0.9$ , which are significantly higher than for coatings based on the MT-TiCN process [32]. The modification of the coating structure is similar to the results reported by Holzschuh [19, 31] and Wagner et al. [11], when boron is incorporated into the TiN or  $\text{TiC}_x\text{N}_{1-x}$  solid solution, but the used  $\text{BCl}_3$  fractions differ significantly. Wagner et al. found a boron content of 3 at.% in TiNB coatings when 20 vol.%  $\text{BCl}_3$  at 950 °C and atmospheric pressure were used. Holzschuh used 0.4 vol.%  $\text{BCl}_3$  in the MT-TiCN process to incorporate approximately 3 at.% B at 900-1000 °C. The  $\text{BCl}_3$  fraction used in this work is lower by a factor of 4 compared to Holzschuh and 200 compared to Wagner et al. to achieve comparable B contents in the coatings. This is caused by the lower process pressure, which corresponds to a decreased residence time of the feed gases in the reactor. The formation of the  $\text{TiB}_2$  phase at higher boron contents is comparable to the findings of Wagner et al.; however, in the present work no peak shift of the  $\text{TiC}_x\text{N}_{1-x}$  phase due to B incorporation was observed (c.f. Fig. 5). Nevertheless, the increase of hardness is significant even when small amounts of boron are incorporated. These results agree well to literature [11, 19, 31], even for the different measurement methods and instruments. TEM results (c.f. Fig 6) showed that the incorporation of boron led to homogeneously distributed defects. No evidence for B segregation to the grain boundaries could be observed [19, 20]. The increasing number of defects is coupled with an increase of residual stress in the coating (c.f. Fig. 7), but no significant grain fining effect could be observed, till the structure transfers to the lamellar type characteristic for the highest boron content studied. The GDOES profile for the highest  $\text{BCl}_3$  fraction of 1070 ppm (c.f. Fig 2) showed a decrease of boron from the uppermost to lower regions of the coating. One possible explanation is that the highly distorted lamellar structure could not incorporate the total amount of  $\text{BCl}_3$  offered, and thus its concentration in the boundary layer formed in the CVD process [26] increases during layer growth. Only for this high  $\text{BCl}_3$  fraction, small traces of a Co-W-B phase could be observed. This high  $\text{BCl}_3$  fraction is thus too high both from the deposition point of view (i.e. formation of Co-W-B- phase) and it moreover affects the coating structure in an undesired way (i.e. formation of a lamellar structure). According to the findings of Holzschuh [19], an increasing performance of  $\text{TiC}_x\text{N}_y\text{B}_{1-(x+y)}$  coatings with low amounts of boron was obtained in milling operation. But in contrast to [19], also an increase of lifetime was observed in turning tests, when low amounts of 0.04 at.% B are incorporated.

Tab. 1: Chemical composition of the coatings.

at. %	BCl <sub>3</sub> fraction in the feed gas			
	0 ppm	150 ppm	380 ppm	1070 ppm
<b>B</b>	0.01	0.04	0.12	3.96
<b>Ti</b>	50.2	49.9	50.1	49.7
<b>C</b>	39.7	45.5	41.4	40.2
<b>N</b>	10.0	4.5	8.3	6.0

## 5. Summary and conclusions

TiC<sub>x</sub>N<sub>y</sub>B<sub>1-(x+y)</sub> coatings were deposited via CVD using a TiCl<sub>4</sub>-C<sub>2</sub>H<sub>6</sub>-H<sub>2</sub>-N<sub>2</sub>-BCl<sub>3</sub> gas system at 920 °C with BCl<sub>3</sub> fractions from 0 to 1070 ppm, yielding a maximum boron content in the coating of 3.96 at.%. Since boron incorporation into the coatings correlates exponentially to the BCl<sub>3</sub> fraction in the feed gas, careful dosing of the precursor is necessary. The increasing boron content resulted in an increasing number of defects in the formed TiC<sub>x</sub>N<sub>y</sub>B<sub>1-(x+y)</sub> solid solution, in an increasing hardness and residual tensile stress, till the structure converts from an equiaxed, columnar to a lamellar structure for the highest boron content. An improved cutting performance could be detected in milling and turning tests for boron contents below 3 at.%. Compared to earlier studies, the used feed gas system offers the possibility to deposit TiC<sub>x</sub>N<sub>y</sub>B<sub>1-(x+y)</sub> coatings at low temperatures with high carbon ratios and hardness enhancement due to the low amounts of boron incorporated, where substrate contamination by boron in-diffusion can be neglected.

## Acknowledgements

Financial support by the Österreichische Forschungsförderungsgesellschaft mbH, the Province of Styria, the Steirische Wirtschaftsförderungsgesellschaft mbH and the Municipality of Leoben within research activities of the Materials Center Leoben under the frame of the Austrian Kplus Competence Center Programme is gratefully acknowledged.

## References

- [1] W. Schedler, Hartmetall für den Praktiker, Plansee TIZIT, Düsseldorf, 1988.
- [2] EMUGE-Franken, Handbuch der Gewindetechnik und Frästechnik, EMUGE-Franken, Erlangen, 2004.
- [3] S. Ruppi, J. Phys. IV 11/Pr3 (2001) 847.
- [4] S. Ruppi, Surf. Coat. Technol. 202/17 (2008) 4257.
- [5] M. Bonetti-Lang, R. Bonetti, H.E. Hintermann, D. Lohmann, Int. J. of Refract. Hard Mater. 1/4 (1982) 161.
- [6] E. Kübel, Surf. Coat. Technol. 49/1-3 (1991) 268.
- [7] A. Osada, M. Danzinger, R. Haubner, B. Lux, J. Phys. IV 1/C2 (1991) 557.
- [8] S. Kudapa, K. Narasimhan, P. Boppana, W.C. Russell, Surf. Coat. Technol. 121 (1999) 259.
- [9] H. Holzschuh, Thin Solid Films 469-70 (2004) 92.
- [10] M.H. Staia, D.G. Bhat, E.S. Puchi-Cabrera, J. Bost, Wear 261/5-6 (2006) 540.
- [11] J. Wagner, D. Hochauer, C. Mitterer, M. Penoy, C. Michotte, W. Wallgram, M. Kathrein, Surf. Coat. Technol. 201/7 (2006) 4247.
- [12] H. Holzschuh, J. Phys. IV 10/P2 (2000) 49.
- [13] I. Dreiling, C. Raisch, J. Glaser, D. Stiens, T. Chassé, Surf. Coat. Technol. 206/2-3 (2011) 479.
- [14] I. Dreiling, D. Stiens, T. Chassé, Surf. Coat. Technol. 205/5 (2010) 1339.
- [15] S. Ruppi, A. Larsson, J. Vac. Sci. Technol. A 21/1 (2003) 66.
- [16] C. Czettl, C. Mitterer, U. Mühle, D. Rafaja, S. Puchner, H. Hutter, M. Penoy, C. Michotte, M. Kathrein, Surf. Coat. Technol. 206/7 (2011) 1691.
- [17] K. Hiroyuki, Patent No. EP1138800A1, 2001.
- [18] R. Bonetti, H.E. Hintermann, J. Electroch. Soc. 124/8 (1977) C298.
- [19] H. Holzschuh, in: G. Kneringer, P. Rödhammer, H. Wildner (Eds.), Plansee Seminar, Plansee, Reutte, 2001, p. 441.
- [20] H. Holzschuh, in: G. Kneringer, P. Rödhammer, H. Wildner (Eds.), Plansee Seminar, Plansee, Reutte, 2005, p. HM59.
- [21] W. Wallgram, U. Schleinkofer, in: L.S. Sigl, P. Rödhammer, H. Wildner (Eds.), Plansee Seminar 2009, Plansee, Reutte, Austria, 2009, p. HM32.
- [22] B. Rother, H. Kappl, Surf. Coat. Technol. 96/2-3 (1997) 163.
- [23] J.L. Peytavy, A. Lebugle, G. Montel, H. Pastor, High Temperatures-High Pressures 10 (1978) 341.
- [24] J.L. Peytavy, A. Lebugle, G. Montel, H. Pastor, Wear 52 (1979) 89.
- [25] C. Czettl, C. Mitterer, C. Michotte, M. Penoy, M. Kathrein, in: L.S. Sigl, P. Rödhammer, H. Wildner (Eds.), Plansee Seminar 2009, Plansee, Reutte, Austria, 2009, p. HM71.1
- [26] H.O. Pierson, Handbook of Chemical Vapor Deposition, Noyes Publications, New Jersey, 1999.
- [27] U. Mühle, S. Jansen, S. Leinert, D. Breuer, Pract. Met. 43 (2006) 306.
- [28] W.C. Oliver, G.M. Pharr, J. Mat. Res. 7/6 (1992) 1564.
- [29] W. Lengauer, S. Binder, K. Aigner, P. Ettmayer, A. Guillou, A. Debuigne, G. Groboth, J. Alloy Compd. 217 (1995) 137.
- [30] C. Kral, W. Lengauer, D. Rafaja, P. Ettmayer, J. Alloy Compd. 265/1-2 (1998) 215.
- [31] H. Holzschuh, Int. J. Refract. Met. Hard Mater. 20/2 (2002) 143.
- [32] A. Larsson, S. Ruppi, Thin Solid Films 402/1-2 (2002) 203.